

Technical Report

**ATMOSPHERIC CORRECTION AND SIMULATION
OF SPACE-ACQUIRED REMOTE SENSOR DATA:
0.4- TO 1.0- μ m SPECTRAL RANGE**

by

R. Horvath, M. Spencer, and R. Turner

INFRARED AND OPTICS DIVISION
WILLOW RUN LABORATORIES
INSTITUTE OF SCIENCE AND TECHNOLOGY
THE UNIVERSITY OF MICHIGAN

prepared for

NATIONAL AERONAUTICS AND SPACE ADMINISTRATION

NAS 9-12269

Manned Spacecraft Center
Houston, Texas

(NASA-CR-152922) ATMOSPHERIC CORRECTION AND
SIMULATION OF SPACE-ACQUIRED REMOTE SENSOR
DATA: 0.4 TO 1.0- MICRON SPECTRAL RANGE
(Michigan Univ.) 139 p

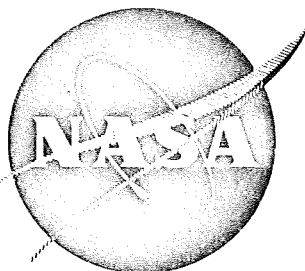
N77-77964

Unclas

00/46 02208

7/24/76
R

NASA CR-
WRL 10657-5-F



ATMOSPHERIC CORRECTION AND SIMULATION
OF SPACE-ACQUIRED REMOTE SENSOR DATA:
0.4- TO 1.0- μ m SPECTRAL RANGE

by

R. HORVATH, M. SPENCER, AND R. TURNER

INFRARED AND OPTICS DIVISION
WILLOW RUN LABORATORIES
INSTITUTE OF SCIENCE AND TECHNOLOGY
THE UNIVERSITY OF MICHIGAN

prepared for

NATIONAL AERONAUTICS AND SPACE ADMINISTRATION

NASA Manned Spacecraft Center
NAS 9-12269

02208

NOTICES

Sponsorship. The work reported herein was conducted by the Willow Run Laboratories of the Institute of Science and Technology for the National Aeronautics and Space Administration for the Manned Spacecraft Center under Contract No. NAS 9-12269. Technical Monitor is D. Evans. Contracts and grants to The University of Michigan for the support of sponsored research are administered through the Office of the Vice-President for Research.

Disclaimers. This report was prepared as an account of Government-sponsored work. Neither the United States, nor the National Aeronautics and Space Administration (NASA), nor any person acting on behalf of NASA:

- (A) Makes any warranty or representation, expressed or implied with respect to the accuracy, completeness, or usefulness of the information contained in this report, or that the use of any information, apparatus, method, or process disclosed in this report may not infringe privately owned rights; or
- (B) Assumes any liabilities with respect to the use of, or for damages resulting from the use of any information, apparatus, method, or process disclosed in this report.

As used above, "person acting on behalf of NASA" includes any employee or contractor of NASA, or employee of such contractor, to the extent that such employee or contractor of NASA or employee of such contractor prepares, disseminates, or provides access to any information pursuant to his employment or contract with NASA, or his employment with such contractor.

Availability Notice. Requests for copies of this report should be referred to:

National Aeronautics and Space Administration
Scientific and Technical Information Facility
P. O. Box 3767

BALTIMORE/WASHINGTON INTERNATIONAL AIRPORT,
MARYLAND, 21240

Final Disposition. After this document has served its purpose, it may be destroyed. Please do not return it to the Willow Run Laboratories.

ACKNOWLEDGMENTS

This report and the program of investigation which it describes represent the work of several people. Mr. Robert Horvath, under Dr. Jon D. Erickson, had overall responsibility for technical direction of the effort. Miss Margaret M. Spencer performed the model validation analyses using the multispectral scanner data, and contributed Section 4. Dr. Robert E. Turner directed the radiative transfer model calculations, assisted in developing the simplified calculational procedures of Section 3, and contributed the Appendices. Mr. Jackson P. Livisay performed the computer processing of the multispectral scanner data and programmed the sensor simulation algorithms. Mr. Richard F. Nalepka provided valuable advice and counsel concerning the multispectral recognition analyses and was especially helpful in the mixtures' recognition analysis. The authors express their appreciation for the assistance received from those named above and from others in the Infrared and Optics Division of the Willow Run Laboratories.

FOREWORD

This report describes part of a comprehensive, continuing program of research into remote sensing of the environment from aircraft and satellites. The research is being carried out by the Willow Run Laboratories, a unit of The University of Michigan's Institute of Science and Technology, for the NASA Manned Spacecraft Center, Houston, Texas. The basic objective of this multidisciplinary program is to develop remote sensing as a practical tool to provide the planner and decision-maker with extensive information quickly and economically.

The scope of our program includes: extending understanding of basic processes; evolving new applications for remote sensing systems; generating advanced remote sensing systems; developing automatic data processing to extract information in a useful form; and assisting in data collection, processing, and analysis, including material spectra and ground-truth verification.

The research described herein was performed under NASA Contract NAS 9-12269, and covers the period from July 1971 through July 1972. The program was directed by R. R. Legault, Associate Director of the Infrared and Optics Division. The work was done under the management of the NASA Project Manager, D. Evans, Manned Spacecraft Center. The Willow Run Laboratories' number for this report is 10657-5-F.

Page intentionally left blank

WILLOW RUN LABORATORIES

ABSTRACT

This report describes a program of investigation into certain fundamental problems associated with remote sensing from space. Particular emphasis is placed upon two problems which are often underestimated in importance: (1) the spectral, spatial, and temporal variability of the radiometric effects of the atmosphere; and (2) the impact of limited spatial resolution, and consequent presence of mixtures of target classes within individual resolution elements, upon computer implemented multispectral recognition operations. Solutions to these problems are presented in the form of: (1) a simplified calculational procedure for quantitatively determining the several radiometric effects of Earth's atmosphere as a function of wavelength, environmental conditions, and scene content; and (2) a multispectral recognition approach which specifically accounts for the possibility and recognizes the presence of mixtures of targets within individual resolution elements.

In support of the above topics, specific analyses are also described which utilize the remote sensor data collected from aircraft and spacecraft as part of the SO-65 experiment associated with the flight of Apollo IX. Multispectral scanner data are utilized in validating the accuracy of a previously developed atmospheric radiative transfer model. These same data, in concert with the model itself, are then used to calibrate radiometrically the space photography associated with the experiment. Finally, multispectral data from future space sensors are simulated and an attempt made to evaluate and compare their potential in multispectral recognition operations.

Page intentionally left blank

WILLOW RUN LABORATORIES

CONTENTS

Acknowledgments	ii
Foreword	iii
Abstract	v
List of Figures	ix
List of Tables	x
List of Symbols	xii
Summary	1
1. Introduction	3
1.1. The Atmospheric Problem	3
1.2. The Recognition-Resolution Problem	9
1.3. Scope of This Report	12
2. Discussion of Results	14
2.1. The Answer to the Atmospheric Problem	14
2.1.1. Model Input Requirements	14
2.1.2. Model Accuracy	17
2.2. One Answer to the Recognition-Resolution Problem	18
3. Simplified Atmospheric Correction Techniques	20
3.1. Input Requirements and Definitions	20
3.2. Total Atmospheric Transmittance, T_v	21
3.2.1. $T_0(\lambda, P, V, \theta_v)$	21
3.2.2. $T_{\text{ozone}}(\lambda, \theta_v)$	22
3.3. Total Path Radiance, L_p	22
3.3.1. $F(\lambda_i, T_0, \tau_0, \tau_{R0}, \tau_R, \theta_0, \phi_0, \theta_v, \phi_v)$	22
3.3.2. $G(\lambda_i, T_0, \tau_0, \tau_{R0}, \tau_R, \theta_0, \phi_0, \theta_v, \phi_v)$	23
3.3.3. $H(\lambda_i, \tau_{00}, \tau_R, \bar{\rho})$	23
3.3.4. $T_{\text{ozone}}(\lambda, \theta_0, \theta_v)$	24
3.3.5. $E_0(\lambda)$	24
3.4. Total Irradiance, E_g	24
3.4.1. $I(\lambda, \tau_{00}, \tau_R, \theta_0)$	24
3.4.2. $J(\lambda, \tau_{00}, \tau_R)$	25
3.4.3. $T_{\text{ozone}}(\lambda, \theta_0)$	25
4. Radiative Transfer Model Validation	48
4.1. Data Base for Validation Analysis	48
4.1.1. Multispectral Scanner Data Acquisition	48
4.1.2. Computer Processing of Multispectral Data	50
4.1.3. Parameters for Validation Modeling	52
4.1.4. Target Selection	53

WILLOW RUN LABORATORIES

4.2. Validation Analysis	54
4.2.1. Validation by ρ^t Comparison	55
4.2.2. Validation by Means of ρ^t Equivalence	58
4.2.3. Validation Summary	74
5. SO-65 Photography Calibration	75
5.1. Model Validation Attempts with SO-65 Data	75
5.2. SO-65 Data Calibration	78
5.2.1. Extrapolation of Scanner Data	78
5.2.2. Simulation of SO-65 Photographic Data	80
5.2.3. SO-65 Calibration	84
6. Analysis of Simulated ERTS and SKYLAB Data	93
6.1. Simulation	93
6.2. Standard Multispectral Recognition Evaluation	95
6.3. Analysis of Mixtures Within a Resolution Element	99
Appendix I: Earth's Atmosphere	103
Appendix II: The Radiative Transfer Model	112
Appendix III: Simulated S-192 Multispectral Scanner Imagery	117
References	127
Distribution List	129

FIGURES

1. Spectral Radiance of a Corn Field as Seen from Space for Several Atmospheric Conditions	6
2. Spectral Radiance of Sandy Loam Soil as Seen from Space for Several Atmospheric Conditions.	7
3. Spectral Radiance of a Corn Field as Seen from Space for Two Background Conditions	8
4. <u>A Priori</u> Probability that any Particular Resolution Element Will Contain a Mixture When Imaging Extended Checkerboard Field Pattern.	11
5. Geometry Defining Solar and View Angles	26
6. Dependence of Total Rayleigh Optical Depth τ_{R0} on Wavelength for United States Standard Atmosphere	27
7. Aerosol Optical Depth τ_A Versus Visual Range V	28
8. Transmittance T Versus Optical Depth τ	29
9. Average Ozone Optical Depth τ_{ozone} Versus Wavelength λ	30
10. Radiance Function F_0 Versus Derived Angle θ_s	31-35
11. Radiance Function G_0 Versus Solar Zenith Angle θ_0	36-38
12. Radiance Function H_0 Versus Transmittance T_{00}	39-41
13. Extraterrestrial Solar Spectral Irradiance E_0	42
14. Irradiance Function I_0 Versus Solar Zenith Angle θ_0	43-46
15. Irradiance Function J_0 Versus Transmittance T_{00}	47
16. Effective Diffuse Spectral Reflection for a Barley Field.	56
17. Effective Diffuse Spectral Reflection for a Salt Flat	56
18. Hypothetical Slope-Intercept (S-I) Line for L(10) Versus L(5).	59
19. Slope-Intercept Comparison at 0.422 μm (Spectrometer Channel 1)	63
20. Slope-Intercept Comparison at 0.457 μm (Spectrometer Channel 3)	64
21. Slope-Intercept Comparison at 0.491 μm (Spectrometer Channel 5)	65
22. Slope-Intercept Comparison at 0.511 μm (Spectrometer Channel 6)	66
23. Slope-Intercept Comparison at 0.533 μm (Spectrometer Channel 7)	67
24. Slope-Intercept Comparison at 0.563 μm (Spectrometer Channel 8)	68
25. Slope-Intercept Comparison at 0.602 μm (Spectrometer Channel 9)	69
26. Slope-Intercept Comparison at 0.646 μm (Spectrometer Channel 10)	70
27. Slope-Intercept Comparison at 0.708 μm (Spectrometer Channel 11)	71
28. Slope-Intercept Comparison at 0.800 μm (Spectrometer Channel 12)	72
29. Relative Spectral Sensivity	83

WILLOW RUN LABORATORIES

30. Calibration Curve for AS9-26-3799B: SO-65 Camera BB Positive Transparency	86
31. Calibration Curve for AS9-26-3799C: SO-65 Camera CC Positive Transparency	87
32. Calibration Curve for AS9-26-3799D: SO-65 Camera DD Positive Transparency	88
33. Calibrated Reproduction of SO-65 Frame AS9-26-3799B	90
34. Calibrated Reproduction of SO-65 Frame AS9-26-3799C	91
35. Calibrated Reproduction of SO-65 Frame AS9-26-3799D	92
36. Standard Recognition Results for the Space-Simulated Sensor Data and for the Original 10-Channel Scanner Data	98
37. Wavelength Dependence of the Attenuation Coefficient for Rayleigh Molecular Scattering and Mie Aerosol Scattering in Earth's Atmosphere	106
38. Variation of Visual Range with Extinction Coefficient	111
39. Simulated S-192 Multispectral Scanner Imagery	118
40. Imperial Valley Test Area	119-120

WILLOW RUN LABORATORIES

TABLES

1. Proportions of Various Target Classes in 18,600 Acres of Imperial Valley	19
2. Spectral Response Limits of the 12-Channel Spectrometer.	49
3. Mean Value of the Calculated Differences ρ_{10}^t to ρ_5^t for Each Spectral Channel	57
4. Relative Effect Upon S-I (Slope-Intercept) Line Calculation Caused by Input Uncertainties	60
5. Nominal Value and Uncertainty for Average Background Terrain Albedo, $\bar{\rho}$	61
6. Specific Values of the Model Input Parameters Used for Calculating Limiting S-I (Slope-Intercept) Line	62
7. Estimated Minimum RMS Calibration Errors for SO-65 Cameras with Type 3400 Film	77
8. Simulation Accuracy for SO-65 Cameras	82
9. Simulation Accuracy for ERTS and SKYLAB Sensors	94
10. Average Pair-Wise Probability of False Alarm for Original (10 Channel) Scanner Data	97
11. Average Pair-Wise Probability of False Alarm for S-192 (7 Channels Only) Data	97
12. Average Pair-Wise Probability of False Alarm for MSS (4 Channel) Data	97
13. Average Pair-Wise Probability of False Alarm for RBV (3 Channel) Data	97
14. Size Distribution of Aerosol Particles	104
15. Imperial Valley Ground Truth	121-125
16. Field Key for Table 15	126

WILLOW RUN LABORATORIES

SYMBOLS

a	gamma distribution factor
A_0	Avogadro's number
b	gamma distribution factor
E	irradiance
E_g	irradiance at ground
E_0	extraterrestrial solar spectral irradiance
F	path radiance function corrected for nonstandard conditions
F_0	path radiance function for standard conditions
g	acceleration as a result of gravity
g_0	acceleration as a result of gravity at sea level
G	path radiance function corrected for nonstandard conditions
G_0	path radiance function for standard conditions
h	height above Earth's surface
h	altitude above sea level in appendices
h_0	station altitude above sea level
H	albedo function corrected for nonstandard conditions
H_p	scale height for aerosol distribution
H_0	albedo function for standard conditions
i	index
I	ground irradiance function corrected for nonstandard conditions
I, I_0	intensity in Appendix I
I_0	ground irradiance function for standard conditions
j	index
J	ground irradiance function corrected for nonstandard conditions
J_0	ground irradiance function for standard conditions
K_G, K_F	G and F function correction factors for nonstandard conditions
L	spectral radiance
L^B	band radiance
\overline{L}^B	mean band radiance
L_t	intrinsic target radiance
L_j	different spectral radiance distributions
$L_p(h)$	path radiance generated between the target and the sensor at altitude h
L_p	total radiance of the line-of-sight path between the surface and space
L_T	total spectral radiance
L_T^t	total target spectral radiance

m	index of refraction
M	mean molecular mass of the atmosphere
n	number of spectral bands
n_p	aerosol-density distribution function in appendices
N	number of data points within a target area
N	particle number density in Appendix I
N_p	particle size and density distribution
N_s	sea level number density
p	single scattering phase function
p_i	proportion of target class i
P	atmospheric pressure
r	particle radius
r_i	relative response of the i -th spectral band
r_0	relative response of a reference spectral band
t	target
$T(h)$	transmittance from target to sensor at altitude h
T_{ozone}	transmittance for atmospheric ozone
T_u	turbidity
T_v	transmittance from Earth's surface to space
T_{00}	transmittance vertically of total atmosphere without ozone
T_0	transmittance of total atmosphere without ozone for particular nadir view angle
V	visual range
w_i	weighting factor
x	distance
z	vertical distance
α	volume absorption coefficient
β	volume scattering coefficient
γ	slope of film density versus log exposure curve
γ	gamma distribution factor in appendices
δ	delta function
Δ	depolarization anisotropy factor
ξ	gamma distribution factor
η	fraction of energy scattered in the forward hemisphere
θ	scattering angle
θ_s	angle between the vector defining the direction of view and the vector defining the direction of travel of unscattered solar radiation

WILLOW RUN LABORATORIES

θ_v	nadir view angle
θ_0	solar zenith angle
κ	volume extinction coefficient
κ_R	volume extinction coefficient for Rayleigh scattering
κ_0	volume extinction coefficient at sea level
λ, λ_i	spectral wavelength
μ	cosine θ
μ'	cosine θ'
μ_0	cosine θ_0
ρ	reflectance
ρ	density of the atmosphere in appendices
$\bar{\rho}$	mean surface (Lambertian) reflectance
ρ^t	effective diffuse target reflectance
σ_a	absorption cross section
σ_s	scattering cross section
σ_t	total cross section
$\bar{\sigma}_t$	mean total cross section
τ	optical depth
τ_A	aerosol optical depth
τ_{ozone}	optical depth for atmospheric ozone
τ_R	Rayleigh optical depth of atmosphere for specific conditions
τ_{R0}	Rayleigh optical depth of atmosphere for standard conditions
τ_0	total optical depth of the atmosphere relative to sea level
$\tau_{0,h}$	optical depth between surface and altitude h
τ_{00}	vertical optical depth of total atmosphere without ozone
ϕ	relative angle between the solar plane and the view angle
ϕ_r	relative azimuth
ϕ_v	azimuth view angle
ϕ_0	solar azimuth angle
ψ	aerosol size distribution function
ω_0	single scattering albedo

ATMOSPHERIC CORRECTION AND SIMULATION OF SPACE-ACQUIRED
REMOTE SENSOR DATA: 0.4- TO 1.0- μ m SPECTRAL RANGE

SUMMARY

The program for which this document serves as the final technical report represented a rather diverse technical analysis aimed at utilizing the remote sensor data of the SO-65 experiment associated with the flight of Apollo IX to address questions and problems not previously examined. The technical scope of the program involved: (1) validation of a previously developed atmospheric radiative transfer model utilizing SO-65 experimental data; (2) reduction of the model's necessary complexity to the end of producing simplified atmospheric correction algorithms which would be of practical utility to the average user of space-acquired remote sensor data; (3) radiometric calibration of space photography generated during the SO-65 experiment; (4) simulation of the space data expected to be acquired from ERTS and SKYLAB-EREP sensors; and (5) analysis of the multispectral recognition potential, especially as regards the recognition-resolution problem, of future space-acquired multispectral data.

All of the above technical objectives were addressed during the program, and the technical approach, methodology and results for each are reported fully. However, the above five tasks really reduce to addressing two problems of fundamental importance to the future utility of remotely sensed data: (1) the impact of the spectral, spatial and temporal variability of the radiometric effects of the atmosphere; and (2) the impact of limited spatial resolution and consequent presence of mixtures of target classes within individual resolution elements.

A description of these two fundamental problems and of their importance is given in Section 1 of this report. It is shown that the presence and variability of atmospheric radiometric effects not only alters the spectral signatures of objects observed from space, but, more importantly, produces an alteration which varies qualitatively as well as quantitatively with atmospheric state and leads to different total signature effects for different target types. In addition, it is shown that the scene context within which a particular target is located also has a significant effect upon the character of the target's spectral signature as viewed from space. It is also shown in Section 1 that, limited spatial resolution for space sensors means that a very significant proportion of resolution elements seen from space will contain mixtures of target classes, resulting in a measured spectrum or signature for those elements which is a mixture of the pure signatures of the classes involved. Standard multispectral recognition approaches do not account for such a condition.

The overall results of the program of investigation are synthesized in Section 2 to describe solutions to the fundamental problems of atmospheric effects and recognition-resolution. The solution for the atmospheric problem rests upon a simplified calculational procedure for quantitatively determining the several radiometric effects of Earth's atmosphere as a function of wavelength, environmental conditions and scene content. The solution to the recognition-resolution problem is a multispectral recognition approach which specifically accounts for the possibility, and recognizes the presence of mixtures of targets within individual resolution elements.

Section 3 presents a cookbook recipe for calculating the several radiometric effects of the atmosphere upon space-acquired remote sensor data. The procedure is the result of simplifications applied to a more general atmospheric radiative transfer model previously developed. The necessary inputs are described in detail, and possible sources indicated. A step-by-step procedure is then defined which allows determination of all the atmospheric effects relevant to remote sensing from space in the 0.4- to 1.0- μm spectral range. The simplification is achieved by defining a standard space condition as a norm, and then tailoring it to specific conditions by successive corrections for surface pressure, ozone and non-nadir viewing geometry.

Section 4 describes the radiative transfer model validation analysis representing the most sophisticated attempt to date for validation of the calculated atmospheric effects in down-looking remote sensor systems. It is shown that, within the error limitations of the experimental data, the model appears to correctly calculate those quantities necessary to describe the atmospheric effects. In particular, it is shown that for wavelengths in the blue and green regions of the visible spectral range, the accuracy with which the atmospheric effects can be calculated is predominantly controlled by the accuracy with which the ground truth input parameters describing the atmospheric state can be determined.

Section 5 describes the calibration efforts on the SO-65 space photography. Only limited goals were achieved in comparison to initial hopes. Problems associated with photographic processing of the space photography reproductions precluded using these data for even the most general validation of the radiative transfer model's ability to calculate the effects of the entire atmosphere. However, absolute radiometric calibration was achieved by indirect methods for a portion of the scene present in SO-65 data set AS9-26-3799. From this calibration the effective reflectance of scene elements could be determined.

Section 6 describes space sensor simulations which were produced by a new but quite simple simulation technique. The simulations are valid in describing mean target spectral radiance values and may also be valid in defining the target-associated variance. However, comparison of multispectral recognition results produced from these simulations leads to some questions regarding their ability to measure accurately the relative recognition capabilities of various space sensors.

Section 6 also provides a comparison of multispectral recognition techniques with quite significant results being observed. A mixtures recognition approach is applied to multispectral data of degraded spatial resolution. The mixtures recognition allows a determination of proportions or mixtures of several targets within a single resolution element. This technique is shown to provide excellent recognition when compared to ground truth data, and much superior results to those obtained by means of a standard multispectral recognition technique.

1

INTRODUCTION

The SO-65 experiment associated with the flight of Apollo IX represented a major advance in remote sensing of Earth for peaceful purposes. The data consisted of (1) SO-65 multispectral photography taken from the spacecraft; (2) the film produced during the simultaneous high-altitude underflights of NASA's camera-equipped RB-57 aircraft; and (3) the radiometrically-calibrated multispectral line scans made in near-simultaneous underflights over Imperial Valley by Willow Run Laboratories' C-47 aircraft. Because of the variety of sensors and platforms involved, the SO-65 experiment produced a significant data base containing a wide range of information acquired at various spectral and spatial resolutions, containing a wide range of synoptic scene contents, and being affected by a wide range of atmospheric path conditions.

The data produced by the SO-65 experiment have been subjected to extensive analysis and interpretation. Representative of the results are a recent NASA publication [1] summarizing the results of vegetation-oriented Earth resource investigations, as well as previous publications (e.g., Ref. 2) describing geologic analyses. These analysis programs were primarily directed toward qualitative analysis in the sense of classical photointerpretation. Even when rather sophisticated techniques of, for example, false-color image reconstruction were utilized, the methodology was fundamentally qualitative in nature. In particular, two very fundamental and significant questions were neither approached nor accounted for: (1) what is the effect of the atmosphere upon the multispectral data acquired from space or from the aircraft; and (2) how can one maximize the information content of remote sensor data for which the spatial resolution is of significant magnitude compared to the scale of the phenomenon under investigation? It is the purpose of this report to address these two fundamental questions utilizing the data base resulting from the SO-65 experiment.

1.1. THE ATMOSPHERIC PROBLEM

The atmosphere has long represented a fundamental problem in remote sensing to astronomers and planetary and solar physicists. The use of observations of incoming electromagnetic radiation from extraterrestrial objects as an analytical tool has required development of extensive theoretical and empirical techniques in order to account for, or at least minimize, atmo-

spheric effects upon such observations. In more recent years, much technological effort and expenditure have been allocated to carry remote sensors into space so that extraterrestrial observations could be accomplished without any interference from the atmosphere. If the atmospheric effects are significant when one is looking through the atmosphere into space from Earth's surface, surely the effects cannot be ignored when one is looking at Earth's surface through that same atmosphere from space.

The atmosphere produces three fundamental effects upon remotely sensed phenomena within that region of the electromagnetic spectrum where the sun is the dominant radiation source. First, the spectral content, directionality, and intensity of the solar radiation reaching Earth's surface are modified by absorption and scattering in the atmosphere. Second, that radiation which is reflected from the surface and subsequently passes into space is also modified in spectral content, directionality, and intensity resulting from absorption and scattering. Finally, the atmosphere itself becomes an apparent radiation source interposed between Earth's surface and a space sensor because of the scattering of the incoming radiation from the sun and the outgoing radiation reflected from Earth's surface. These three effects are usually characterized, respectively, by general functions termed: (1) the irradiance at the ground, E_g ; (2) the transmittance from Earth's surface to space, T ; and (3) the radiance of the line-of-sight path between the surface and space, L_p .

For any surface target of reflectance, ρ , the radiance L of that target as seen from space is given by

$$L = \frac{\rho E_g T}{\pi} + L_p \quad (1)$$

The transmittance, T , is a function only of the atmospheric state and the target-sensor geometry. The irradiance, E_g , is a function of the atmospheric state, the target-sun geometry, the extraterrestrial solar radiation characteristics and the albedo of Earth's surface surrounding the target. Finally, the path radiance, L_p , is a function of all of the above parameters.

Figure 1 shows the calculated spectral radiance of a typical agricultural target as seen from space. For the particular geometric and background conditions indicated, the parametric effect of atmospheric state, as characterized by the horizontal visual range at the ground, is shown. A visual range of 100 km represents an exceptionally clear atmosphere, 40 km an average clear day, 20 km a clear to hazy transition, 10 km a typical haze and 5 km a very strong haze. Figure 2 shows the spectral radiance of a typical sandy loam soil under the same conditions as for Fig. 1.

Several general characteristics of the atmospheric problem are seen in Figs. 1 and 2. The most significant spectral effect occurs in the blue region of the visible spectrum, where the difference between having no atmosphere and having a very clear atmosphere (100-km visual range)

is several times larger than is the difference between having a very clear atmosphere and a very hazy one. At wavelengths longer than about $0.7 \mu\text{m}$, the opposite holds with a very clear atmosphere being nearly equivalent to no atmosphere.

The effect of changes in atmospheric state upon the spectral character of the targets of Figs. 1 and 2 is not the same. For the corn field, going from a clear atmosphere to a hazy one increases the observed radiance at wavelengths less than $0.7 \mu\text{m}$ but decreases the radiance at wavelengths greater than $0.7 \mu\text{m}$. For the sandy loam soil, the same atmospheric change from clear to hazy decreases radiance at all wavelengths greater than $0.47 \mu\text{m}$. Except for the reversal of effects on either side of $0.7 \mu\text{m}$, the corn field spectral shape is not significantly altered by changes in atmospheric state. On the other hand, the position and presence of spectral peaks and depressions in the soil spectral radiance does vary with atmospheric state. In fact, as the atmosphere becomes hazy, the observed soil radiance begins to take on vegetation-like spectral characteristics, with a definite green peak present, a depression being created beyond that peak in the yellow-red region and a near infrared peak moving out to $0.8 \mu\text{m}$ and beyond. Thus, not only does the atmosphere alter the spectral signatures of objects observed through it, but in addition, the nature of this effect varies with atmospheric state and produces different total effects for different targets.

One of the primary reasons that these spectral effects differ with a changing atmospheric state is that the spectral nature of the path radiance and of the ground irradiance is significantly dependent upon the spectral albedo of the background terrain surrounding the target. A vegetated background was assumed for the calculation of the data of Figs. 1 and 2. Thus, solar radiation reflected from this background and subsequently scattered to become either a part of the path radiance or a part of the ground irradiance carried with it a vegetation-like spectral quality. As the atmosphere is assumed to be more and more hazy, this ground-reflected scattered component becomes a more significant portion of both the path radiance and ground irradiance, and the path radiance itself becomes a more significant part of the total observed target radiance. This albedo effect did not greatly alter the spectral signature of the corn field since the intrinsic corn spectrum looks like vegetation anyway. However, the albedo effect did alter the spectral character of the soil which does not look intrinsically like vegetation. The greatest effect on the soil signature is in the red region, where vegetation and soil are in fact of most disparate spectral character. This dependence of the surrounding background upon the spectral albedo is shown more concisely in Fig. 3, wherein the spectral radiance of a corn field for two different background conditions is depicted. When the surrounding terrain is changed from vegetation (as used in Figs. 1 and 2) to soil, the observed spectral radiance of the corn field also changes. Without the reinforcing effect of a vegetative-like spectrum in the path radiance, the green peak disappears, the chlorophyll absorption at $0.65 \mu\text{m}$ becomes less distinct, and the near infrared peak is slightly reduced.

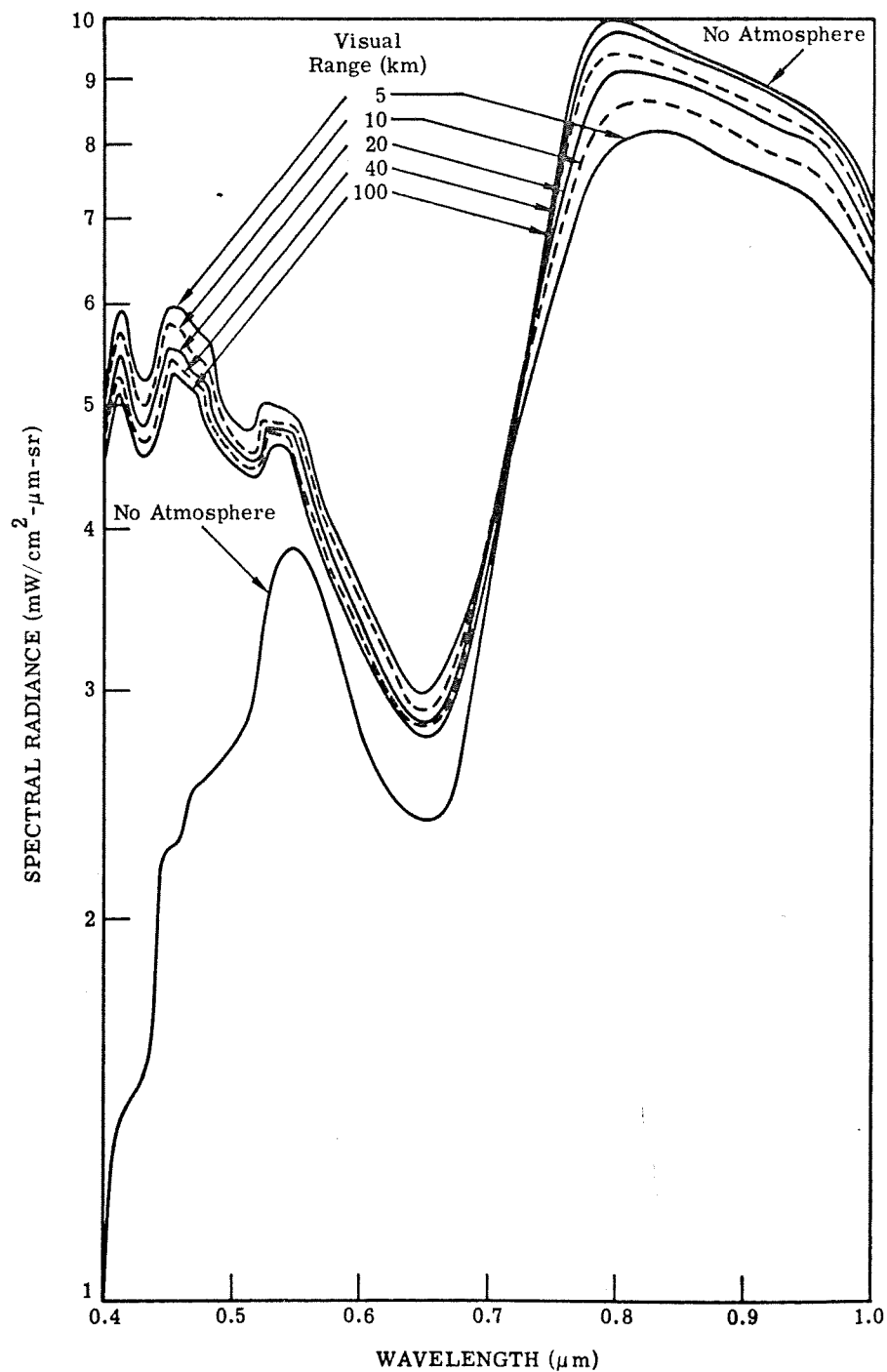


FIGURE 1. SPECTRAL RADIANCE OF A CORN FIELD AS SEEN FROM SPACE FOR SEVERAL ATMOSPHERIC CONDITIONS. Parameter is horizontal visual range at the ground. Solar zenith angle = 45° , nadir view angle = 0° , vegetation background condition assumed.

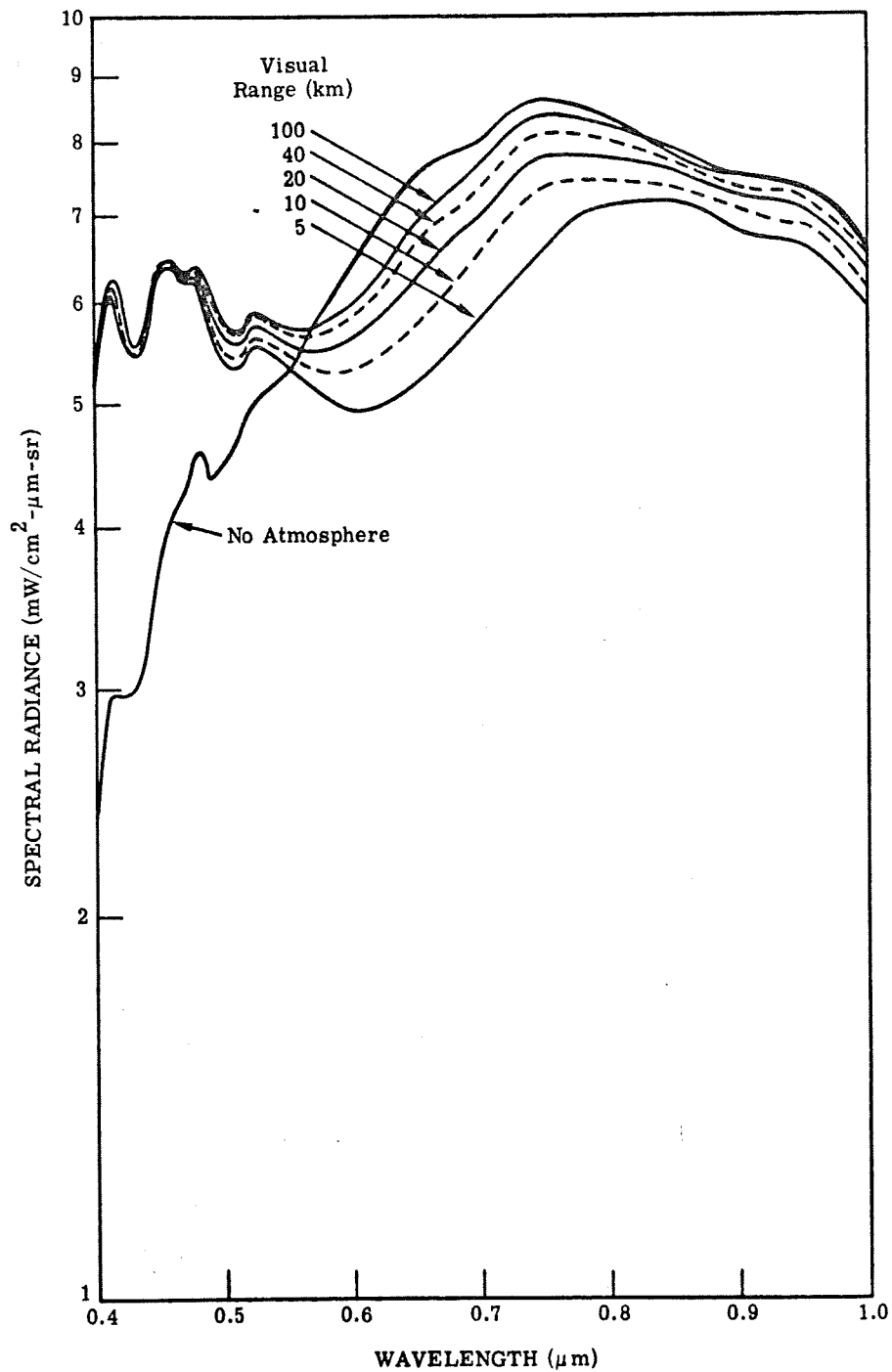


FIGURE 2. SPECTRAL RADIANCE OF SANDY LOAM SOIL AS SEEN FROM SPACE FOR SEVERAL ATMOSPHERIC CONDITIONS. Parameter is horizontal visual range at the ground. Solar zenith angle = 45°, nadir view angle = 0°, vegetation background assumed.

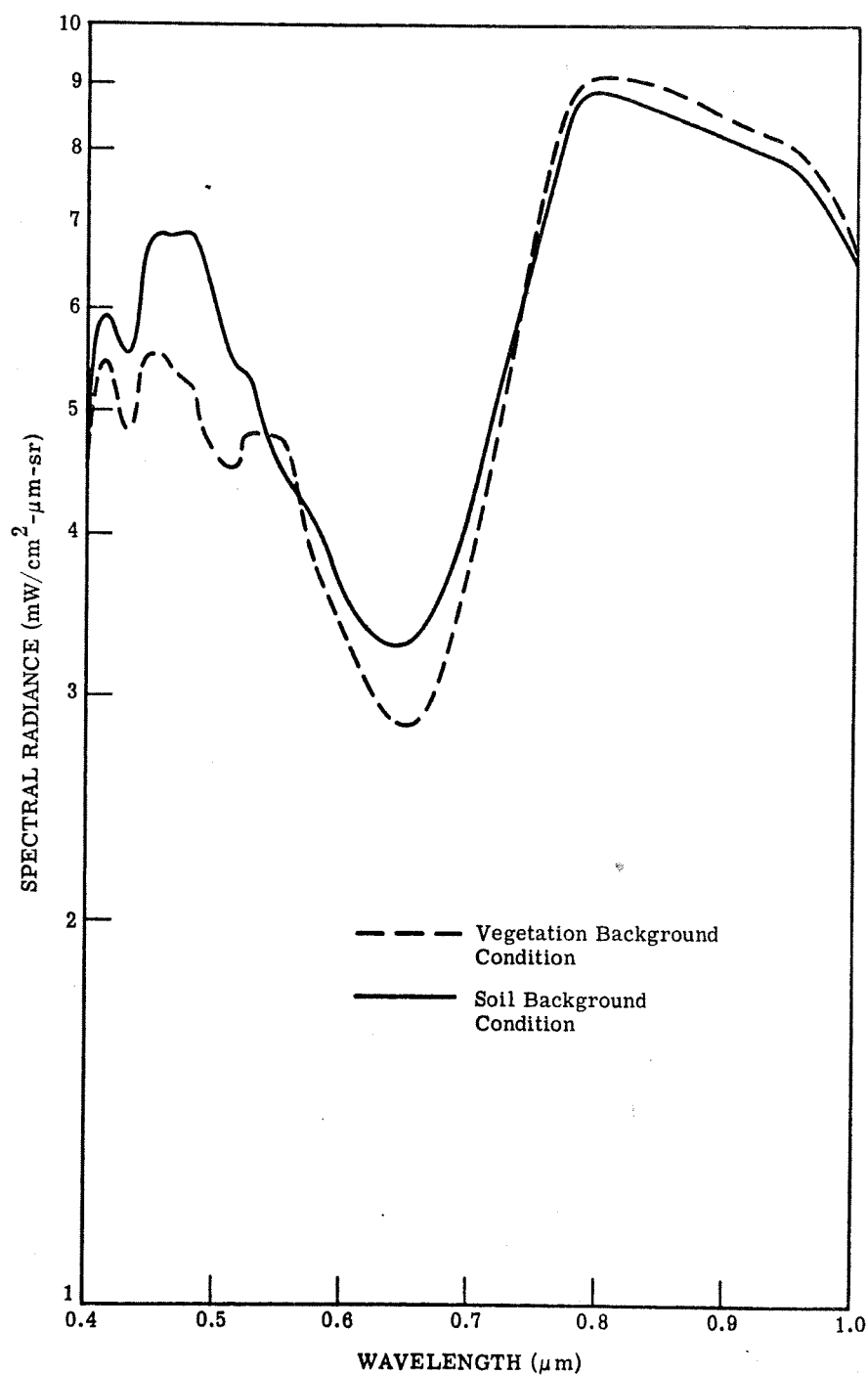


FIGURE 3. SPECTRAL RADIANCE OF CORN FIELD AS SEEN FROM SPACE FOR TWO BACKGROUND CONDITIONS. Visual range = 20 km, solar zenith angle = 45°, nadir view angle = 0°.

In summary, not only does the atmosphere alter the spectral signatures of objects observed through it, but more important, the nature of that alteration varies with atmospheric state and produces different total signature effects for different target types. In addition, when a particular target is viewed from space, the scene context within which that target is located also has a significant effect upon the character of the target's spectral signature.

1.2. THE RECOGNITION-RESOLUTION PROBLEM

Remote sensing from space has very definite geometric advantages. Large areas can be covered in a single image frame, putting targets into a large regional context. In addition, synoptic or near-synoptic observation of events occurring at widely separated points can be achieved. However, one disadvantage resulting from extended area coverage is the sacrifice in ground resolution when compared to that normally obtainable from aircraft altitudes. Nominally, the difference in linear ground resolution between a spaceborne sensor and an aircraftborne sensor of otherwise similar purpose is approximately one order of magnitude. Thus, linear spatial resolution of several tens of meters rather than several meters is normal from space. This difference can be of significance when ground phenomena with a spatial extent of even several hundreds of meters are observed.

Many phenomena can be effectively detected and mapped from space even when they exhibit dimensions significantly less than the sensor's resolution, so long as their radiometric contrast to their background is sufficient to produce detectable image contrast. For example, in many instances, roads can be detected even though their width may be only a fraction of the sensor's resolution because their material images differently than their surroundings. Thus, for urban geography, delineation of road networks is much more dependent upon the relation between resolution and road spacing than between resolution and road size. In such cases, however, the instantaneous sensor signal is only used as a threshold detection device, while actual recognition and interpretation are done by geometric analysis, often visual, of the resulting image pattern produced by many such threshold detections.

Other remote sensing applications are not so fortunate in overcoming resolution problems, however. In particular, for those applications in which the spectral character of the received signal in each resolution element is examined to make a recognition decision, the actual magnitude of the instantaneous radiometric return is of fundamental importance. Obviously, if more than one class of target is present within a single resolution element, the resultant spectral signal will be that resulting from a weighted mixing of the spectral signals of the classes present.

Computer-implemented multispectral recognition techniques are almost universally based upon the assumption (at least implicit) that each resolution element analyzed contains no mixture of target classes. At the very least, no provision is made for recognizing that a mixture is present. Such approaches have been successful and have provided useful results. However,

the application of these techniques has been almost entirely limited to aircraft-acquired multi-spectral data of relatively high spatial resolution, since suitable space data have not previously been available. Obviously, the probability that a given resolution element will contain a mixture of targets must increase as the size of the resolution element increases, so that one can expect that such problems will be of increased significance for space-acquired data.

The degree to which multispectral recognition success will be degraded in moving from aircraft to spacecraft resolutions will, of course, be dependent upon the spatial scale of the phenomenon being investigated. A case of particular interest is that of agriculture. Extensive research and application have already been conducted in use of multispectral techniques for crop identification, disease detection, and acreage measurement. Since agriculture is a cultural activity, we control, and thus have a good understanding of, the spatial scale of the phenomena involved. Consider, then, the recognition problem which arises when agricultural remote sensing is done with a 90-m square resolution element as will be the approximate case for the Earth Resources Technology Satellite (ERTS) and SKYLAB multispectral scanners. This resolution represents a square area of 2 acres for which standard multispectral recognition success requires the presence of a substantially pure sample of a desired class. If one assumes the presence of an extended agricultural area containing many fields of similar size and shape, with adjacent fields containing different crops, then one can calculate the probability that any particular 2-acre resolution element obtained while imaging that area will not contain a mixture of crops from adjacent fields. The results of such calculations are shown in Fig. 4 for the case in which the scanning is accomplished orthogonal to field boundaries (the situation is even somewhat worse otherwise). As can be seen, the result is strongly dependent upon the size of the individual fields in the area. For square fields, a size in excess of 20 acres is necessary before the probability of getting a pure target in any particular resolution element exceeds that of getting a mixture, and a field size nearly an order of magnitude greater is required for an 0.8 probability. The dashed curve in Fig. 4 shows that the situation is not dramatically improved by assuming that up to 10% impurity is tolerable.

The curves for the rectangular fields of various length to width ratios in Fig. 4 indicate that field shape is as important a factor as field area in causing mixture problems. Very small rectangular fields present greater problems than square fields, because, for a given field acreage, the minimum linear field dimension is nearer in size to the linear dimension of the resolution element. For very large rectangular fields, the problem is more generally related to the fact that there is more linear perimeter for a rectangle than for a square of equal area, and the mixture problem arises at the perimeter. The increased mixture problem associated with rectangles is especially significant because modern farming techniques are more efficiently applied to long and narrow fields requiring fewer turn-arounds per acre worked. Thus, other factors being equal, rectangular fields are preferred and are more abundant.

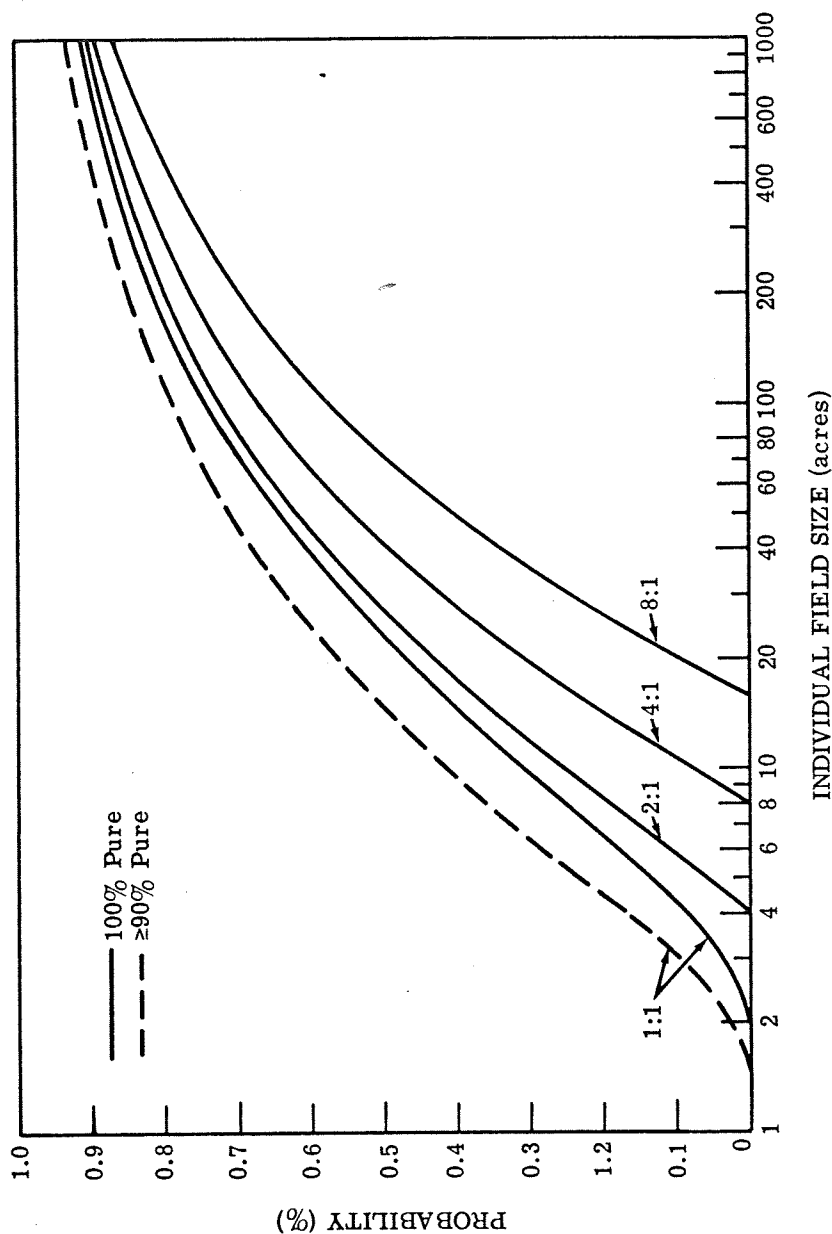


FIGURE 4. A PRIORI PROBABILITY THAT ANY PARTICULAR RESOLUTION ELEMENT WILL CONTAIN A MIXTURE WHEN IMAGING EXTENDED CHECKERBOARD FIELD PATTERN. Resolution element assumed = 90-meter square (2 acres) and scanned orthogonal to field boundaries. Parameter is length to width ratio of individual fields.

This example of the potential mixture problem for multispectral recognition of agricultural phenomena observed from space can, of course, be extended to include potential problems for other disciplines. It is significant to note, for example, that naturally occurring phenomena such as forest stands are likely to have irregular boundaries. This will lead to a greater perimeter length per enclosed acre than for agricultural fields and will create more of a problem with mixtures of targets within resolution elements for a given standing acreage. In any case, since a significant percentage of resolution elements may well contain mixtures of targets, recognition results must surely be compromised when such data are analyzed by means of a processing methodology incapable of determining that a mixture exists.

1.3. SCOPE OF THIS REPORT

The program for which this document serves as the final technical report represented a rather diverse technical analysis aimed at employing the data of the SO-65 experiment to address questions and problems not previously examined. The technical scope of the program itself involved:

- (1) validation of a previously developed atmospheric radiative transfer model utilizing SO-65 experimental data
- (2) reduction of the model's necessary complexity in order to produce simplified atmospheric correction algorithms which can be of practical utility to the average user of space-acquired remote sensor data
- (3) radiometric calibration of space photography generated during the SO-65 experiment
- (4) simulation of the space data expected to be acquired from ERTS and SKYLAB-EREP sensors
- (5) analysis of the multispectral recognition potential, especially as regards the mixture problem, of future space-acquired multispectral data.

All of the above technical objectives were addressed during the program, and the technical approach, methodology and results for each are fully reported here. There existed a definite relationship between the logical processes and technical development from one result to the next. However, we feel that the standard practice of organizing a report along strict lines of development would be a disservice to the reader for two reasons: first, he would be forced to proceed methodically through each and every section in order to understand the results; and second, it would be difficult to focus the emphasis upon those results believed to be of fundamental importance. Thus, we have taken the liberty of organizing this report to emphasize what we believe to be the two aspects of this program which should have fundamental impact upon the future utility of remote sensing from space. In particular, the discussion of results (Section 2) focuses on the application and utility of the simplified atmospheric correction techniques de-

veloped and on the demonstration of a method for overcoming the mixtures problem associated with the rather coarse spatial resolution to be produced by space-borne remote sensors. Next, Section 3 presents the methodology for calculating atmospheric effects. This methodology is broken down into a step-by-step routine which requires minimal insight and understanding to follow and which is directly amenable to implementation as a computer program table. Discussions of the basic physical phenomena causing atmospheric effects as well as presentation of the mathematical formulations comprising the model by which the phenomena are quantitatively described are relegated to the appendices. Many readers will be familiar with these aspects of the problem since the phenomena themselves have been understood for some time and since the general mathematical treatments have been developed and reported previously. Finally, Sections 4, 5, and 6 describe, respectively, the model validation, space photography calibration and space remote sensor simulation which were accomplished with the use of the data available from the SO-65 experiment.

DISCUSSION OF RESULTS

2.1. THE ANSWER TO THE ATMOSPHERIC PROBLEM

Given a physical description of the constituents of the atmosphere, an understanding of the laws and effects governing the interaction between that matter and electromagnetic radiation, and a solvable mathematical description of the mechanics of that interaction in a bounded medium, one has, upon synthesis, an atmospheric radiative transfer model. The radiometric character of any atmospheric state may then be determined so long as one can describe that state in the terms required by the model. It is at this point that the utility and practicality of mathematical modeling may fall short, for often input information necessary to a calculation is as complex and difficult to obtain as the final answer which follows from that input. The practical utility of a model can be measured in terms of the simplicity and availability of the input information required to achieve acceptable and useful accuracy of output, and the ease and speed by which input data may be manipulated to produce the output result.

2.1.1. MODEL INPUT REQUIREMENTS

The appendices describe the general matter-radiation interactions within Earth's atmosphere and present the mathematical constructs to effect solution of the resultant equations. Despite apparent complexity, the model actually requires four types of information: (1) a definition of the sun-target-sensor geometry; (2) a definition of the density and distribution of gaseous molecules in the atmosphere; (3) a definition of the density and distribution of aerosol particles in the atmosphere; and (4) a definition of the spectral reflectance characteristics of the terrain surrounding the target. Operation of the model thus requires either specification of this information directly, or specification of auxiliary information from which the model can itself quantitatively define the required information.

Specification of the sun-target-sensor geometry is relatively easy, particularly since these parameters are controllable through choice of the time, place, and sensor orientation for data collection. In any case, present and future space sensors are tightly controlled in their orientation, thus fixing the sensor-target geometry. In addition, it has become standard practice to report the angular position of the sun with respect to the target area for all space-acquired remote sensor data.

The density and altitude distribution of gaseous molecules in the atmosphere is not commonly available for specific sites and specific times; nor is there usually a measure of the exact chemical constitution of the atmosphere. However, certain characteristics simplify the problem. First, the only gas exhibiting significant absorption in the 0.4- to 0.7- μ m spectral range is ozone.* Since most of the ozone is concentrated above the region where significant scattering occurs, ozone can be treated as an extra-atmospheric absorbing layer and its effects

*Water vapor can produce significant absorption of wavelengths greater than 0.75 μ m for moist atmospheres. However, this absorption is spatially distributed throughout the scattering medium so that the present model cannot calculate the effect in a unified manner.

calculated independently of all other gases. Second, all atmospheric gases of significant concentration have molecular diameters much less than the wavelength of the radiation of interest. The scattering character therefore becomes, not a function of chemical composition, but only a function of number density. Finally, the total number of gas molecules in a vertical path between Earth's surface and space is measurable by means of the atmospheric pressure at that point on the surface, and their relative density distribution with altitude above the surface is essentially constant, spatially and temporally. Thus, the atmospheric pressure at Earth's surface in the target area provides all the information required to define adequately the molecular scattering character in the atmosphere above the target.

The density and distribution of aerosol particles in the atmosphere is perhaps the least accessible type of information required by the model. This is unfortunate since the aerosol content is the most variable factor defining the state of the atmosphere. As discussed in Appendix I, turbidity measurements can provide a direct measure of the required atmospheric aerosol information. However, such measurements are not commonly made nor reported, even in the United States at this time. Another source for aerosol information may be the air pollution monitoring networks which are rapidly increasing, at least in the United States. Unfortunately, such monitoring measures only solid particulate content and ignores the water droplets which are the most significant factor in aerosol scattering.* Temperature and humidity measurements, especially radiosonde profiles, may ultimately provide a usable measure of aerosol concentration and distribution. We are, in fact, left with only one indirect measure of aerosol content which is routinely available at most places and at most times, the horizontal visual range at the ground which is reported routinely from all U.S. Weather Bureau Stations usually on an hourly basis.

As discussed in Appendix I, extensive empirical investigation has resulted in a statistically quantitative definition of the relationship between visual range and the number density, altitude distribution, and size distribution of aerosols. By employing visual range as a model input, one can expect to be quantitatively correct in assessing aerosol effects, at least on the average. Obviously, for specific instances the error may be significant. Another potential source of error results because the visual range itself is usually determined by a human observer and is essentially an estimate of how far he can see. Meteorologists use fixed landmarks of known distances for this purpose, and accuracy depends upon the number and distance interval between the suitable landmarks available at a particular station. The error in determining the visual range is thus dependent upon the site condition of the particular station, while the error in associating visual range and aerosol characteristics is dependent upon the degree to which the particular haze condition departs from the norm. Some feeling for the level of significance of such errors can be derived from Figs. 1 and 2 of the previous section. In these figures, each parametric visual range value is essentially twice the value of its successor, while each

*In several major cities, however, two-channel VOLZ photometers are now being used to measure the total scattering effect. Where such data are available, the aerosol optical depth may be specified directly without use of visual range (see Section 3.2).

WILLOW RUN LABORATORIES

parametric radiance curve represents a 5% to 10% total radiance change on the average. It would then appear that errors in estimating visual range of about +50% to - 30% would still produce acceptably accurate model calculations for the vast majority of cases.

The fourth and final type of information required by the model is a description of the average spectral reflectance of the terrain surrounding the target. This information is necessary since solar radiation reflected from the surrounding terrain is available for subsequent scattering to produce both additional irradiance onto the target and, more importantly, to produce a portion of the observed path radiance. Obviously, an actual measurement of the spectral total reflectance (spectral albedo) of each terrain component surrounding the target is usually unfeasible. In fact, if such ground truth effort could be accomplished the need for remote observation of the target itself would be largely obviated. Certain simple cases are apparent. In particular, if the surrounding terrain is constituted of a single component (e.g. all water, all forest, or all desert sand), the problem may be as simple as retrieving typical reflectance data from the literature or from a data library, or at worst from a very limited ground excursion.

More complex terrain conditions do require somewhat more complex albedo analysis, however. Agricultural areas typically contain major components of bare soil, various crops, and often natural vegetation and water as well. An average spectral albedo, weighted according to the relative abundance of each component, must be determined. In this case, it is important to realize that perhaps 90% of the albedo effect can be evaluated by determining the percentage of terrain area in each of a very small number of general spectral classes. For example, one class would consist of all healthy green vegetation, another of all dry (bright) soil, another of all damp (dark) soil, and the last, of all standing water. To each class, one would then assign nominal spectral reflectance for that class of target. Separation into such gross classifications and determination of the relative abundance of each can usually be accomplished quite simply from aircraft photography or scanner imagery or even from the space data itself.

In working in a mixed background condition, however, one must define the geographic limits of the area centered around the target which can be expected to affect the radiometric character of the atmosphere over the target. No extensive investigation of this effective range has been made. However, certain guidelines can be specified. In particular, it can be assumed that any terrain area with a distance more than one mean-free path of a photon from the target will not have significant effect. While the mean-free path is dependent upon wavelength and atmospheric state, a good average measure is produced by taking one-fourth the value of the visual range (this is approximately equal to the mean-free path at $0.55 \mu\text{m}$). Thus, if the visual range is 10 km, albedo analysis can be restricted to a circle of about 2.5-km radius centered on the target. If the visual range exceeds 20 km, the effective radius for albedo analysis should not be extended beyond about 5 km, however, since even for large visual ranges, the background albedo effect from areas more than 5 km distant greatly diminishes.

2.1.2. MODEL ACCURACY

Determination of the overall accuracy of the atmospheric radiative transfer model and of the simplified calculational procedures of Section 3 was a fundamental objective of this program. Appendix II lists previous validation analyses which showed excellent agreement between calculation and experimental measurement of the spectral and spatial sky radiance distribution as seen when looking up from Earth's surface. These analyses have been taken as a strong indication that the model should also produce accurate results when calculating atmospheric effects upon surface targets seen from space. However, it was not until the validation analysis of the present program was completed that this indication was confirmed.

The preceding discussion indicates that the input requirements necessary to utilize the calculational procedures are indeed quite simple and of general availability. The geometric relationship of sensor-target-sun is commonly supplied as annotation to space-acquired remote sensor data. The atmospheric pressure and the visual range at the surface are measured and reported by all stations of the U.S. Weather Bureau and are generally available in other countries. Only the background terrain albedo information requires additional data of the remote sensor user who wishes to calculate the atmospheric effects present in his data. In this case, however, rather simple photointerpretation and photogrammetry together with access to generally available spectral reflectance data will provide sufficient information for the purpose.

Section 4 of this report provides a detailed description of the methodology and results of the validation analyses. The radiometrically-calibrated multispectral line scanner data gathered in the SO-65 experiment provided the data base necessary for the analysis. Comparison of total radiance measurements derived from two flight altitudes allowed quantitative assessment of the atmospheric effects without the need for calibrated ground reference targets.* While the highest flight altitude was 3.3 km (10,000 ft), the validation results should be indicative of calculational accuracy for space sensors since the bulk of the atmospheric effect occurs at altitudes below 3 km, especially as regards aerosol scattering which is the most variable aspect of the atmospheric state.

Specific results of the validation analysis comparing measured atmospheric effects to those calculated by the model will not be presented in this section. The rather complex nature of the analyses conducted and the specific implications of the results obtained require the fullness of discussion present in Section 4. However, the general conclusions supported by the specific

*The fully-implemented atmospheric model can calculate the atmospheric effects on remote sensor data obtained from any altitude and from any look direction. However, the simplified procedures of Section 3 apply only to a sensor located outside the atmosphere viewing Earth within 15° of the nadir.

WILLOW RUN LABORATORIES

results can be summarized as follows:

- (1) Agreement between experiment and the model was good for all wavelengths longer than $0.45 \mu\text{m}$. At the one available scanner wavelength shorter than $0.45 \mu\text{m}$, the presence of a significant systematic disagreement between experimental and calculated data appeared to be the result of scanner calibration uncertainties rather than a model defect.
- (2) Uncertain knowledge of the exact values of the input data required by the model leads to uncertainties in calculated results which are generally greater than any systematic disagreement between model calculations and experimental data.
- (3) Use of visual range as the only input parameter for specifying atmospheric aerosol distribution can lead to some calculation error, especially for very highly reflecting targets sensed from low aircraft altitudes, even though the results should be correct in an average statistical sense. Such possibility of calculational error should decrease for higher sensor altitudes and for average target reflectances.

2.2. ONE ANSWER TO THE RECOGNITION-RESOLUTION PROBLEM

A significant percentage of the resolution elements in data acquired over typically-sized targets contains a mixture of target types, and thus contains spectral signatures characteristic of that mixture. Standard multispectral recognition techniques do not provide for such a situation. The obvious solution to that problem is to utilize a multispectral recognition technique which can recognize the presence of such a mixture and which can then define the proportions of the individual classes which produced that mixture.

Significant work has been accomplished on another NASA-sponsored program to effect a solution to this problem.* The program being reported herein calls upon the basic techniques previously developed, together with the data available from the SO-65 experiment, in order to provide a test of the utility and accuracy of the mixtures recognition approach.

Section 6.3 discusses the nature of the multispectral mixtures recognition algorithm presently available and describes in detail the method by which the approach was tested and compared to results derived from a standard multispectral recognition algorithm. Table 1 presents the results of tests conducted with multispectral data of 76-m square (250-ft square) spatial resolution obtained from the aircraft overflights of Imperial Valley associated with the SO-65 experiment. The first column of Table 1 defines the target classes; the second column gives the recognition results obtained (total proportion of the 18,600 acres processed) with the standard recognition algorithm; the third column gives the results obtained with the mixtures algo-

*Contract NAS9-9784, NASA Manned Spacecraft Center.

WILLOW RUN LABORATORIES

TABLE 1. PROPORTIONS OF VARIOUS TARGET CLASSES
IN 18,600 ACRES OF IMPERIAL VALLEY

	Standard Recognition (%)	Mixtures Recognition (%)	Ground* Truth (%)
Barley	7.9	15	20
Cut Alfalfa	8	9.4	--
Alfalfa	10	18.8	--
Lettuce	0.5	6	5.4
Weeds	9	4.5	--
Bedded and Disced Soil	17.1	16.1	--
Fallow Soil	8.3	15.6	--
Other	39.2	14.6	23.6 (+ Weeds)

*Accurate area measures for some classes could not be obtained. For others, only combined measures as shown could be accurately determined.

rithm; and the last column gives the results determined from extensive ground truth observation conducted during the SO-65 experiment.

The results shown in Table 1 provide a persuasive argument for the mixtures recognition approach. For the classes cut alfalfa plus alfalfa, lettuce, and weeds plus others, the agreement between the mixtures proportions and the ground truth is excellent. For barley, the mixtures proportion is less than the ground truth estimate, but indicative of the fact that the ground truth defines a barley field as being entirely barley, while the mixtures recognition should recognize only that proportion constituting full-leaf area coverage by crop, and classify any patches of soil showing elsewhere. Thus, the mixtures recognition indicates an average barley crop cover of 75% of the field. This is not much different from a mean value (based upon field count and not area count) of 80 to 85% estimated on the ground. For the bare soil areas, the mixtures recognition produces a higher estimated proportion than indicated by ground truth. The argument for barley, in reverse, can account for at least some of this difference. In addition, dirt roads and other such nonproductive bare soil areas would have been recognized as soil by the mixtures recognition, but classed as other by the ground truth.

The agreement obtained for the mixtures recognition is not achieved in the standard recognition results. For the vegetative targets, the estimated proportions seem much too low to be accounted for by the previous leaf area argument. In addition, the proportion of other (not classified) is significantly greater than indicated by the ground truth. Only the soil proportion can be justified by reasonable arguments other than that the standard recognition approach was not adequate for the job required.

In summary, it would appear that, at least for this data set, the problem of target mixtures within large resolution elements can be handled by the convex mixtures approach. The results are in very good agreement with ground observations and appear much superior to those produced by the standard recognition technique.

SIMPLIFIED ATMOSPHERIC CORRECTION TECHNIQUES

The present section constitutes a simplified methodology for utilizing the results of the model for space-acquired data so that any user may correct space-acquired data for atmospheric effects.* The narrative describes the step by step procedures necessary to calculate the required functions without attempting to justify those steps. Given a space-borne sensor which produces a quantitative radiometric measure of a target's radiance, L^t , this section defines how one determines the target's effective diffuse reflectance, $\rho^{t\dagger}$ where ρ^t is given by:

$$\rho^t = \frac{\pi(L^t - L_p)}{E_g T_v} \quad (2)$$

The technique for determining the total atmospheric transmittance, T_v , along the viewing path is given in Section 3.2. The technique for determining the total path radiance, L_p , coming from the viewing path is given in Section 3.3. The technique for determining the total irradiance onto the target, E_g , is given in Section 3.4.

3.1. INPUT REQUIREMENTS AND DEFINITIONS

Certain descriptive parameters of the atmospheric state, the general scene content, and the sensor-target-sun geometry are required as inputs necessary to utilize the data in Sections 3.2, 3.3 and 3.4. The following definitions are used:

V = Visual Range, defined to be that horizontal distance (km) at the ground for which the apparent difference in radiance between two resolved objects is decreased to 2% of the actual difference, all data pertaining to 0.55- μ m wavelength. The visual range or visibility reported by United States Weather Bureau stations represents a reasonable approximation to V .

P = Station Pressure, defined to be that atmospheric pressure (mbar) actually measured at the ground, with no compensation or correction for altitude above sea level. This parameter is a standard measured and reported item for U.S. Weather Bureau stations.

$\bar{\rho}$ = Mean Background Terrain Spectral Albedo, defined to be the area-weighted average diffuse spectral reflectance for those terrain components in the vicinity of the target (i.e., within about 5 km). This parameter must usually be estimated by use of ground truth or remote sensor data to determine scene content, and use of library reflectance data (e.g., ERSIS [3]) to define the diffuse reflectance of the various materials present.

θ_0 = Solar Zenith Angle, defined to be the angle measured from the gravitational vector to the vector defining the direction of travel of unscattered solar radiation into the target area (Fig. 5).

*See Section 5.2 for a discussion of the meaning of ρ^t .

[†] The limitation of this simplified approach over the general model rests with the treatment for non-nadir viewing angles as discussed in Section 3.3.

ϕ_0 = Solar Azimuth Angle, defined to be the angle measured clockwise from the true north direction to the projection onto a horizontal plane of the vector defining the direction of the sun from the target area (Fig. 5).

θ_v = Nadir View Angle, defined to be the angle measured from the gravitational vector to the vector defining the direction of view from the sensor to the target (Fig. 5).

ϕ_v = Azimuth View Angle, defined to be the angle measured clockwise from the true north direction to the projection onto a horizontal plane of the vector defining the direction of view from the sensor to the target (Fig. 5).

3.2. TOTAL ATMOSPHERIC TRANSMITTANCE, T_v

This section provides data and procedures for the calculations of T_v :

$$T_v = T_0(\lambda, P, V, \theta_v) T_{\text{ozone}}(\lambda, \theta_v)$$

3.2.1. $T_0(\lambda, P, V, \theta_v)^*$

(a) For the particular λ , read τ_{R0} from Fig. 6.

(b) For the particular P , calculate τ_R using (a)

$$\tau_R = \tau_{R0} \left(\frac{P}{1013} \right)$$

(c) For the particular V , read τ_A from Fig. 7 for the desired λ . For λ between the given values λ_i , read $\tau_A(V, \lambda_i)$ and $\tau_A(V, \lambda_{i+1})$, plot these two values as $\log \tau_A$ versus $\log \lambda$, draw a straight line between points and read τ_A at desired λ .

(d) Calculate τ_{00} using (b) and (c) above

$$\tau_{00} = \tau_R + \tau_A$$

(e) Calculate τ_0 using (d) above

$$\tau_0 = \frac{\tau_{00}}{\cos \theta_v}$$

(f) For τ_0 read $T_0(\lambda, P, V, \theta_v)$ from Fig. 8 or calculate

$$T_0(\lambda, P, V, \theta_v) = e^{-\tau_0}$$

*If some direct measure of τ_0 at a particular wavelength is available, steps (d) through (e) may be worked in reverse to solve for τ_A at that wavelength. Then, using Fig. 3.3, the effective V may be defined and used for determining τ_A at other wavelengths.

3.2.2. $T_{\text{ozone}}(\lambda, \theta_v)$

(a) For the particular λ , read τ_{ozone} from Fig. 9

(b) Using (a) above, calculate

$$\tau_{\text{ozone}}(\theta_v) = \frac{\tau_{\text{ozone}}}{\cos \theta_v}$$

(c) For $\tau_{\text{ozone}}(\theta_v)$ read $T_{\text{ozone}}(\lambda, \theta_v)$ from Fig. 8, or calculate

$$T_{\text{ozone}}(\lambda, \theta_v) = e^{-\tau_{\text{ozone}}(\theta_v)}$$

3.3. TOTAL PATH RADIANCE, L_p

This section provides data and procedures to calculate L_p in the following form:

$$L_p = [F(\lambda, T_0, \tau_0, \tau_{R0}, \tau_R, \theta_0, \phi_0, \theta_v, \phi_v) + G(\lambda, T_0, \tau_0, \tau_{R0}, \tau_R, \theta_0, \phi_0, \theta_v, \phi_v)H(\lambda, \tau_{00}, \tau_R, \bar{\rho})] \\ \times T_{\text{ozone}}(\lambda, \theta_0, \theta_v)E_0(\lambda)$$

The quantities F and G must be calculated at the particular λ_i provided. The quantity H can, however, be calculated at the actual λ desired. In any case, if L_p is desired at some wavelength λ between λ_i and λ_{i+1} , then interpolation should be accomplished by means of the entire quantity $[F + GH]$ by plotting $\log [F(\lambda_i) + G(\lambda_i)H(\lambda_i \text{ or } \lambda)]$ versus $\log \lambda_i$. Those quantities from Section 3.2.1. used here to determine F, G, and H must be those applicable to the particular wavelength at which F, G, and H are being individually determined. Because of mathematical complexity, only approximate methods for determining F and G for $\theta_v \neq 0$ are provided. The approximation leads to errors in L_p (as compared to the exact model calculations) of less than $\pm 10\%$ for $\theta_v \leq 15^\circ$. The errors increase significantly for $\theta_v > 15^\circ$.

3.3.1. $F(\lambda_i, T_0, \tau_0, \tau_{R0}, \tau_R, \theta_0, \phi_0, \theta_v, \phi_v)$

(a) Calculate

$$\theta_s = \cos^{-1} [\cos \theta_v \cos \theta_0 + \sin \theta_v \sin \theta_0 \cos (\phi_v - \phi_0)]$$

where $\theta_s = \theta_0$ for $\theta_v = 0^\circ$

(b) From among Figs. 10a, 10b, 10c, 10d, and 10e, choose the graph corresponding to the desired λ_i . Using (a) above, read F_0 for the particular θ_s and T_0 (calculated in Section 3.2.1.) required. Linear visual interpolation between the parametric T_0 curves will usually be as accurate as is justified by the accuracy of T_0 .

- (c) Using τ_0 , τ_{R0} and τ_R from Section 3.2.1, and (a) above, calculate

$$K_F = \frac{\cos \theta_s + (0.05\tau_0 + 0.45\tau_{R0})}{\cos \theta_s + \left(0.05\tau_0 + \frac{0.45\tau_R}{\cos \theta_v}\right)}$$

- (d) Calculate, using (b) and (c) above

$$F(\lambda_i, T_0, \tau_0, \tau_{R0}, \tau_R, \theta_0, \phi_0, \theta_v, \phi_v) = F_0 K_F$$

3.3.2. $G(\lambda_i, T_0, \tau_0, \tau_{R0}, \tau_R, \theta_0, \phi_0, \theta_v, \phi_v)$

- (a) From Figs. 11a, 11b, and 11c choose the graph corresponding to the desired λ_i . Read G_0 for the particular θ_0 and T_0 (calculated in Section 3.2.1) required. Linear visual interpolation between the parametric T_0 curves will usually be as accurate as is justified by the accuracy of T_0 .

- (b) Using τ_0 , τ_{R0} and τ_R from Section 3.2.1, calculate

$$K_G = \left[\frac{\cos \theta_0 + (0.05\tau_0 + 0.45\tau_{R0})}{\cos \theta_0 + \left(0.05\tau_0 + \frac{0.45\tau_R}{\cos \theta_v}\right)} \right] \left[\frac{1 + 4\left(0.05\tau_0 + \frac{0.45\tau_R}{\cos \theta_v}\right)}{1 + 4(0.05\tau_0 + 0.45\tau_{R0})} \right]$$

- (c) Calculate, using (a) and (b) above

$$G(\lambda_i, T_0, \tau_0, \tau_{R0}, \tau_R, \theta_0, \phi_0, \theta_v, \phi_v) = G_0 K_G$$

3.3.3. $H(\lambda, \tau_{00}, \tau_R, \bar{\rho})$

- (a) Using τ_{00} and τ_R from Section 3.2.1, calculate directly

$$H(\lambda, \tau_{00}, \tau_R, \bar{\rho}) = \frac{\bar{\rho}}{1 + 2(1 - \bar{\rho})(0.05\tau_{00} + 0.45\tau_R)}$$

- (b) Alternatively, if $\tau_R = \tau_{R0}$, use τ_{00} from Section 3.2.1 and read T_{00} from Fig. 8, or calculate

$$T_{00} = e^{-\tau_{00}}$$

where $T_{00} = T_0$ for $\theta_v = 0^\circ$

- (c) From Figs. 12a, 12b, and 12c, choose the graph corresponding to the desired λ_i . Using (b) above, read H for the particular T_{00} and $\bar{\rho}$ required.* Linear visual interpolation between parametric $\bar{\rho}$ curves will usually be as accurate as is justified by the accuracy of $\bar{\rho}$.

3.3.4. $T_{\text{ozone}}(\lambda, \theta_0, \theta_v)$

- (a) For the particular λ , read τ_{ozone} from Fig. 9.

- (b) Using (a) above, calculate

$$\tau_{\text{ozone}}(\lambda, \theta_0, \theta_v) = \tau_{\text{ozone}} \left(\frac{1}{\cos \theta_0} + \frac{1}{\cos \theta_v} \right)$$

- (c) For $\tau_{\text{ozone}}(\lambda, \theta_0, \theta_v)$ read $T_{\text{ozone}}(\lambda, \theta_0, \theta_v)$ from Fig. 18, or calculate

$$T_{\text{ozone}}(\lambda, \theta_0, \theta_v) = e^{-\tau_{\text{ozone}}(\lambda, \theta_0, \theta_v)}$$

3.3.5. $E_0(\lambda)$

For the particular λ , read $E_0(\lambda)$ from Fig. 13.

3.4. TOTAL IRRADIANCE, E_g

This section provides data and procedures to calculate E_g in the following form:

$$E_g = I(\lambda, \tau_{00}, \tau_R, \theta_0) [1 + J(\lambda, \tau_{00}, \tau_R) H(\lambda, \tau_{00}, \tau_R, \bar{\rho})] \times T_{\text{ozone}}(\lambda, \theta_0) E_0(\lambda)$$

Those quantities from Section 3.2.1 used here to determine I, J, and H must be those applicable to the λ at which the determination is being made. The quantities H and E_0 used here are identical in all respects to those described in Sections 3.3.3 and 3.3.5, respectively, and their calculation for a given condition need not be repeated.

3.4.1. $I(\lambda, \tau_{00}, \tau_R, \theta_0)$

- (a) Using τ_{00} and τ_R from Section 3.2.1, calculate

$$I(\lambda, \tau_{00}, \tau_R, \theta_0) = \frac{(\cos \theta_0)^2}{\cos \theta_0 + 0.05\tau_{00} + 0.45\tau_R}$$

*In contrast to other parameters involved in determining L_p , $\bar{\rho}$ is not necessarily a smoothly varying function of wavelength. If high accuracy is desired in determining L_p at some particular wavelength λ between given values λ_i and λ_{i+1} , and $\bar{\rho}$ varies significantly over this range, then the value of $\bar{\rho}$ for the particular wavelength of interest should be used in calculating $H(\lambda_i)$ and $H(\lambda_{i+1})$, or even better, (a) above should be used for the actual λ desired.

- (b) Alternatively, if $\tau_R = \tau_{R0}$, choose from Figs. 14a, 14b, 14c, and 14d the graph corresponding to the desired λ_i . Read $I_0(\lambda_i, \tau_{00}, \tau_{R0}, \theta_0)$ for the particular θ_0 and T_{00} (from Section 3.3.3) required. Linear visual interpolation between parametric T_{00} curves will usually be as accurate as may be justified by the accuracy of T_{00} .

3.4.2. $J(\lambda, \tau_{00}, \tau_R)$

- (a) Using τ_{00} and τ_R from Section 3.2.1, calculate

$$J(\lambda, \tau_{00}, \tau_R) = 2(0.05\tau_{00} + 0.45\tau_R)$$

- (b) Alternatively, if $\tau_R = \tau_{R0}$, read $J_0(\lambda_i, \tau_{00}, \tau_{R0})$ from Fig. 15 using the particular λ_i and T_{00} (from Section 3.3.3) required.

3.4.3. $T_{\text{ozone}}(\lambda, \theta_0)$

Follow the procedure defined in Section 3.2.2, but using θ_0 rather than θ_v , to determine $T_{\text{ozone}}(\lambda, \theta_0)$.

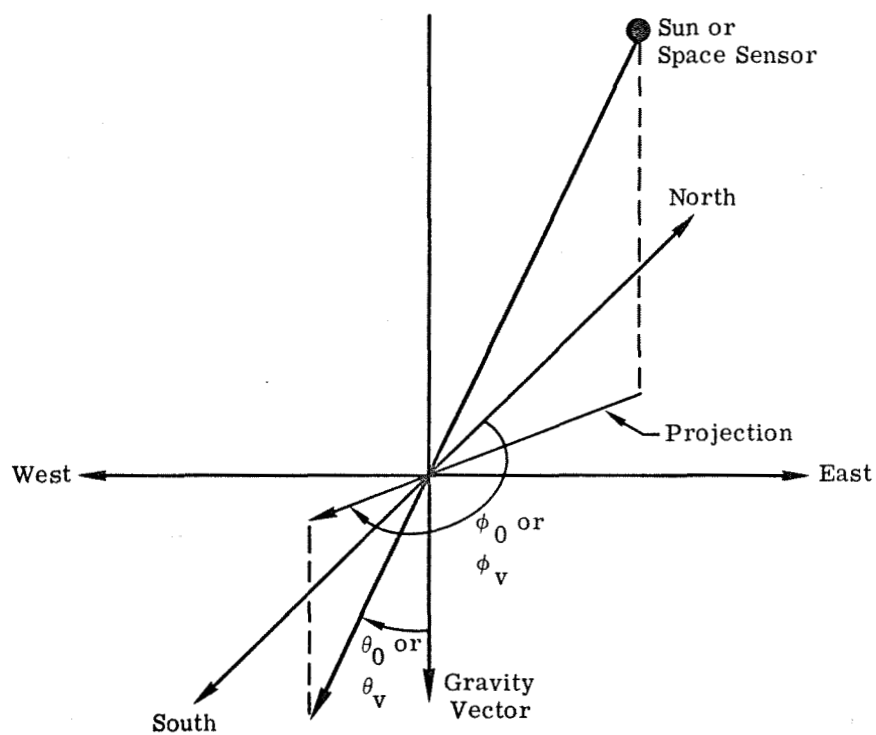


FIGURE 5. GEOMETRY DEFINING SOLAR AND VIEW ANGLES

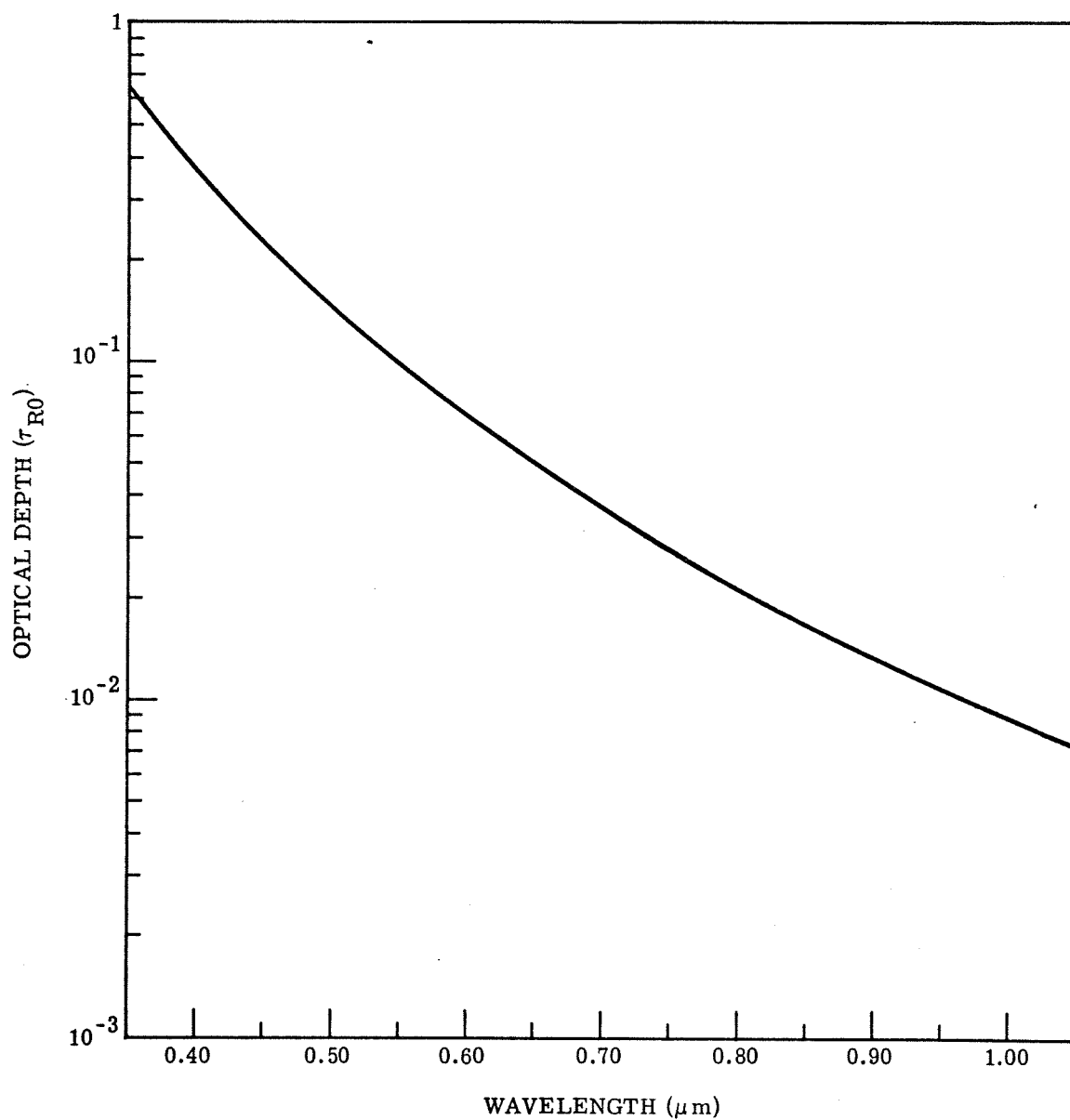


FIGURE 6. DEPENDENCE OF TOTAL RAYLEIGH OPTICAL DEPTH τ_{R0} ON WAVELENGTH
FOR UNITED STATES STANDARD ATMOSPHERE

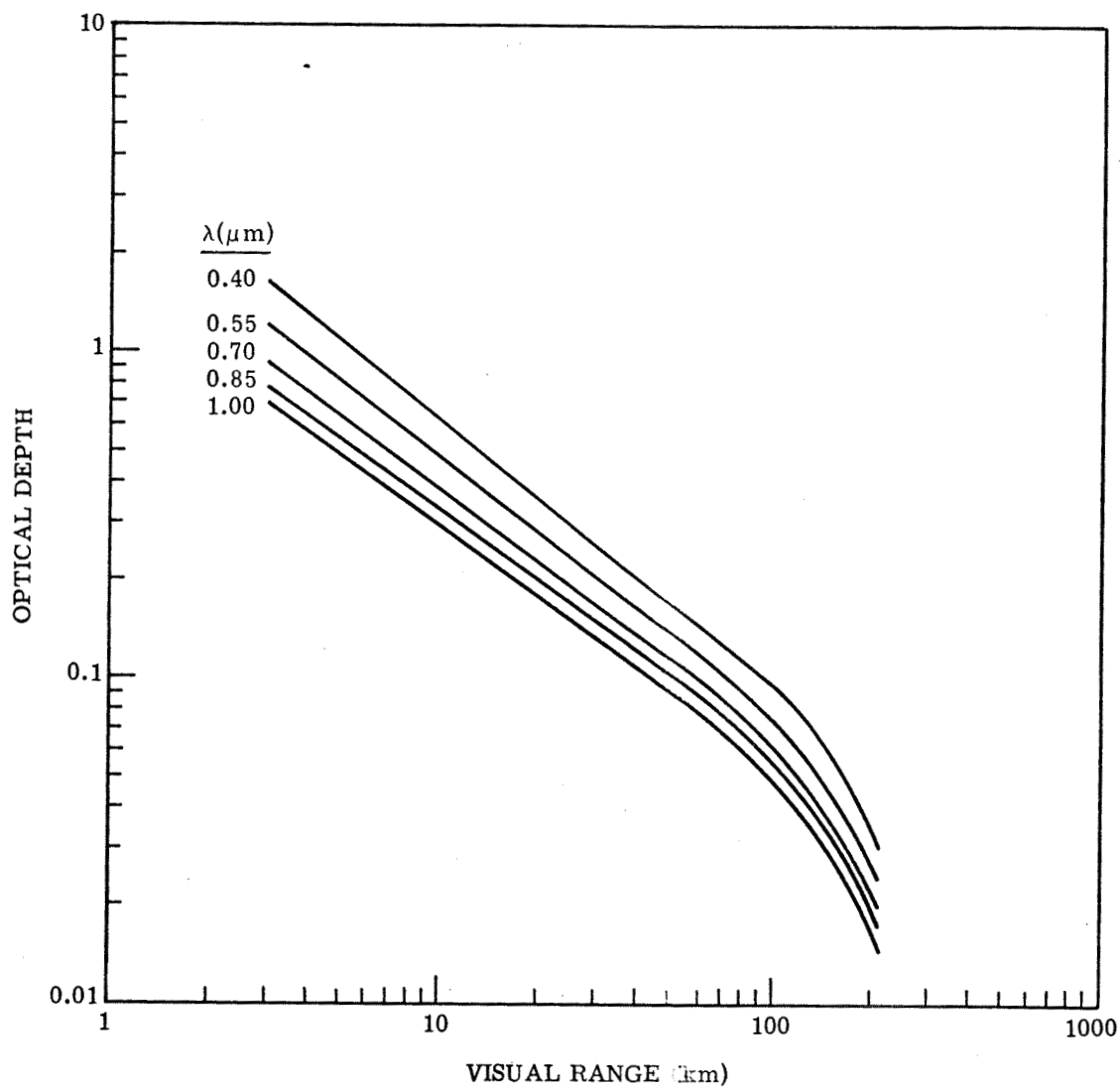


FIGURE 7. AEROSOL OPTICAL DEPTH τ_A VERSUS VISUAL RANGE V . Parameter is spectral wavelength, λ .

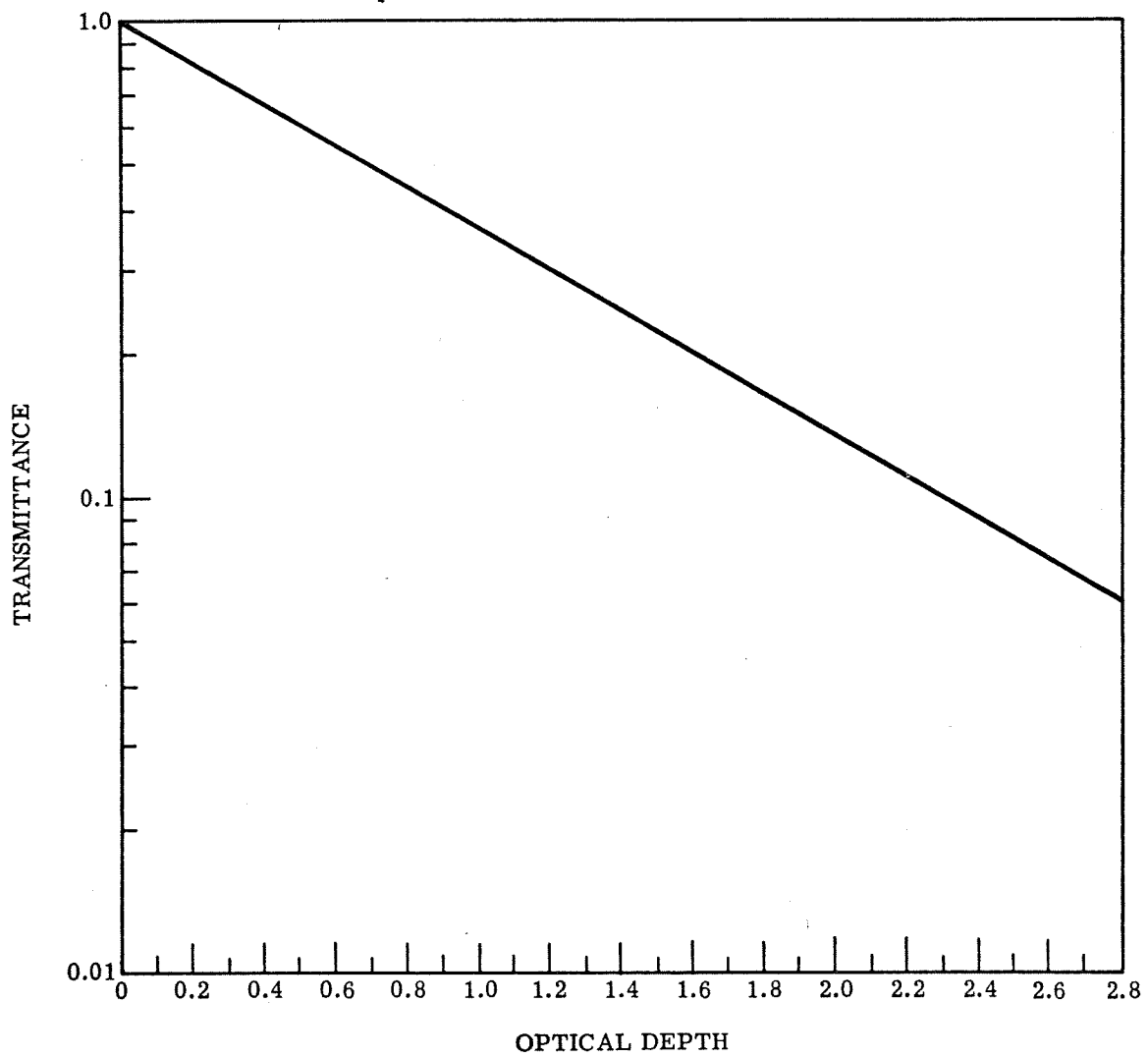


FIGURE 8. TRANSMITTANCE T VERSUS OPTICAL DEPTH τ

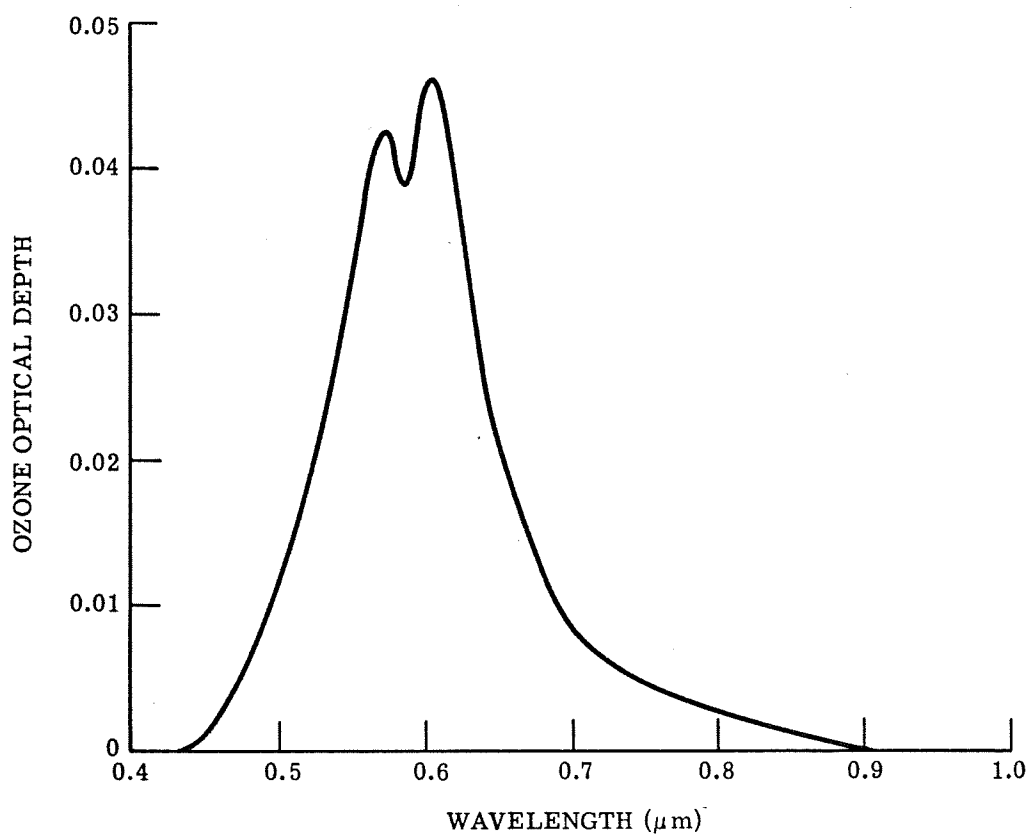
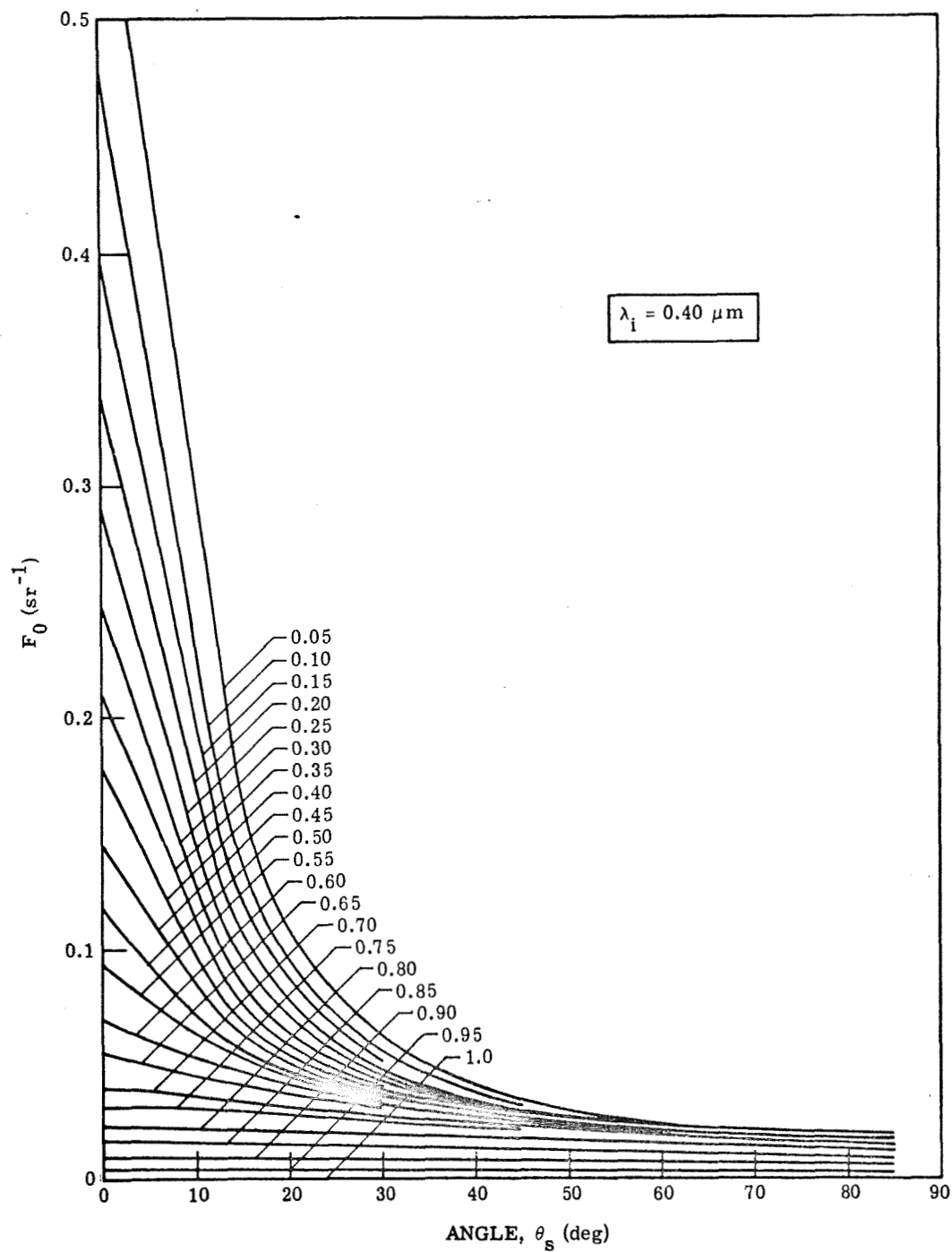
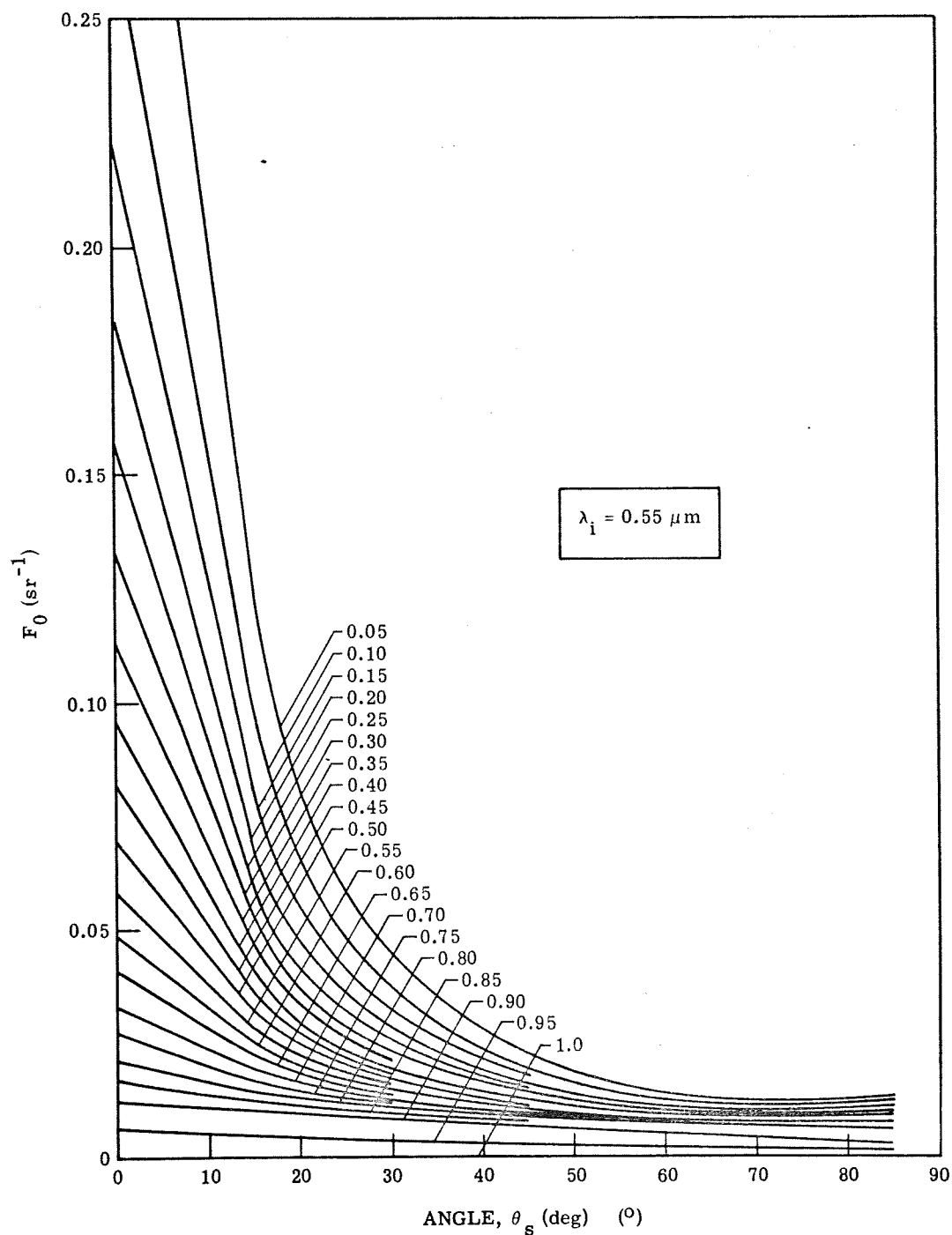


FIGURE 9. AVERAGE OZONE OPTICAL DEPTH τ_{ozone} VERSUS WAVELENGTH λ [28]



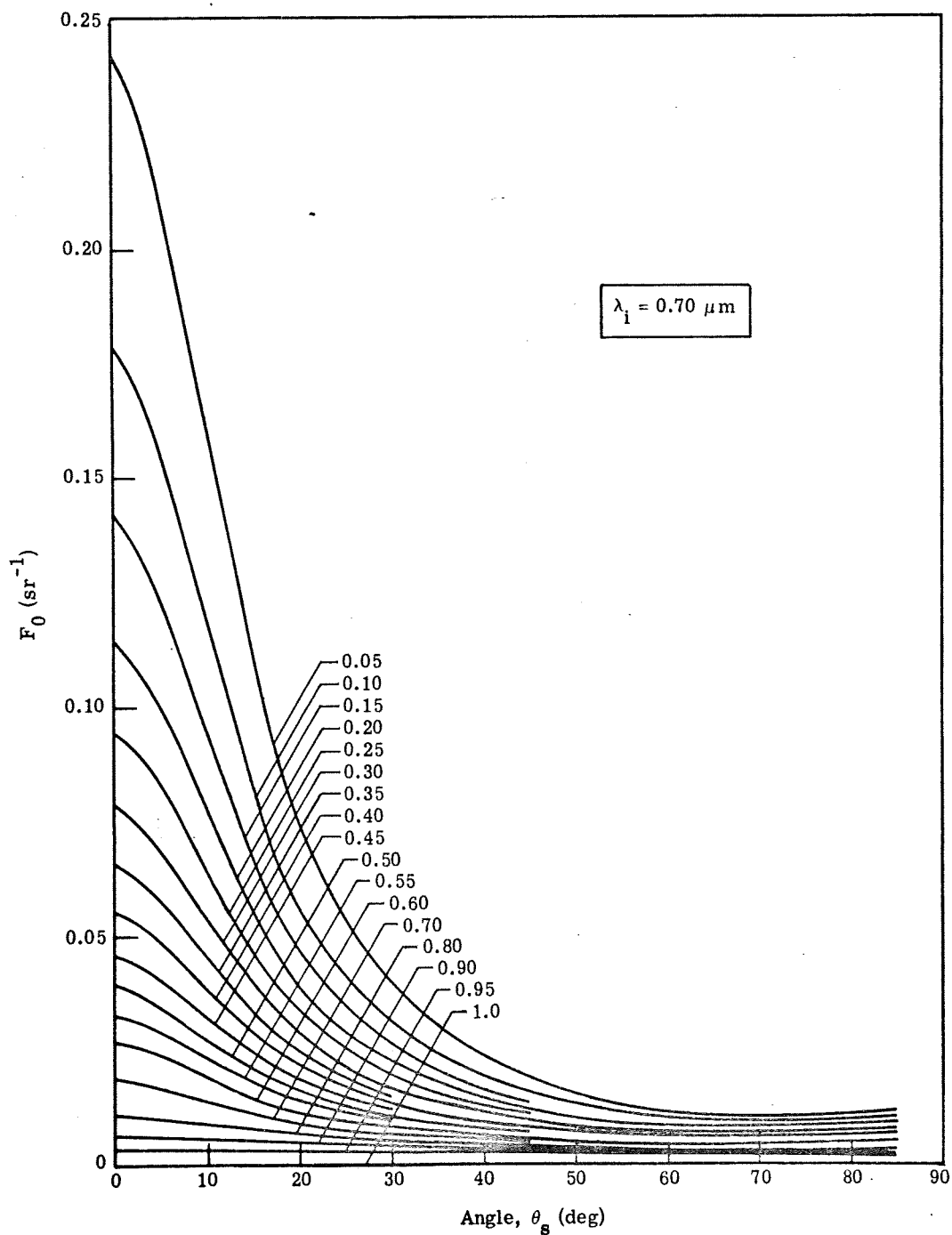
(a)

FIGURE 10. RADIANCE FUNCTION F_0 VERSUS DERIVED ANGLE θ_s . Parameter is atmospheric transmittance T_0 .



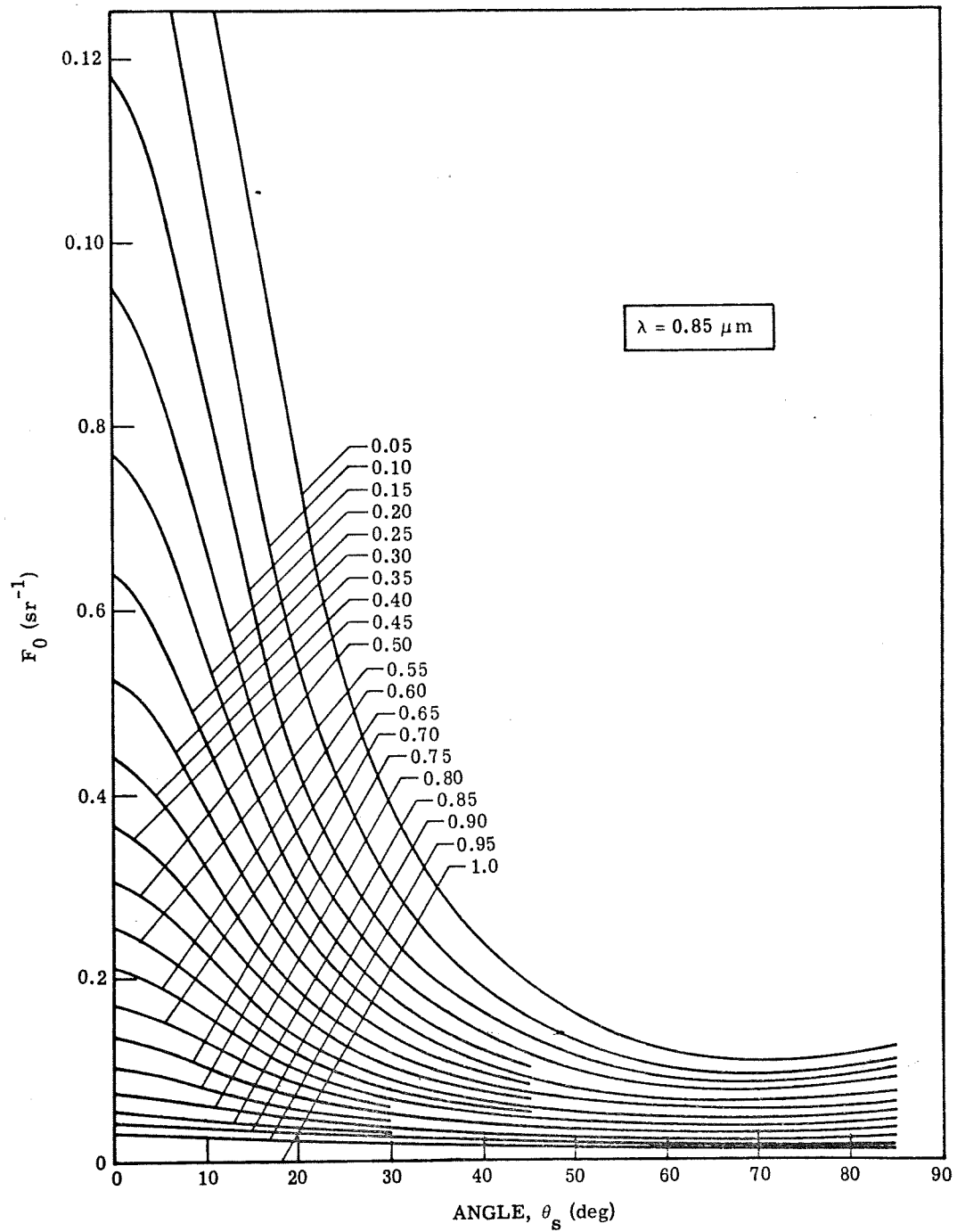
(b)

FIGURE 10. RADIANCE FUNCTION F_0 VERSUS DERIVED ANGLE θ_s . Parameter is atmospheric transmittance T_0 (Continued).



(c)

FIGURE 10. RADIANCE FUNCTION F_0 VERSUS DERIVED ANGLE θ_s . Parameter is atmospheric transmittance T_0 (Continued).



(d)

FIGURE 10. RADIANCE FUNCTION F_0 VERSUS DERIVED ANGLE θ_s . Parameter is atmospheric transmittance T_0 (Continued).

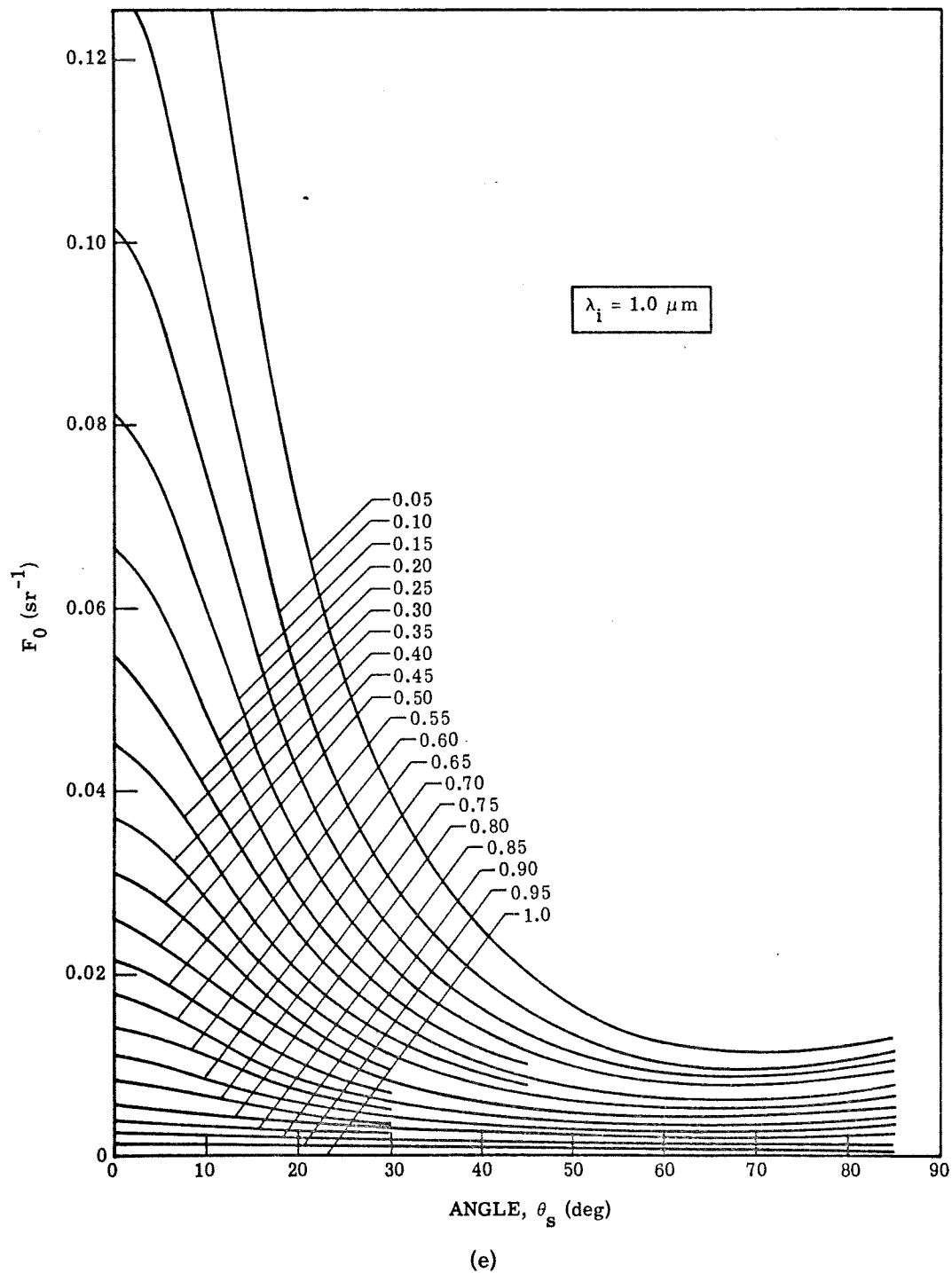
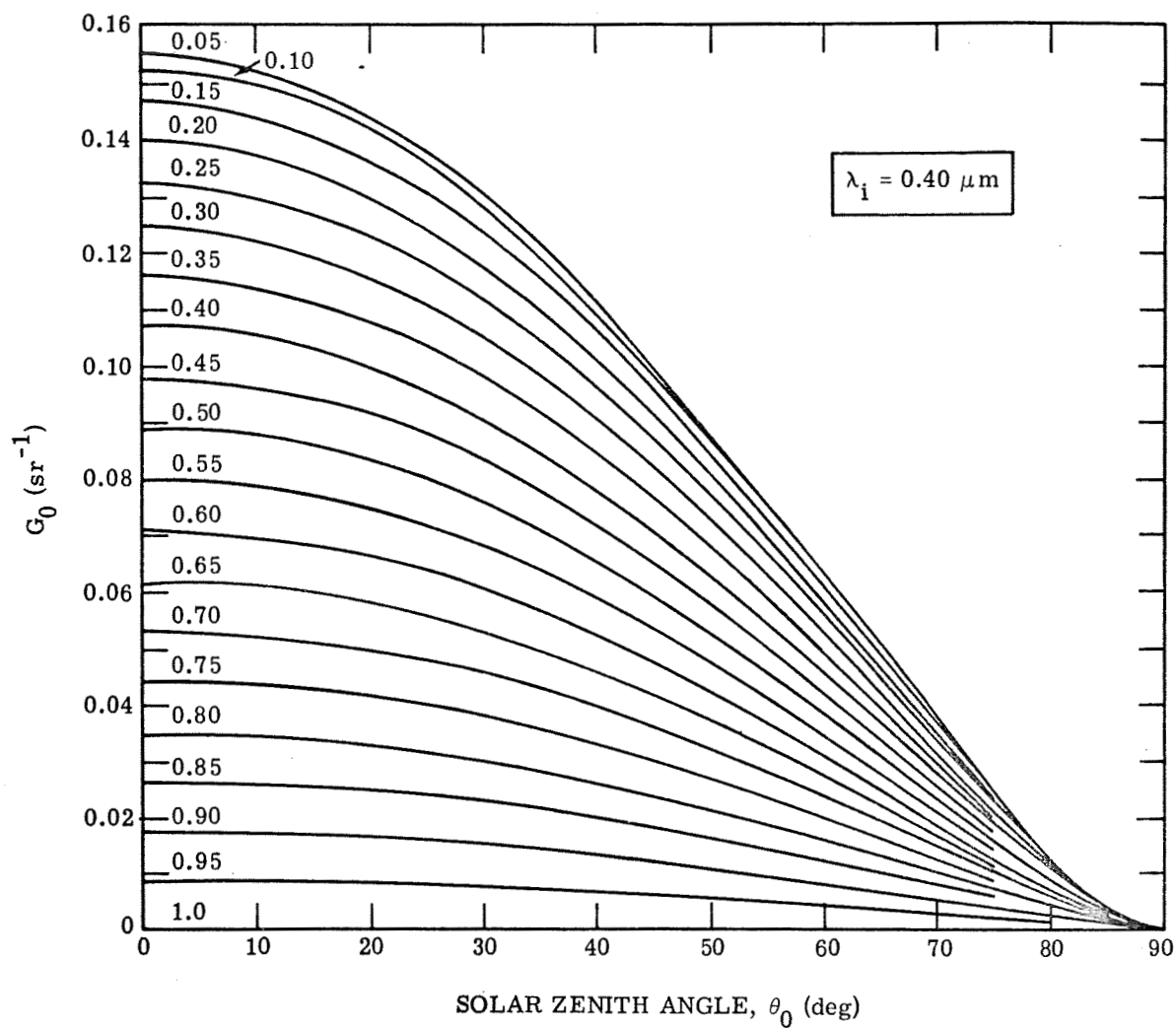
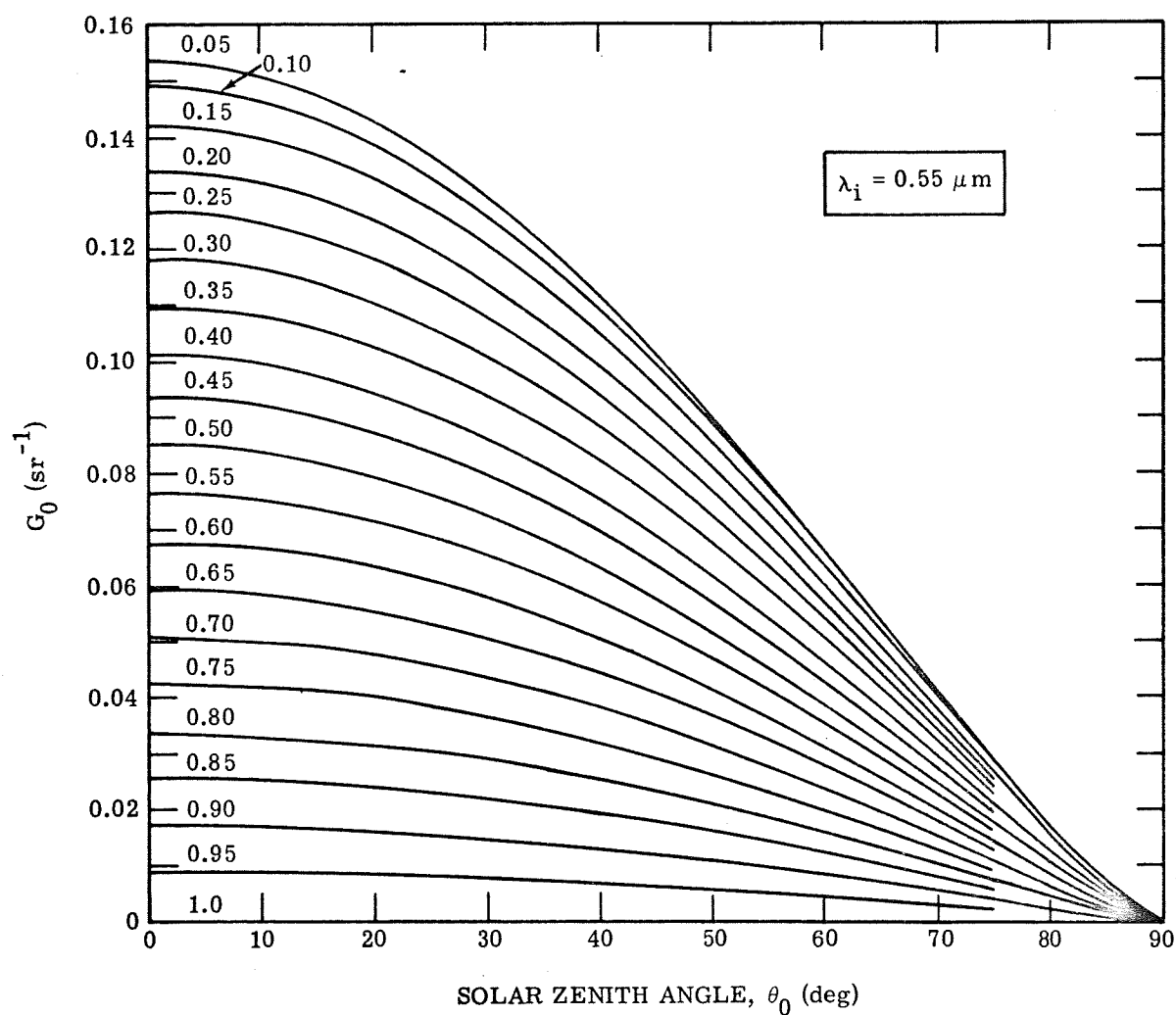


FIGURE 10. RADIANCE FUNCTION F_0 VERSUS DERIVED ANGLE θ_s . Parameter is atmospheric transmittance T_0 (Concluded).



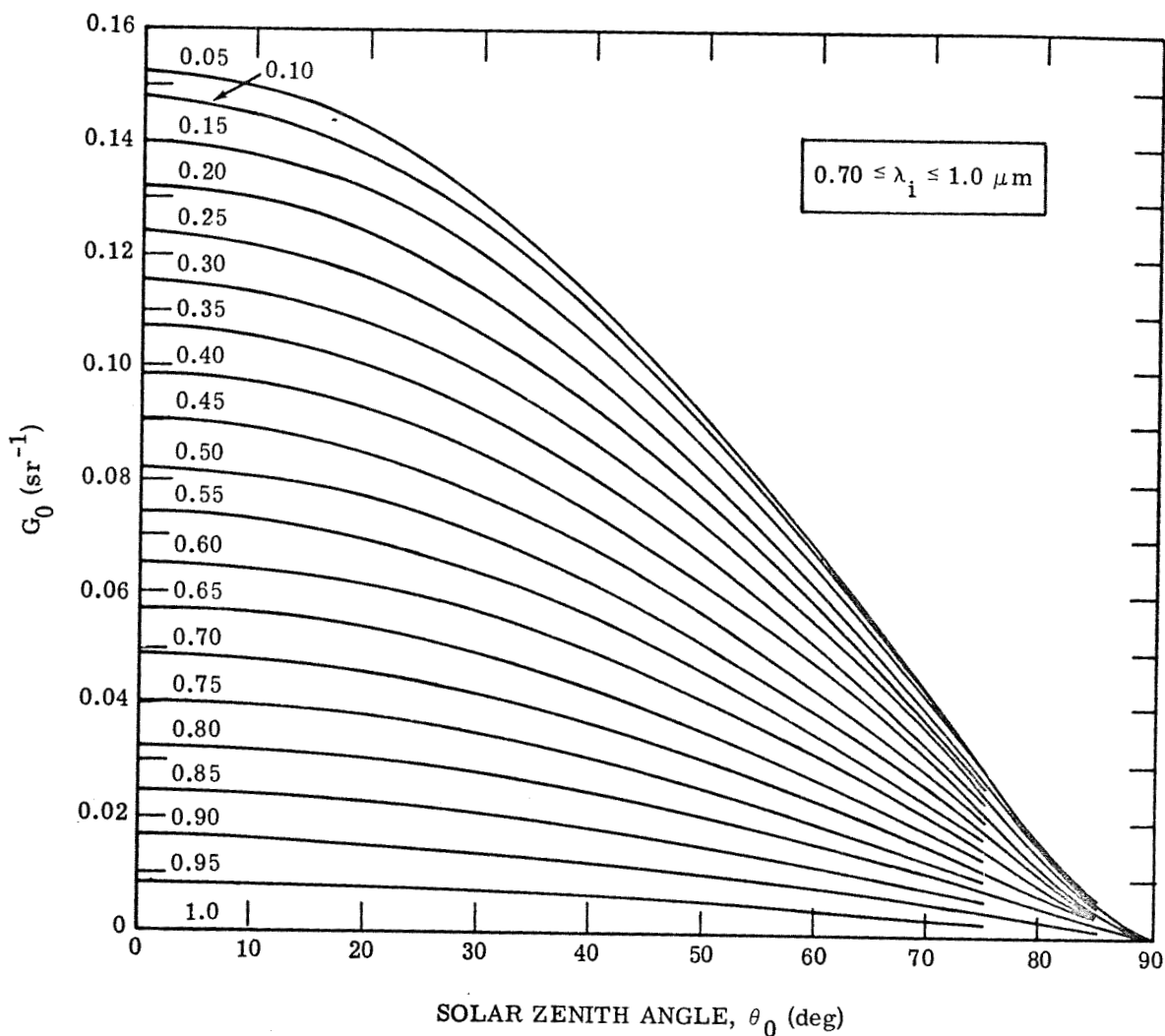
(a)

FIGURE 11. RADIANCE FUNCTION G_0 VERSUS SOLAR ZENITH ANGLE θ_0 . Parameter is atmospheric transmittance T_0 .



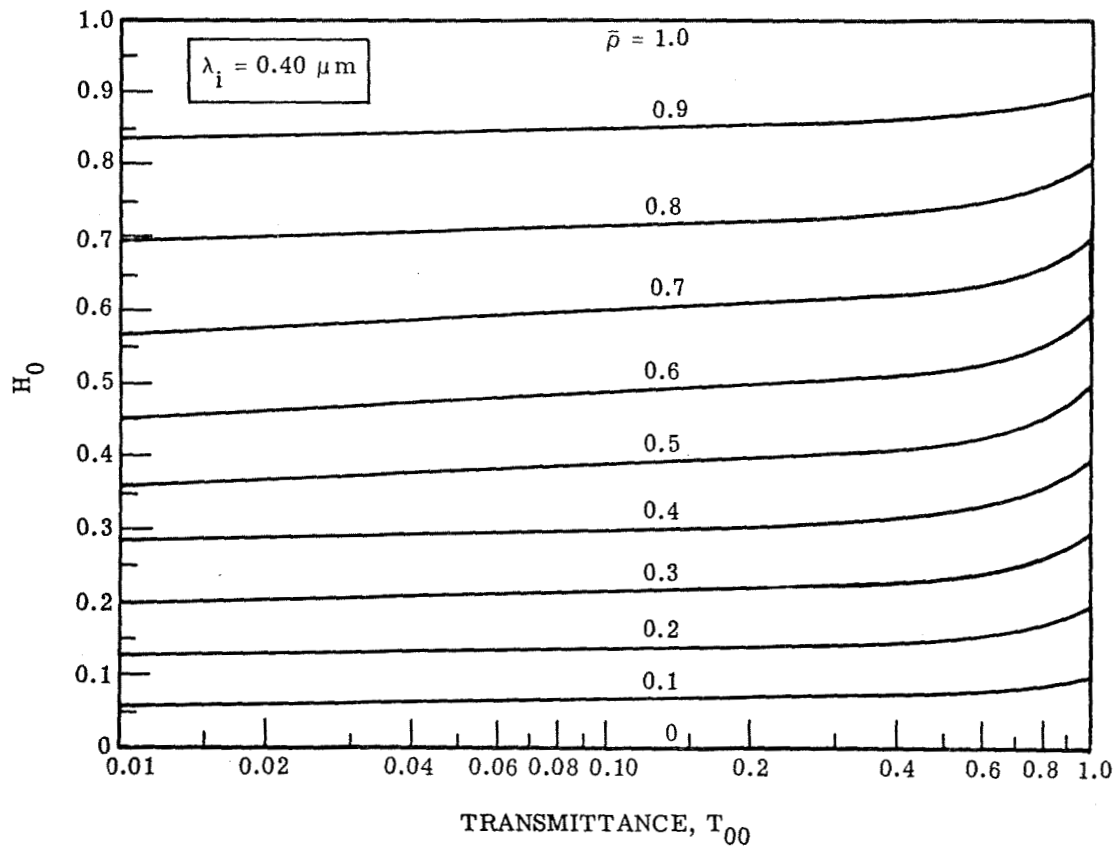
(b)

FIGURE 11. RADIANCE FUNCTION G_0 VERSUS SOLAR ZENITH ANGLE θ_0 . Parameter is atmospheric transmittance T_0 (Continued).



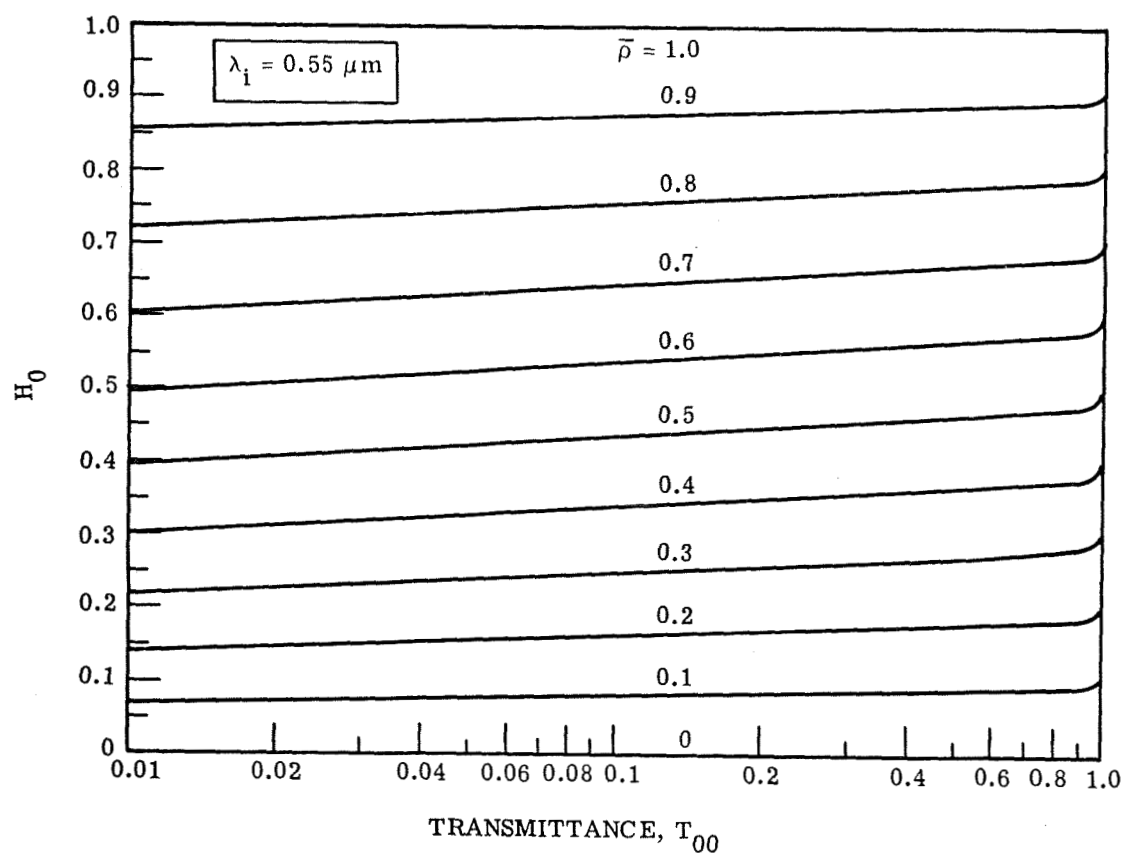
(c)

FIGURE 11. RADIANCE FUNCTION G_0 VERSUS SOLAR ZENITH ANGLE θ_0 . Parameter is atmospheric transmittance T_0 (Concluded).



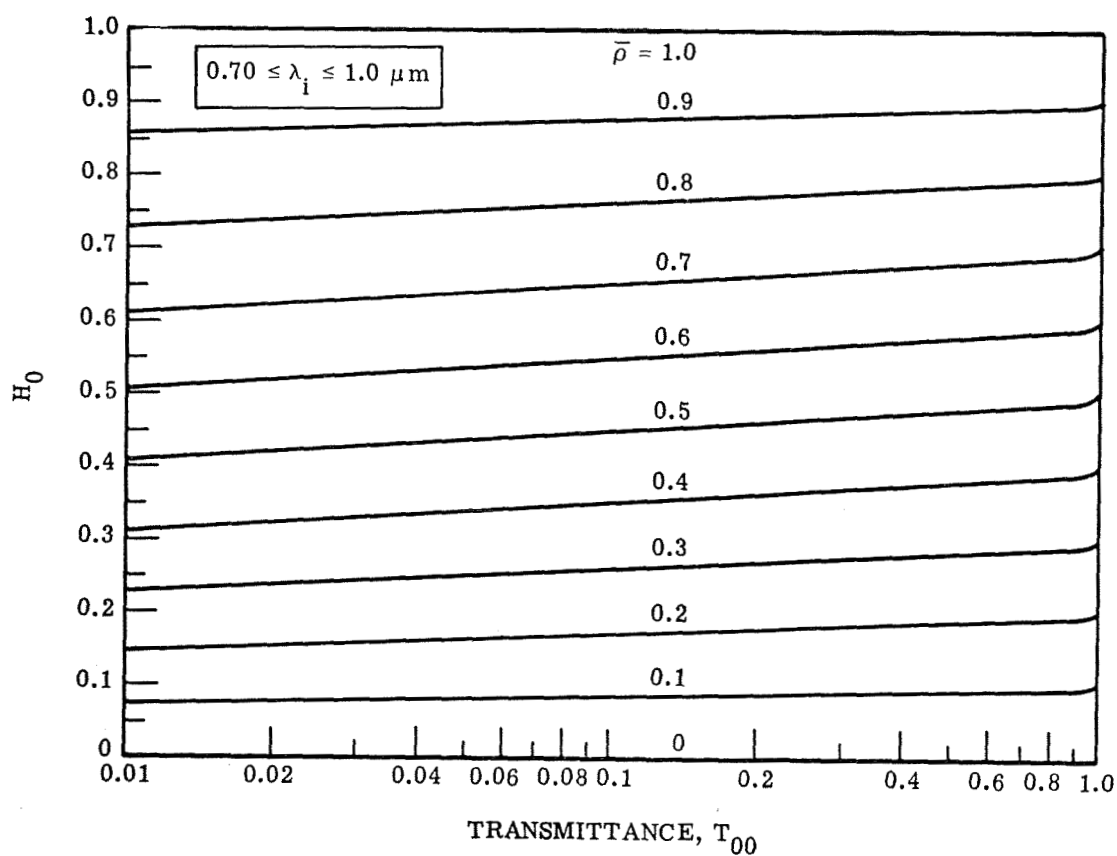
(a)

FIGURE 12. RADIANCE FUNCTION H_0 VERSUS TRANSMITTANCE T_{00} . Parameter is average background terrain albedo $\bar{\rho}$.



(b)

FIGURE 12. RADIANCE FUNCTION H_0 VERSUS TRANSMITTANCE T_{00} . Parameter is average background terrain albedo $\bar{\rho}$ (Continued).



(c)

FIGURE 12. RADIANCE FUNCTION H_0 VERSUS TRANSMITTANCE T_{00} . Parameter is average background terrain albedo $\bar{\rho}$ (Concluded).

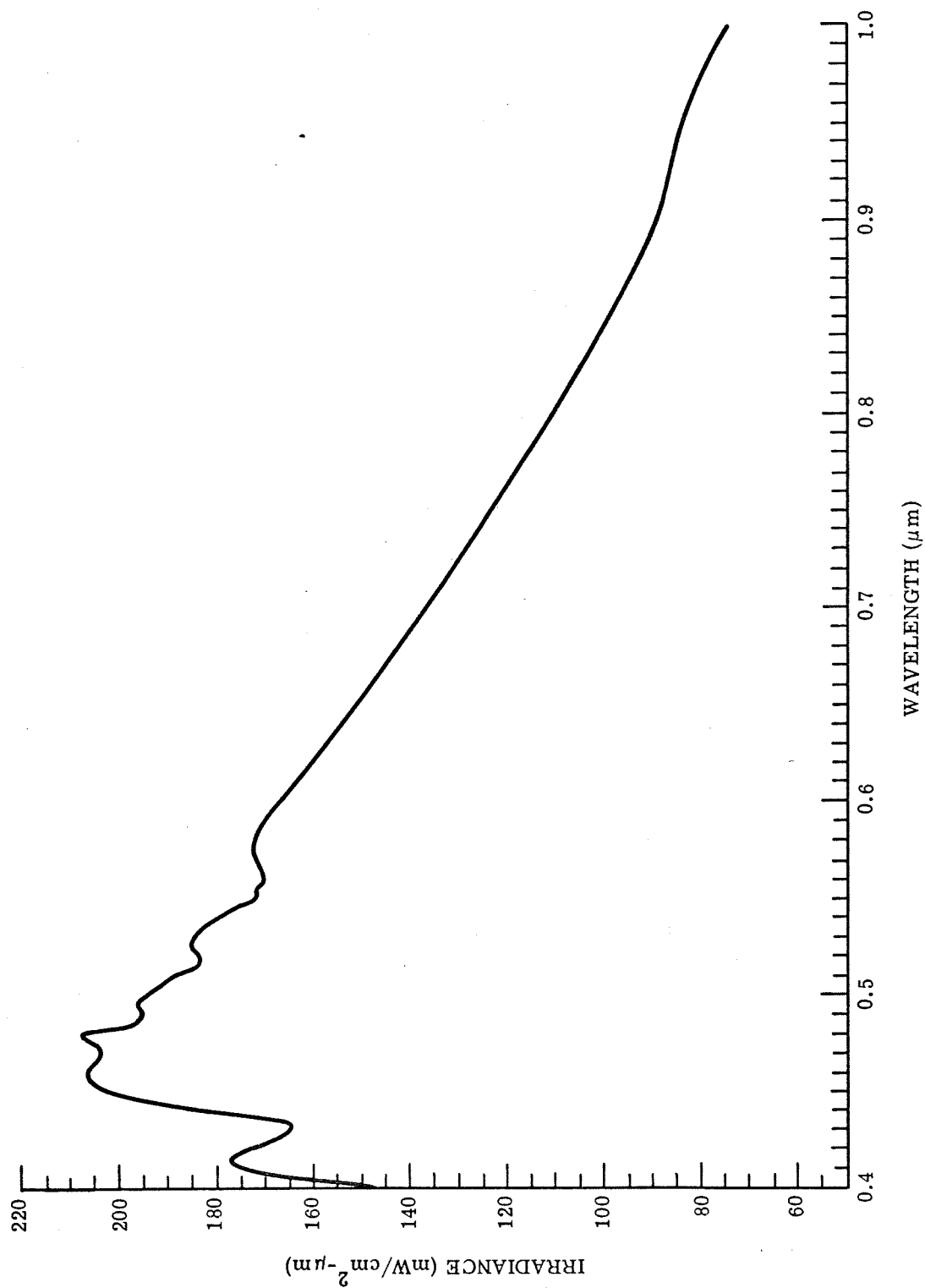
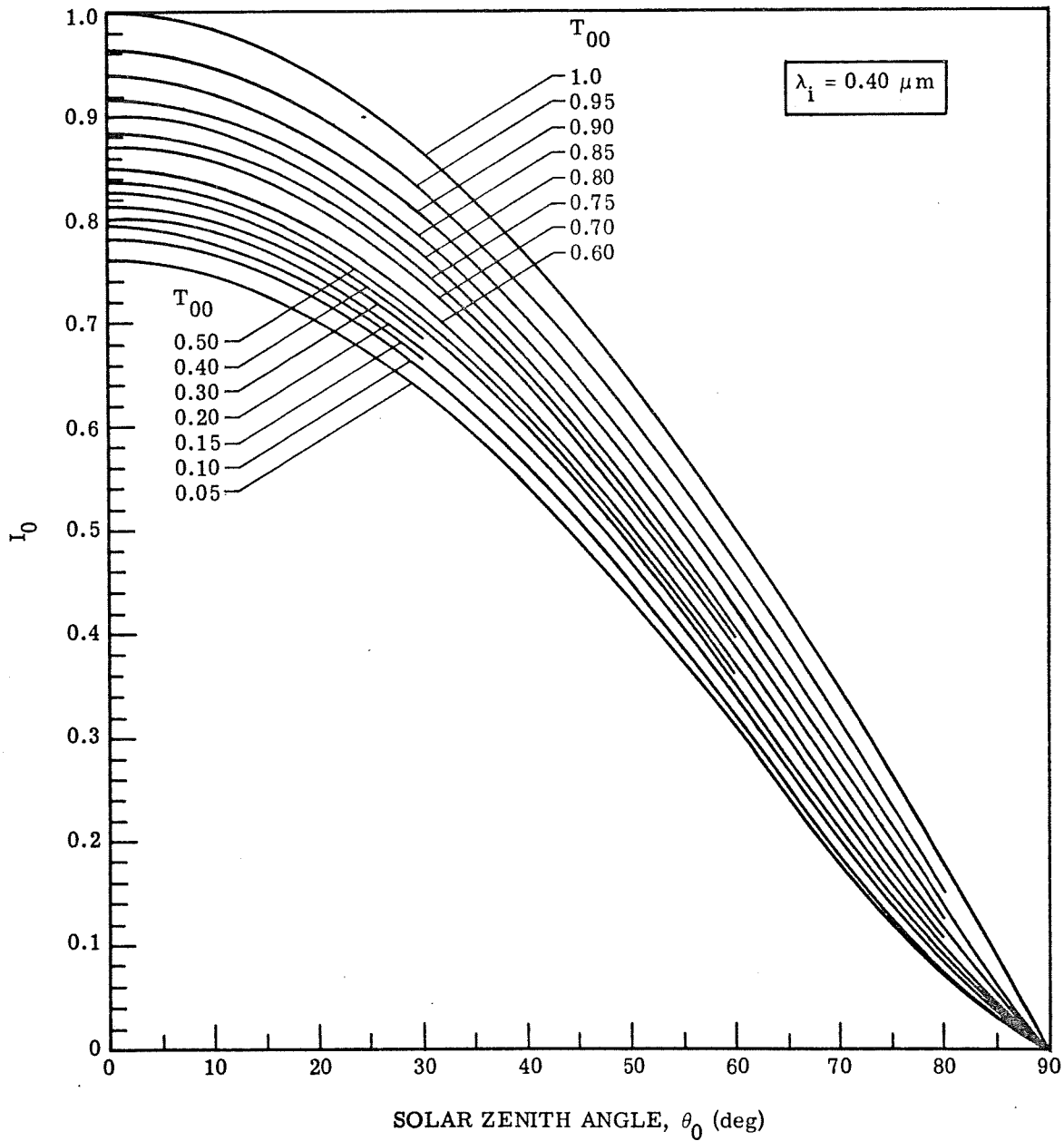
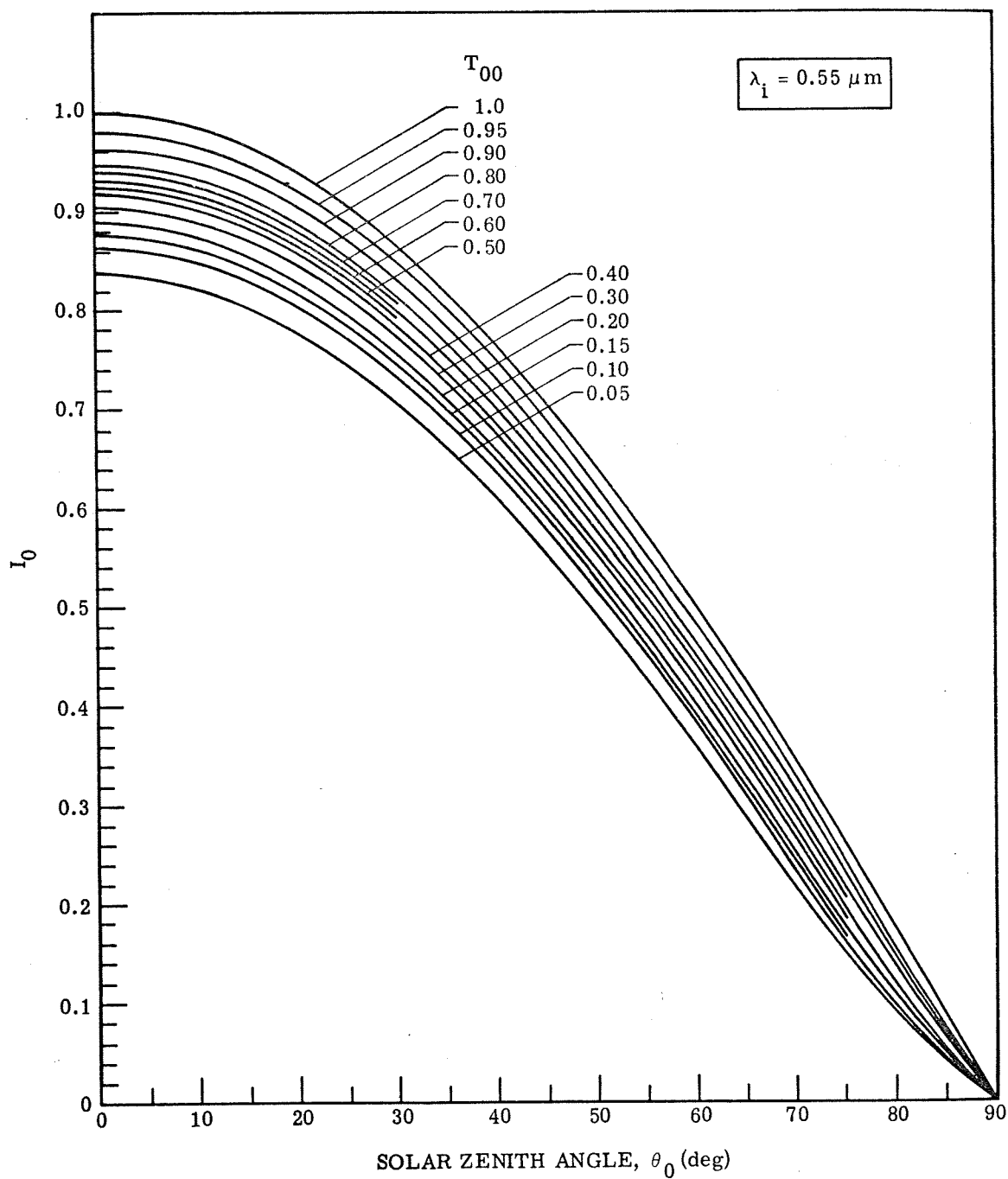


FIGURE 13. EXTRATERRESTRIAL SOLAR SPECTRAL IRRADIANCE E_0 [15]



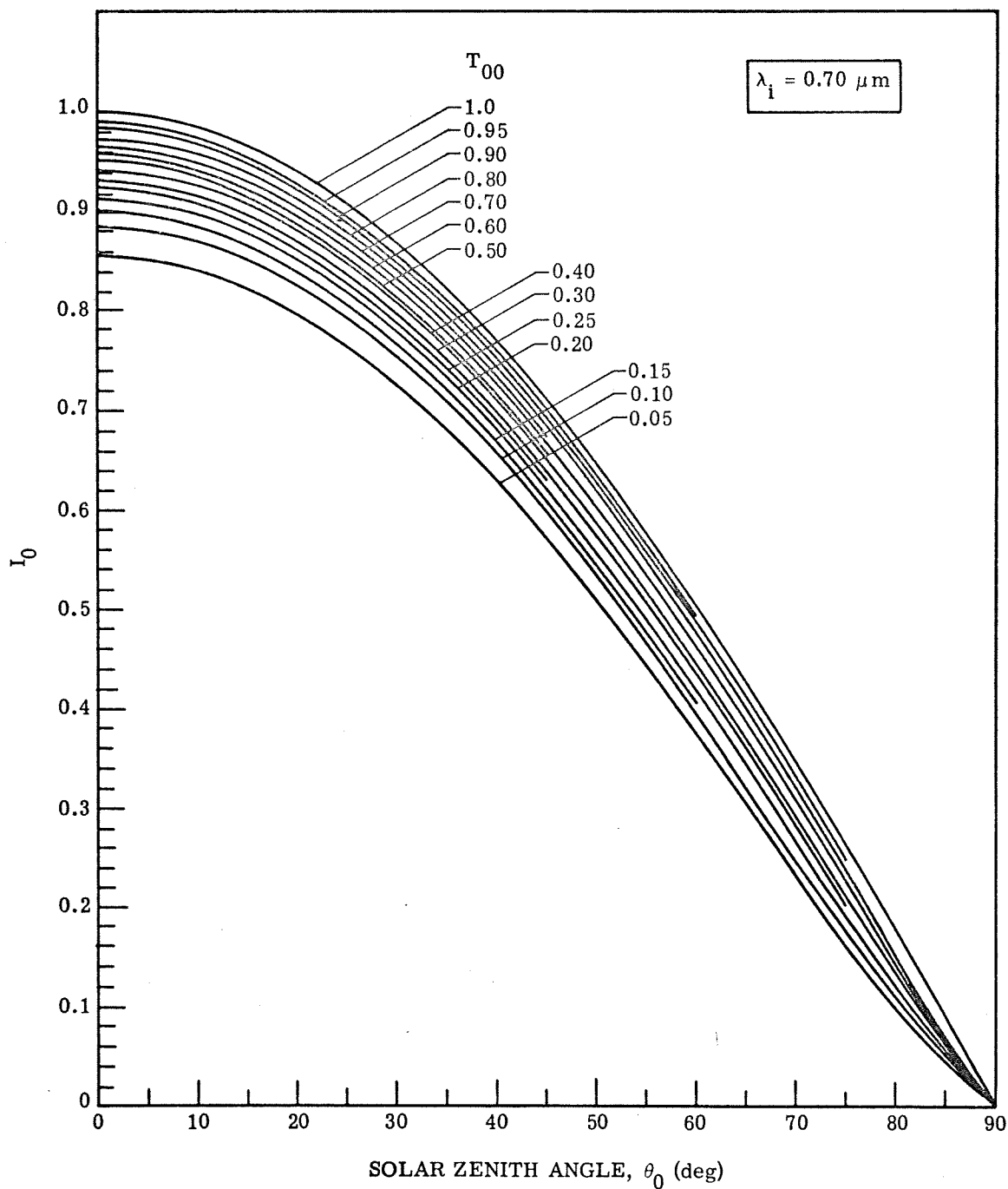
(a)

FIGURE 14. IRRADIANCE FUNCTION I_0 VERSUS SOLAR ZENITH ANGLE θ_0 .
Parameter is atmospheric transmittance T_{00} .



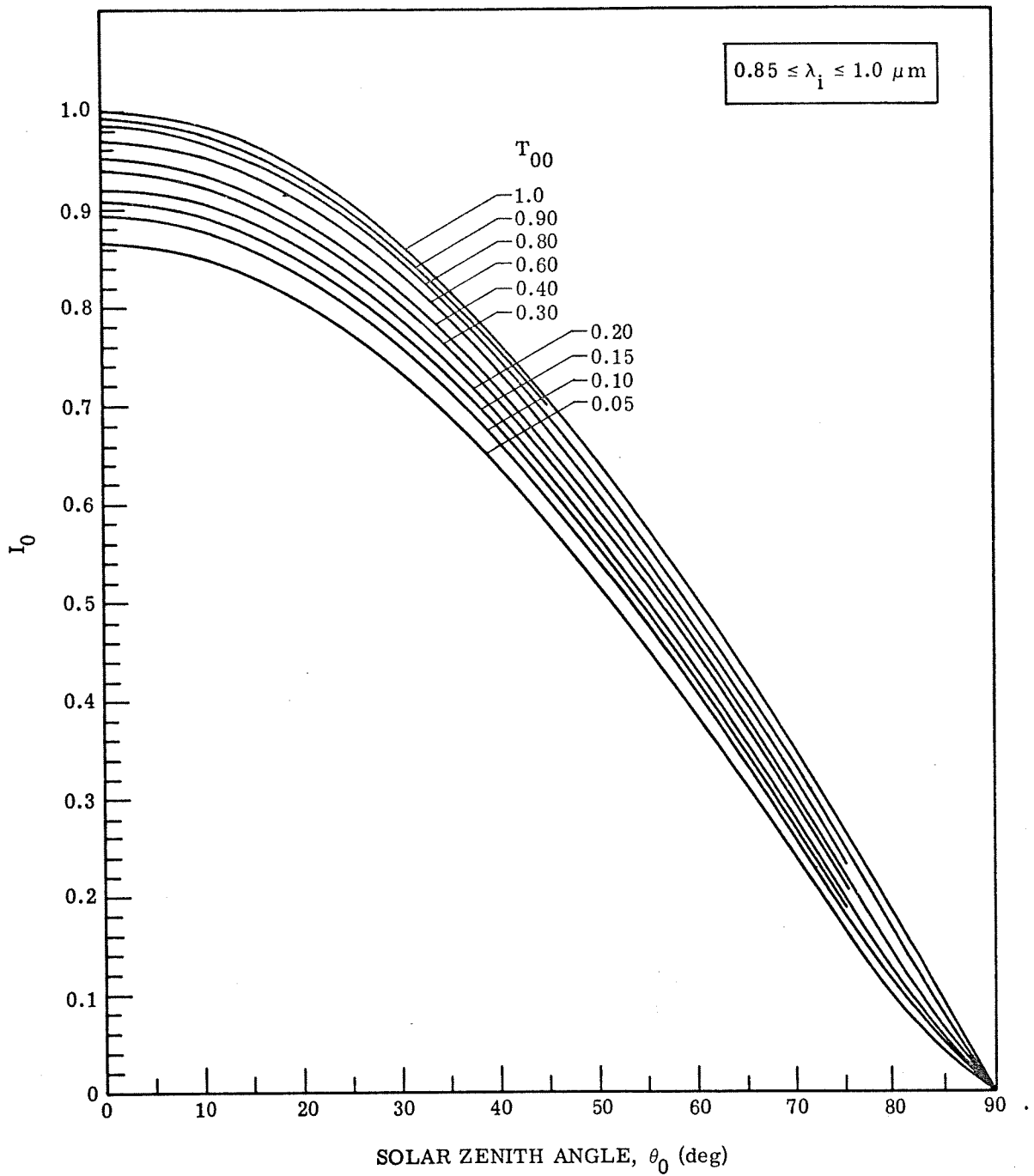
(b)

FIGURE 14. IRRADIANCE FUNCTION I_0 VERSUS SOLAR ZENITH ANGLE θ_0 .
Parameter is atmospheric transmittance T_{00} (Continued).



(c)

FIGURE 14. IRRADIANCE FUNCTION I_0 VERSUS SOLAR ZENITH ANGLE θ_0 .
Parameter is atmospheric transmittance T_{00} (Continued).



(d)

FIGURE 14. IRRADIANCE FUNCTION I_0 VERSUS SOLAR ZENITH ANGLE θ_0 .
Parameter is atmospheric transmittance T_{00} (Concluded).

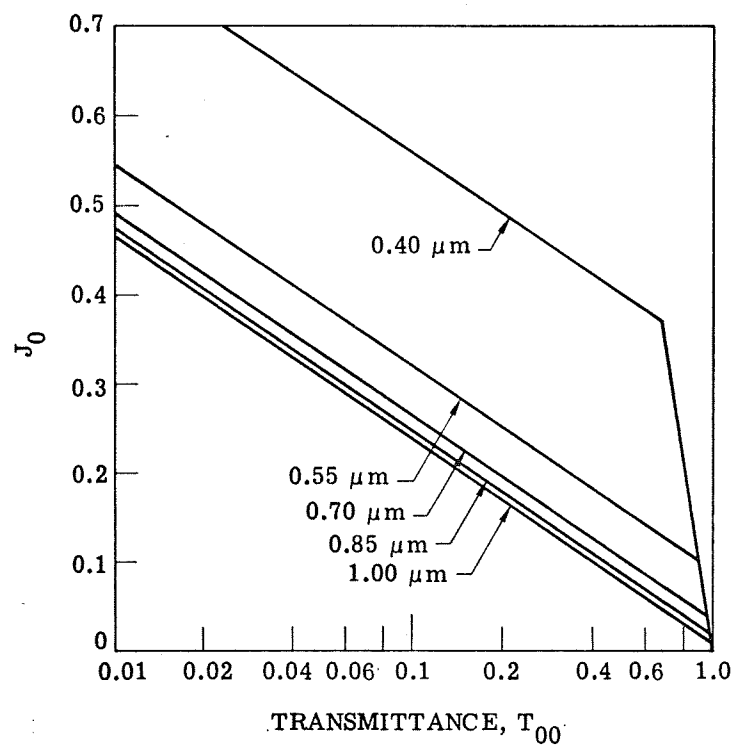


FIGURE 15. IRRADIANCE FUNCTION J_0 VERSUS TRANSMITTANCE T_{00} . Parameter is spectral wavelength.

RADIATIVE TRANSFER MODEL VALIDATION

The purpose of this section is to describe and discuss the procedure used to validate the radiative-transfer model. This mathematical model was developed for calculating the atmospheric effects on received signals. The only aspect of the model for which validation is attempted here is that condition for which the signals are received by sensing devices viewing a ground scene. The model calculates three necessary quantities for this situation: (1) the downwelling irradiance at the ground; (2) the atmospheric transmittance from the ground to the measuring device; and (3) the path radiance.

Using these three quantities in conjunction with the total radiance for a target material as obtained from a calibrated sensing device, the equivalent diffuse reflectance of that target material can be determined. The received signals which are used in the validation procedure are those obtained from Willow Run Laboratories' calibrated multispectral optical-mechanical scanner. The data from this multispectral system allow validation to be independently accomplished at several different wavelengths throughout the visible and near-infrared region of the spectrum.

The following subsections are devoted to description of the model validation. Section 4.1 describes the multispectral scanner data and associated information available for the validation analysis. Section 4.2 describes the specific validation analyses used and discusses and assesses the validation results.

4.1. DATA BASE FOR VALIDATION ANALYSIS

4.1.1. MULTISPECTRAL SCANNER DATA ACQUISITION

The Willow Run Laboratories' multispectral scanner system [4] includes a 12-channel spectrometer. Table 2 gives the spectral response limits for each spectrometer channel. The multispectral scanner data are collected in all 12 spectrometer bands simultaneously registered by means of the entrance slit of a prism monochromator used as the field stop. The data are recorded as analog voltages on magnetic tape. This guarantees that a target element in the ground scene is time related in all 12 recorded spectrometer channels.

The multispectral scanner data are capable of calibration; the recorded analog voltages can be converted to a measure of the apparent radiance at the entrance aperture of the scanner. The calibration system consists of a standard lamp and filter which are viewed through the entire optical system by each spectrometer channel once during each scan line. The apparent radiance of the lamp-filter combination is calibrated as a function of wavelength and lamp current. The analog video voltage obtained for the lamp on each scan line relates voltage to radiance for calibrating the scene voltages.

At the time of the Apollo IX overflight of 12 March 1969, Willow Run Laboratories' multispectral scanner system was collecting data in and around the Imperial Valley. Of the 10 flight

TABLE 2. SPECTRAL RESPONSE LIMITS OF THE 12-CHANNEL SPECTROMETER

Spectrometer Channel	50% Peak Power Bandpass (μm)	10% Peak Power Bandpass (μm)	Peak Response Point (μm)
1	0.412 to 0.427	0.398 to 0.431	0.422
2 (not used)	0.427 to 0.451	0.423 to 0.456	0.440
3	0.451 to 0.465	0.446 to 0.475	0.457
4 (not used)	0.465 to 0.481	0.458 to 0.487	0.473
5	0.481 to 0.501	0.478 to 0.508	0.491
6	0.501 to 0.521	0.492 to 0.536	0.511
7	0.521 to 0.548	0.514 to 0.558	0.533
8	0.548 to 0.579	0.538 to 0.593	0.563
9	0.579 to 0.623	0.566 to 0.638	0.602
10	0.623 to 0.674	0.604 to 0.700	0.646
11	0.674 to 0.744	0.656 to 0.775	0.708
12	0.744 to 0.852	0.725 to 0.920	0.800

lines flown, a pair were flown at two altitudes over the same west to east line at the southern part of the Imperial Valley. This flight line was approximately 12 mi in length, allowing about 6 min of data collection for each pass. The first pass was flown at an altitude of 10,000 ft and the second at an altitude of 5000 ft, with an 18-min time interval between the start of the first pass and the start of the second. The first pass started at 1006 PST. For the time period during which the scanner data were collected, a 32-km visual range was reported, and the sky was cloudless.

The scanner data were collected in 10 of the 12 possible spectrometer bands from 0.4 to 0.8 μm . The two missing spectrometer bands are spectrometer channels 2 and 4 (see Table 2). The multispectral data at both altitudes are of high quality and the signal-to-noise ratio and the resolution of the ground appear good. There is a strong variation in the total radiance with scan angle. In the shorter wavelength bands, this variation is the result of the path radiance, the atmospheric transmittance and the bidirectional reflectance properties of the vegetated and non-vegetated terrain. In the longer wavelength bands, this scan angle variation is primarily caused by the bidirectional reflectance properties of the materials.

A number of targets viewed both at 5000 and 10,000 ft have been chosen for comparison in order to validate the model. With the constant total angular field of view for the scanner system, the ground coverage is directly proportional to the altitude. Any particular target in the ground scene which has been viewed by the scanner system from both altitudes provides a means of comparison if the reflectance for the target is the same for both conditions. Reflectance differences are eliminated by choosing for comparison only targets in which: (1) the ground area of the target (and thus its composition) are the same; and (2) the viewing angle (and thus angular reflectance character) are the same.

Ground truth information was obtained for the center region of the flight data [5]. This region extends 7 mi in the flight line direction and 3.2 mi in the north-south direction and contained at the time, 251 fields. The following information was determined for each of the fields: (1) crop type; (2) row direction; (3) average crop height; (4) average ground cover; and (5) comments which dealt with crop condition and field treatment. (A detailed description of this area is contained in Appendix III.) -The ground truth information is useful to this study for the following reasons:

- (1) The average background terrain spectral albedo is a parameter which is needed by the radiative transfer model. The background albedo affects both the irradiance on the ground and the path radiance. This albedo, which is the average hemispherical spectral reflectance of the whole terrain, can be estimated from the ground truth information. The details of estimating the albedo are discussed in Section 4.1.3.5.
- (2) The equivalent diffuse spectral reflectance of a target material is obtained during the validation procedure. The resulting spectrum can be qualitatively compared to the expected spectrum of the material in order to provide an overall assessment of the scanner spectral calibration and model accuracy.
- (3) The ground truth information is used to correct the multispectral data for variable scan angle effects resulting from target goniometry. Although the scan angle correction is not needed for the validation phase of the study, it is needed for the space simulations to be discussed in Sections 5 and 6.

4.1.2. COMPUTER PROCESSING OF MULTISPECTRAL DATA

All the computer processing on the multispectral data was performed on a Control Data 1604 computer. Preparation of the magnetic tapes in digital format by the A/D equipment was accomplished in the following manner:

- (1) The resolution of the digital data in the scan line direction was determined by the sampling rate used in digitizing the data and was equivalent to 5 mrad.
- (2) Each scan line was roll-corrected for the roll angle of the aircraft. This correction was accomplished by sampling the video data during a time interval set by two gating pulses which are timed with respect to the roll-synchronized pulse.
- (3) The magnitude of the time interval which occurred between the nonroll pulse and the roll-synchronized pulse was recorded and digitized for each scan line of data. This information was necessary so that for each scan line the point number which was equivalent to the nadir look angle could be determined. This information was also used in a digital program to correct the data calibration for the vignetting effect of the scanner aperture existing in 1969.

WILLOW RUN LABORATORIES

The initial processing on the 1604 computer was as follows:

- (1) The digital data were repacked to required software processing format.
- (2) The digital data were made positive and relative by subtracting the voltage equivalent to the dark level (zero radiance) reference of the interior of the scanner.
- (3) The correct number of scan lines for both the 5000- and 10,000-ft data were averaged so that the resolution was equivalent to 5-mrad square for each data point. This averaging was necessary to create square resolution elements since the scanner speed is not variable (i.e., scan lines overlap on the ground for flight altitudes in excess of 1000 ft), and the actual resolution orthogonal to the scan direction is approximately 3 mrad.
- (4) The average voltage level for the calibration lamp in each spectral channel was determined and the scale factor to convert scene voltages to total radiance was calculated.
- (5) The aperture vignetting correction was applied to each scan line of data. This vignetting correction is different for each spectral channel and is a function of the look angle relative to the scanner housing. The time interval between the nonroll and roll pulses recorded with each scan line of data was used to determine this angle for each data point so that the correction could be applied to the previously roll-corrected data.
- (6) The data point which corresponded to the true nadir direction was determined for both the 5000 and 10,000 data. This was possible since the digital program which performed the aperture correction also determined the point number for each scan line which was at the center of the aperture, or, equivalently, the position of the look angle of zero degrees relative to the scanner system. The point number with the highest frequency of occurrence for all the scan lines during the total flight was assumed to be the point number corresponding to the true nadir for the roll-corrected flight data. The maximum and minimum deviation from the chosen nadir point number indicated that the aircraft roll angle range was $\pm 2.4^{\circ}$ for the 5000 data and $\pm 1.0^{\circ}$ for the 10,000 data.
- (7) A pictorial printout of a spectrometer channel, referred to as a graymap, consisting of a printed character representing each digitized data point was made for both the 5000 and 10,000 data. If a data point with a low radiance is represented by a dense printed character and another data point with a high radiance is represented by a less dense printed character, then the appearance of the graymap is similar to a half tone positive print of the scanner imagery. When a graymap is made, the total range of radiances present is divided into a set of intervals with data points within each radiance interval being assigned to one of the symbols from the set of printed characters.

4.1.3. PARAMETERS FOR VALIDATION MODELING

The eight parameters needed by the model are wavelength, azimuth and zenith angles of the sun, azimuth and nadir view angles of the sensing device, height of the sensing device above the terrain, visual range at the ground, and average background terrain albedo.

Wavelength. The spectral bandwidth for each spectrometer channel of the multispectral scanner system is relatively narrow. Each spectrometer channel was represented by a single wavelength. Therefore, model calculations were made only at those discrete wavelengths corresponding to the peak response point on the response curve of each spectrometer channel used. These peak response points are shown in Table 2. For most of the spectrometer channels used, the response curve is approximately triangular and symmetric with respect to the peak, so that the wavelength of the area-weighted centroid of the response curve corresponds to the wavelength of the peak response. For spectrometer channels 1, 11 and 12, the centroid wavelengths differ from the wavelengths of peak response. For spectrometer channel 1, the centroid is at a wavelength slightly shorter than that of the peak while for spectrometer channels 11 and 12, the centroid is at a wavelength slightly longer than that of the peak.

Solar Azimuth and Zenith Angles. The date and local time of the flight along with the longitude and latitude of the ground scene are used in a separate computer program to obtain solar azimuth and zenith angles.

Azimuth and Nadir View Angles of the Sensing Device. The spectrometer system scans the ground scene in a plane which is perpendicular to the centerline of the aircraft. The scanner imagery is roll-corrected. Yaw and pitch are not monitored, so that corrections for these variations are not applied. These effects are thought to be minimal, however. The attitude of the aircraft during the flight must still be accounted for in order to determine the orientation of the scan line. The crab angle and drift angle for the flight can be deduced from the spectrometer imagery if there are roads within the ground scene which can provide a coordinate system. Since the flight line over the Imperial Valley was approximately a west to east flight line, a true north-south road could be used to deduce the crab angle, while a true east-west road could be used to determine the drift angle when the nadir of the aircraft is known for each scan line. The crab and drift angles were determined using the Imperial Valley road system. These angles, together with the nadir definition provided during roll-correction, allowed absolute determination of both the azimuth and nadir view angle for each point of interest in the imagery.

Visual Range. The ESSA weather station at El Centro within the Imperial Valley reported a visual range of 32.2 km (20 mi) on the ground at the time of the flight.

Background Terrain Spectral Albedo. The background terrain spectral albedo was obtained by averaging the area-weighted sum of the directional reflectance for each of the known types of ground cover in the scene for each wavelength of interest. The weights for each type of ground

WILLOW RUN LABORATORIES

cover were determined from the imagery by measuring the size of all fields within the ground truth area.

The directional reflectances were obtained from field reflectance measurements available from the Earth Resources Spectral Information System (ERSIS). The reflectance curves for alfalfa, barley, rye, sugar beets, bare soil, salt flat, and cement road were used. For the remaining types of vegetative ground cover which constituted a small percentage of the total area, the weighting factors were summed and an average reflectance curve for green vegetation was used.

Height. The height of the aircraft above the terrain was determined from flight information.

Station Pressure. The ESSA weather station at El Centro within the Imperial Valley was the source of atmospheric pressure information for the flight period. The reported pressure was not significantly different from standard sea level pressure (1013 mb).

4.1.4. TARGET SELECTION

Several targets viewed from the same angle at 5000 and 10,000 ft were used to validate the model. Each such target constituted a ground area surrounding those specific resolution elements which were viewed at precisely the same angle. In order to locate these targets, the line representing the nadir for the two flight data sets must be established with respect to the terrain. During the computer processing of the digitized multispectral data, the point number which corresponded to the nadir view angle was determined for both the 5000 and 10,000 flight data. The use of the point number associated with its own flight data allows the nadir ground track to be traced on a graymap obtained from one of the spectrometer channels for that flight so that an association between terrain features and the nadir ground track can be made. This was done on a graymap for both the 5000 and 10,000 data. The two nadir ground tracks were separated at the start of the ground truth area and merged at the end. By first determining the physical separation between the two tracks at various positions along the flight line, the locus of targets seen at a common view angle at each of these positions was obtained. The common view angle varied from 14° to 0° along the flight path within the ground truth area.

A line representing the common view angle was drawn on each of the graymaps. Eighteen target areas were chosen along this line. Each target area was within boundaries surrounding one crop type; the dimension in the flight path direction was restricted by field boundaries in most cases. In the scan angle direction, approximately 5 resolution elements were used on either side of the common view angle resolution element in the 10,000 flight data. This corresponded to a $\pm 1.5^{\circ}$ deviation from the common view angle. In the 5000 data, the angular deviation from the common view angle necessarily varied by approximately twice as much in order to ensure that the width of the 5000 ground area was of the same physical dimension as was used for the 10,000 ground area.

This procedure was used for all eighteen target areas and established the location of the target areas with respect to positional coordinates on a graymap. The positional coordinates are the point numbers corresponding to each sampled point digitized in the scan line and the line numbers corresponding to each digitized scan line. All the data points which lie within an area specified by these positional coordinates were used to compute the spectral statistical signature which consists of a spectral radiance mean value and variance in each spectral channel and spectral covariance between channels.

4.2. VALIDATION ANALYSIS

The atmosphere plays a triple role in affecting the received radiation at a sensing device, by: (1) modifying the irradiance at the top of the atmosphere to produce that which exists at the ground; (2) attenuating the signal received from the target material on the ground; and (3) scattering extraneous radiation (path radiance) into the sensor's field of view. The radiative-transfer model can calculate these three atmospheric effects. The relationship between these three quantities and the total radiance $L(h)$ of a target as it is observed by a remote sensing device such as a multispectral scanner at altitude h is

$$L(h) = \frac{\rho^t E T(h)}{\pi} + L_p(h) \quad (3)$$

where $L(h)$ = the total radiance of the target as measured by the sensor

ρ^t = the effective diffuse reflectance of the target material

E = the irradiance onto the target

$T(h)$ = the atmospheric transmittance from the target to the sensor

$L_p(h)$ = the path radiance generated between the target and the sensor

Solving for ρ^t , the effective diffuse reflectance of the target material, produces

$$\rho^t = \pi \left[\frac{L(h) - L_p(h)}{ET(h)} \right] \quad (4)$$

This reflectance is a pure target attribute only if the target is in fact reflecting diffusely. If the target is not inherently diffuse (as is usually the case), then ρ^t will generally vary with changes in viewing or illumination geometry for it only describes the target reflectance for one particular geometric condition.

The effective diffuse reflectance of a particular target should be the same when obtained from Eq. (4) with the use of data from two different altitudes, as long as the corresponding illumination geometries and viewing geometries are essentially the same, and as long as the calculated atmospheric parameters and sensor calibration are correct. The 18 targets which were obtained from the 5000 and 10,000 data were used for such a comparison. The view angle and

ground area were the same for each target but the illumination conditions were slightly different because of elapsed time between the flights. The zenith angle for the sun corresponding to the mean time for each pass was 43.5° for the 10,000-ft data and 41.0° for the 5000-ft data. The azimuth angles for the sun were 140.8° and 147.1° for the 10,000 and 5000 flight data respectively. However, because of differences in crab angle for the two flights, the relative azimuth angles between the viewing direction and the sun differed by less than 1° .

While Eq. (4) is the only mathematical relation which can be used to test the validation results, it can be looked at in two slightly different ways, each of which emphasizes the effects of different error sources. The first is to calculate independently $\rho^t(h)$ for $h = 5000$ ft and 10,000 ft, and then compare results. This comparison emphasizes the absolute accuracy of the model and the scanner calibration. The second method involves equating $\rho^t(h)$,

$$\rho^t(10,000) = \rho^t(5000)$$

and then evaluating the resulting relation which, when Eq. (4) is used, gives, by rearrangement,

$$L(10) = \frac{E(10)T(10)}{E(5)T(5)} L(5) + \left[L_p(10) - \frac{E(10)T(10)}{E(5)T(5)} L_p(5) \right] \quad (5)$$

Note that the irradiances are not dependent upon altitude directly, but are dependent upon the time at which data for a particular altitude is acquired. Graphic analysis of Eq. (5) allows evaluation of possible errors resulting from uncertainties in the actual values of the environmental parameters used as inputs to the model.

4.2.1. VALIDATION BY ρ^t COMPARISON

The spectral values of effective diffuse reflectance, ρ^t , were calculated for each of the 18 selected targets for each flight altitude using Eq. (4). Two of the quantities, irradiance at the ground and path radiance, calculated by the model were corrected for the effect of ozone absorption before using them in Eq. (4). This correction is discussed in Section 6 and Appendix II.

The equivalent diffuse spectral reflectances calculated for two of the 18 targets are shown in Figs. 16 and 17. Figure 16 shows the results obtained for a barley field with 90% ground cover. The common nadir view angle for this field at the two altitudes was approximately 1° . Figure 17 shows the equivalent diffuse spectral reflectance for a salt flat field where the common nadir view angle was 13° . In both figures, the dotted data points designate the reflectance values calculated from the 5000-ft data, and the symbol, x, denotes those for the 10,000-ft data. The data points have not been connected by lines in order to emphasize that the calculated values apply to mean values within relatively large (by spectroscopy standards) wavelength intervals. The absolute values of ρ^t shown in these figures cannot be used in any definitive way to determine

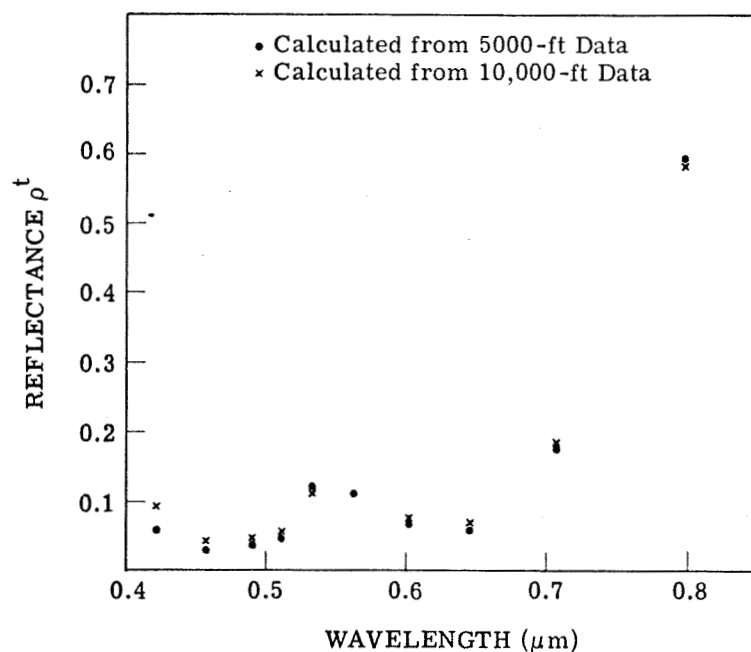


FIGURE 16. EFFECTIVE DIFFUSE SPECTRAL REFLECTANCE FOR A BARLEY FIELD

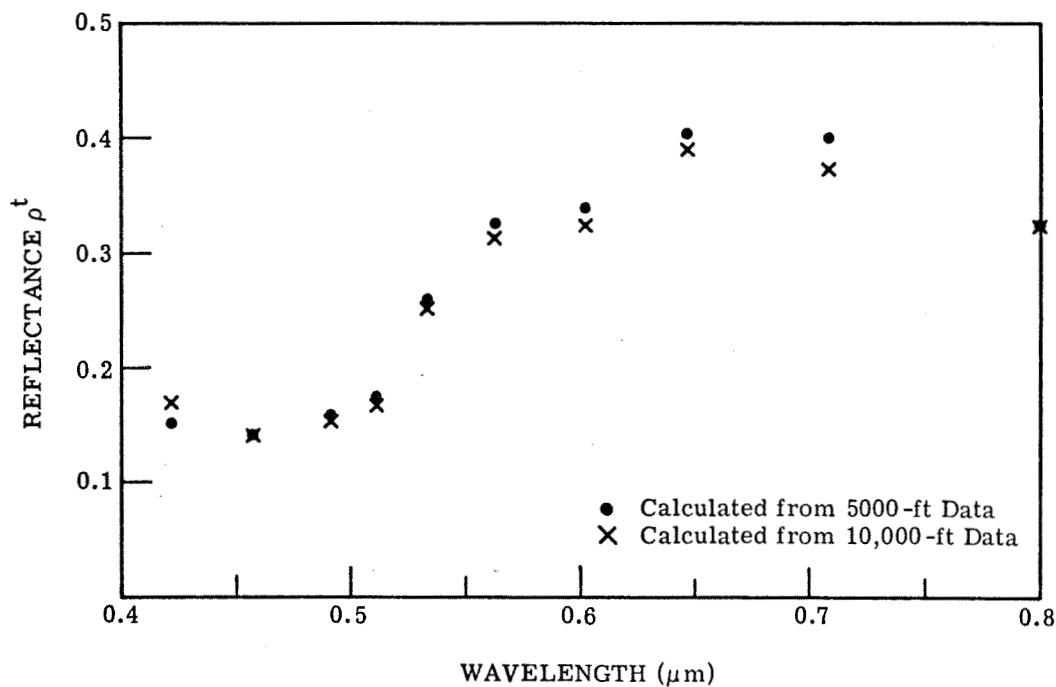


FIGURE 17. EFFECTIVE DIFFUSE SPECTRAL REFLECTANCE FOR A SALT FLAT

the accuracy of the result. The correct values are dependent upon the exact nature of the target and the illumination conditions, so that reflectance spectra obtained elsewhere from laboratory or ground measurements cannot be directly compared. However, the gross spectral variations do appear reasonable for the targets shown.

The absolute difference, $\Delta\rho^t$, between a ρ^t calculated from 10,000-ft data and one calculated from 5000-ft data can be usefully compared, however. Since the analysis was designed and the calculations made based upon the criterion that $\Delta\rho^t$ should be zero, any other systematic result will show the errors associated with the calculations. Table 3 shows, for each spectral channel, the average of the differences, $\overline{\Delta\rho}$, for all 18 targets analyzed. Any significantly positive value of $\overline{\Delta\rho}$ indicates a systematic error of determining $\rho_{10}^t > \rho_5^t$, while a significantly negative value of $\overline{\Delta\rho}$ indicates the opposite systematic error. Only systematic errors are of interest here since random errors are associated only with the noise in the scanner data and with any errors associated with failing to define exactly the same spatial boundaries for a particular target from the two altitudes. The average $\overline{\Delta\rho}$ in Table 3 is positive at all the wavelengths except 0.708 μm (spectrometer channel 11). This indicates that for all wavelengths with the exception of one, the effective diffuse reflectance calculated for the 10,000 data was greater than that for the 5000 data. The largest value of $\overline{\Delta\rho}$ is 0.03 and occurs at 0.422 μm (spectrometer channel 1).

TABLE 3. MEAN VALUE OF THE CALCULATED DIFFERENCES ρ_{10}^t TO ρ_5^t FOR EACH SPECTRAL CHANNEL

Spectrometer Channel	Peak Wavelength (μm)	$\overline{\Delta\rho}$
1	0.422	0.030
3	0.457	0.009
5	0.491	0.005
6	0.511	0.004
7	0.533	0.006
8	0.563	0.005
9	0.602	0.003
10	0.646	0.004
11	0.708	-0.003
12	0.800	0.003

The data of Table 3 indicate the systematic error associated with the radiative transfer model calculations if one assumes that the scanner calibration is excellent, and if one assumes that the inputs to the model were exactly correct. In fact, the absolute radiometric accuracy of the scanner calibration is not known, although it is felt to be least reliable in spectrometer channel 1. Additionally, one must accept the inputs to the model as being of limited, though unknown, accuracy. This is especially true for visual range, which is a human estimate. In any case, comparison of the calculated values ρ^t would seem to provide no basis for discrediting the accuracy of the radiative transfer model.

4.2.2. VALIDATION BY MEANS OF ρ^t EQUIVALENCE

Equation (5) defines the linear relationship which exists between the total radiance for two different altitudes with respect to the calculated and predicted quantities by the model. The slope of the line is the product of two ratios, the ratio of the irradiances at the ground and the ratio of transmittances; the intercept is a linear combination of the path radiances where one of the path radiances is weighted by the value of the slope. The line associated with Eq. (5) will be called the S-I line (slope-intercept) for convenience.

Only a certain portion of the S-I line has a physical meaning with respect to target radiances. This meaningful portion of the S-I line exists between the point on the line where $\rho^t = 0$ [i.e., $L(10) = L_p(10)$ and $L(5) = L_p(5)$] and the point on the line where $\rho^t = 1$ [i.e., $L(10) = [E_{(10)} T_{(10)} / \pi] + L_p(10)$ and $L_T(5) = [E_{(5)} T_{(5)} / \pi] + L_p(5)$]. Only within this portion of the S-I line does the target radiance for the two altitudes relate to a diffuse reflectance for the target.

A linear measure for ρ^t exists along the S-I line between the maximum and minimum values of ρ^t . This can be seen by rearranging Eq. (3) to give

$$L - \frac{\rho^t E T}{\pi} - L_p = 0$$

and then equating this relation for the two altitudes to produce, upon rearrangement,

$$L(10) = L(5) + \left\{ \frac{\rho^t}{\pi} [E(10)T(10) - E(5)T(5)] + L_p(10) - L_p(5) \right\} \quad (6)$$

Equation (6) is the equation of a straight line with unit slope and an intercept equal to the bracketed term. Since the intercept varies linearly with ρ^t , Eq. (6) defines a family of parallel lines, the distance between which is proportional to $\Delta \rho^t$. Thus, these lines must intersect with the S-I line (Eq. 5) at intervals proportional to $\Delta \rho^t$, and therefore distance along the S-I line must be linear in ρ^t .

The S-I line can be generated by the radiative transfer model since all the elements necessary to define both the slope and intercept are calculated by the model. Such a line for hypothetical conditions is shown in Fig. 18, with the ρ^t scale indicated. A hypothetical data point representing a particular target for which the scanner would have measured particular values of $L(10)$ and $L(5)$ for the same conditions is also shown. If the data point were on the S-I line, then the model calculated results would be in agreement with the scanner measurement. In the example the data point is not on the line. If one draws a vertical line through that data point, the intersection with the S-I line will be at that value on the ρ^t scale defined by Eq. (4) for $h = 5000$ ft. Conversely, a horizontal line through the data point will intersect the S-I line at the value on the ρ^t scale defined by Eq. (4) for $h = 10,000$ ft. Thus, it is seen that the S-I line provides a means

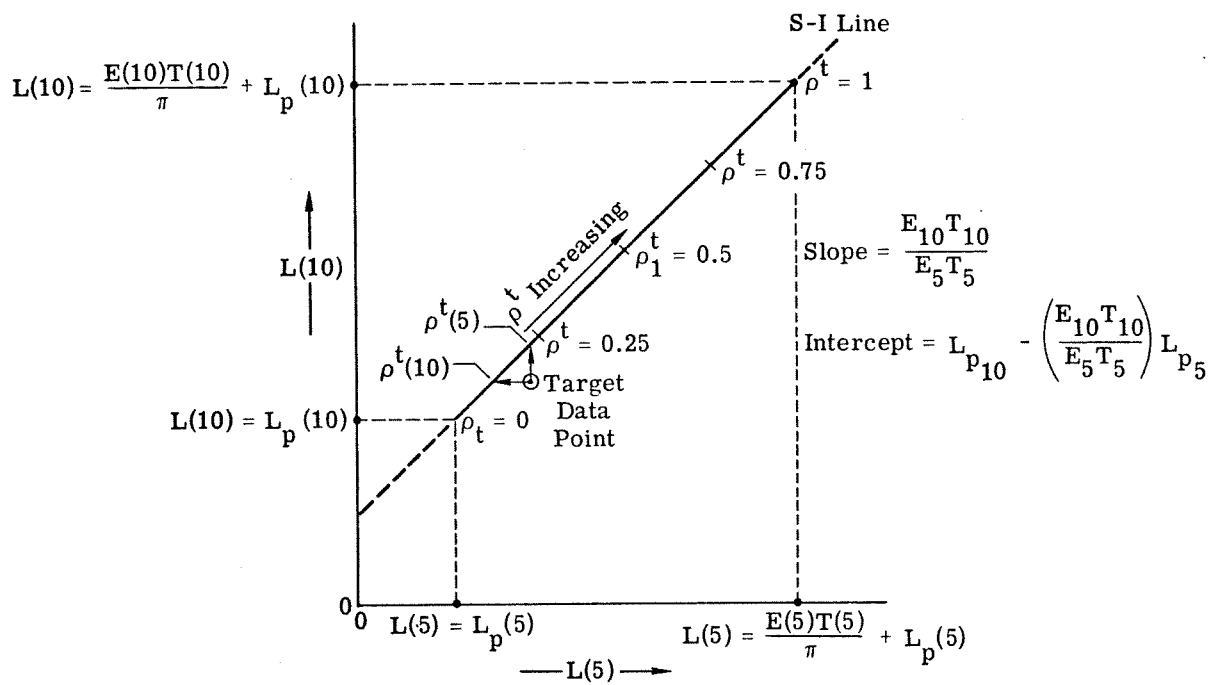


FIGURE 18. HYPOTHETICAL SLOPE-INTERCEPT (S-I) LINE FOR $L(10)$ VERSUS $L(5)$

WILLOW RUN LABORATORIES

for a graphical solution of the calculations of ρ_{10}^t and ρ_5^t discussed in Section 4.2.1. Any data point lying above the line leads to $\rho_{10}^t > \rho_5^t$, while a data point below the line leads to $\rho_{10}^t < \rho_5^t$.

While the location of a plotted data point on the S-I line indicates agreement between model calculation and scanner measurement, it is not necessarily an absolute agreement unless some other information is present to define where on the line the data point should fall, i.e., the true value of ρ^t must be independently known. Since it was not known for any target in this experiment, a limitation in absolute model validation resulted.

The real utility of the S-I line approach to the validation lies in the ability to show those model calculation uncertainties which are due to uncertainties in the values of the input specifications. This can be accomplished by calculating upper and lower bounds of the S-I line resulting from the appropriate combinations of the upper and lower bounds of uncertainty associated with the inputs. Tables 4 and 5 show, for each model input parameter, the nominal value (i.e., the reported value or the best estimate) and the estimated uncertainty in that value for this experiment. Also shown are the relative effects (0, + or -) on both slope and intercept of the S-I line which would be caused by a small increase in the nominal value for each parameter. Note

TABLE 4. RELATIVE EFFECT UPON S-I (SLOPE-INTERCEPT)
LINE CALCULATION CAUSED BY INPUT UNCERTAINTIES

Parameter	Nominal Value	Absolute Uncertainty	General Effect Upon Calculating*	
			Slope	Intercept
Extraterrestrial Solar Irradiance (E_0)	Fig. 13	$\pm 6\%$	0	+
Visual Range (V)	32 km	+8 km -7km	+	-
Average Terrain Background Albedo ($\bar{\rho}$)	See Table 5		0	+
Sensor Height Abover Terrain (h)	10,184 ft 5184 ft	± 500 ft	- for 10,000 ft + for 5000 ft	+ for 10,000 ft - for 5000 ft
Nadir View Angle (θ_v)	7° Average	+7° (0° - 14° target spread)	-	+
Solar Zenith Angle (θ_0)	43.5° for 10,000 ft 41.0 in. for 5000 ft	$\pm 2^\circ$	-	-
Relative Azimuth (ϕ_r)	36.1° for 10,000 ft 36.7° for 5000 ft	$\pm 2^\circ$	0	- for 10,000 ft + for 5000 ft
Effective Channel Wavelength (λ)	See Table 3	$\pm 0.01 \mu\text{m}$ ($\lambda < 0.68 \mu\text{m}$) $\pm 0.02 \mu\text{m}$ ($\lambda > 0.68 \mu\text{m}$)	+	-

*+ means a higher value of parameter leads to a higher value of slope or intercept.
 - means a higher value of parameter leads to a lower value of slope or intercept.
 0 means no effect.

TABLE 5. NOMINAL VALUE AND UNCERTAINTY
FOR AVERAGE BACKGROUND TERRAIN ALBEDO,

Wavelength (μm)	$\bar{\rho}$	Estimated Uncertainty (% of value)
0.422	0.0583	± 50
0.457	0.0677	± 50
0.491	0.0741	± 50
0.511	0.0855	± 50
0.533	0.1059	± 50
0.563	0.1212	± 50
0.602	0.1144	± 50
0.646	0.1140	± 45
0.708	0.1701	± 40
0.800	0.3179	± 30

that for sensor height, h , and relative azimuth, ϕ_r , the nominal values for the two altitudes carry independent effects since independent measures for those parameters were made. For all the other parameters, the uncertainties cannot be applied independently for the two altitudes since, even if the absolute values are wrong, these values are equally applicable to data from both altitudes. This even applies to θ_0 since the time interval between the acquisition of the 10,000-ft and 5000-ft data is accurately known, even though the absolute time of either is uncertain.

The effect upon the S-I line (and, we believe, upon the real atmosphere) due to variation of an input parameter is usually opposite for the slope as compared to the intercept. Thus, in determining an upper bound to the S-I line for the given situation, one must decide whether an upper bound emphasizing slope effects (i.e., transmittance and irradiance) or intercept effects (i.e., path radiance) is to be determined. In general, at longer wavelengths and higher target reflectances, the slope contains the most significant portion of atmospheric effects, while at shorter wavelengths and lower target reflectances, the intercept contains the most significant atmospheric effects. Thus, upper and lower limits to the S-I line for spectrometer channels 1 through 10 were determined by choosing, from Tables 4 and 5, that combination of extreme values of the input parameters which would lead, respectively, to the largest and smallest intercepts. Conversely, the upper and lower limits to the S-I lines for spectrometer channels 11 and 12 were determined by choosing, from Tables 4 and 5, that combination of extreme values of the input parameters which would lead, respectively, to the largest and smallest slopes. As indicated previously, only for the parameters h and ϕ_r were the upper and lower extremes for the input manipulated independently for the two altitudes in order to maximize slope (or intercept) differences. For all other inputs, if a positive (or negative) extreme was taken for the 10,000-ft model calculation, then a positive (or negative) extreme was also taken for the 5000-ft model calculation in order to determine bounds for slope and intercept. The resulting combinations are shown in Table 6.

WILLOW RUN LABORATORIES

TABLE 6. SPECIFIC VALUES OF THE MODEL INPUT PARAMETERS USED FOR CALCULATING LIMITING S-I (SLOPE-INTERCEPT) LINES

Input Parameter for Model	Value Used for Upper Limit S-I Line	Value Used for Lower Limit S-I Line	Spectral Channels
Extraterrestrial Solar Irradiance (E_0)	$1.06E_0(\lambda)^*$	$0.94E_0(\lambda)^*$	all
Visual Range (V)	25 km 40 km	40 km 25 km	1 to 10 11 and 12
Average Terrain Background Albedo ($\bar{\rho}$)	$\bar{\rho}(\lambda) + \Delta\bar{\rho}(\lambda)^{**}$	$\bar{\rho}(\lambda) - \Delta\bar{\rho}(\lambda)^{**}$	all
Sensor Height Above Terrain (h)	10,684 and 4684 ft 9684 and 5684 ft	9684 and 5684 ft 10,684 and 4684 ft	1 to 10 11 and 12
Nadir View Angle (θ_v)	14° 0°	0° 14°	1 to 10 11 and 12
Solar Zenith Angle (θ_0)	41.45° (10,000 ft) 39.04° (5000 ft)	45.45° (10,000 ft) 43.04° (5000 ft)	all
Relative Azimuth (ϕ_r)	38.1° (10,000 ft) 34.7° (5000 ft)	34.1° (10,000 ft) 38.7° (5000 ft)	all
Effective Channel (λ)	$\lambda - 0.01 \mu m^\dagger$ $\lambda + 0.02 \mu m^\dagger$	$\lambda + 0.01 \mu m^\dagger$ $\lambda - 0.2 \mu m^\dagger$	1 to 10 11 and 12

*See Figure 13

**See Table 6

†See Table 3

Figures 19 through 28 present, for each of the ten available spectrometer channels respectively, a graph of the upper and lower limit S-I lines calculated by the model together with the data points for each of the 18 targets as measured by the multispectral scanner. It can be seen that the majority of all the target data points lie either on the two S-I lines or in the region between these lines for all wavelengths except $0.422 \mu m$ (spectrometer channel 1). This indicates that, for most of the wavelengths, the measured data points lie within the upper and lower model-calculated boundaries determined using the estimated uncertainties in the values of the input parameters. The failure of the measured data to fall within the calculated limits for channel 1 (Fig. 19) can be ascribed either to an error in the calculated values or to an error in the measured values, or both. The dashed line in Fig. 19 is a least squares fit to the measured data, and indicates the average magnitude of the disagreement. If we assume that the model calculations are the predominant source of error, then such error should be systematically affecting other wavelengths, since the spectral parameters which are inputs or internal to the model are smoothly varying spectral functions. However, no such systematic discrepancy is evident for the other adjacent wavelengths (e.g., Figs. 20 and 21). The discrepancy in Fig. 19 could also be due to an error in scanner calibration. Such calibration is in fact accomplished essentially

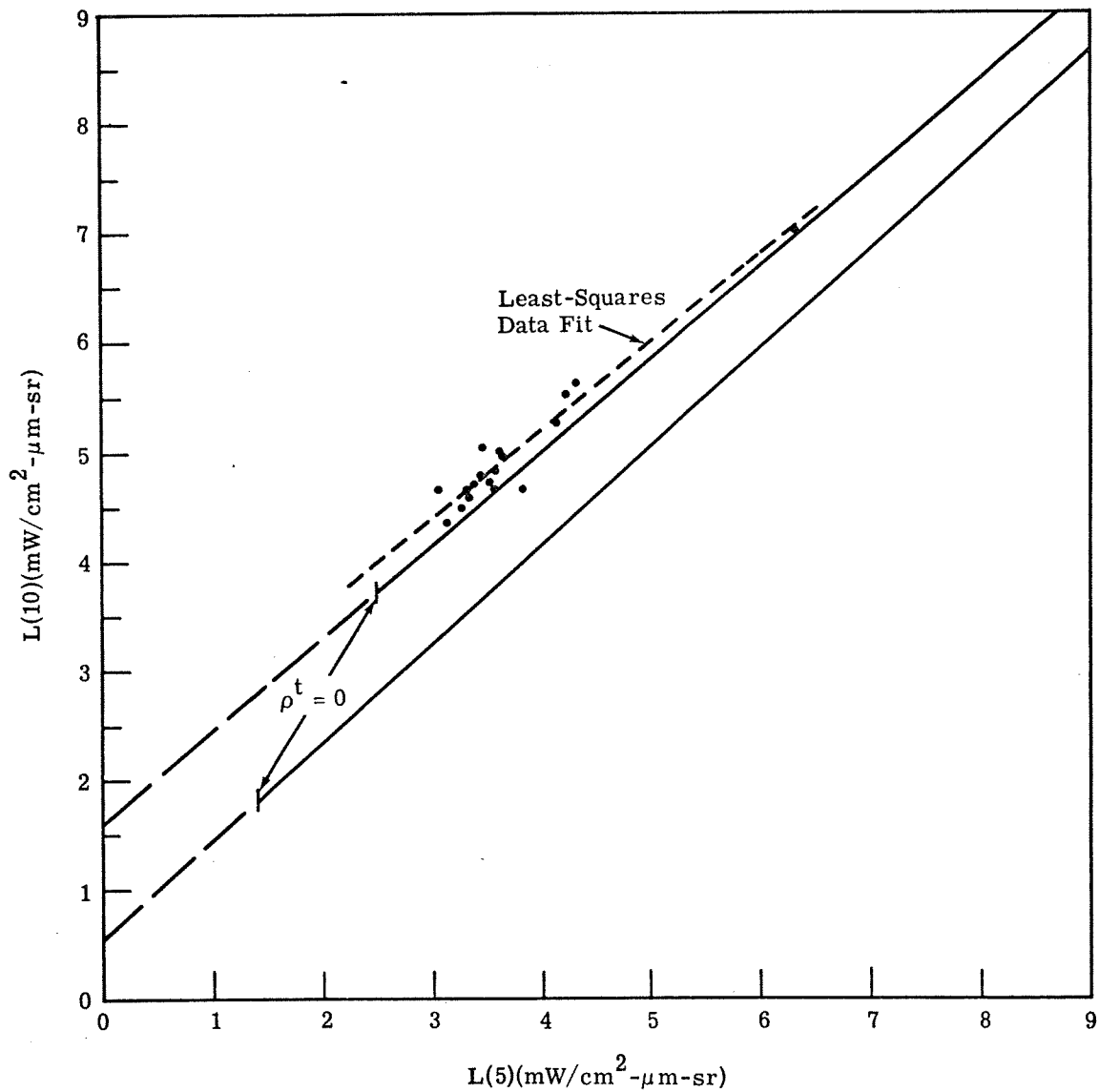


FIGURE 19. SLOPE-INTERCEPT COMPARISON AT 0.422- μm (SPECTROMETER CHANNEL 1). Solid lines are model-calculated S-I lines. Dots are measured data from multispectral scanner.

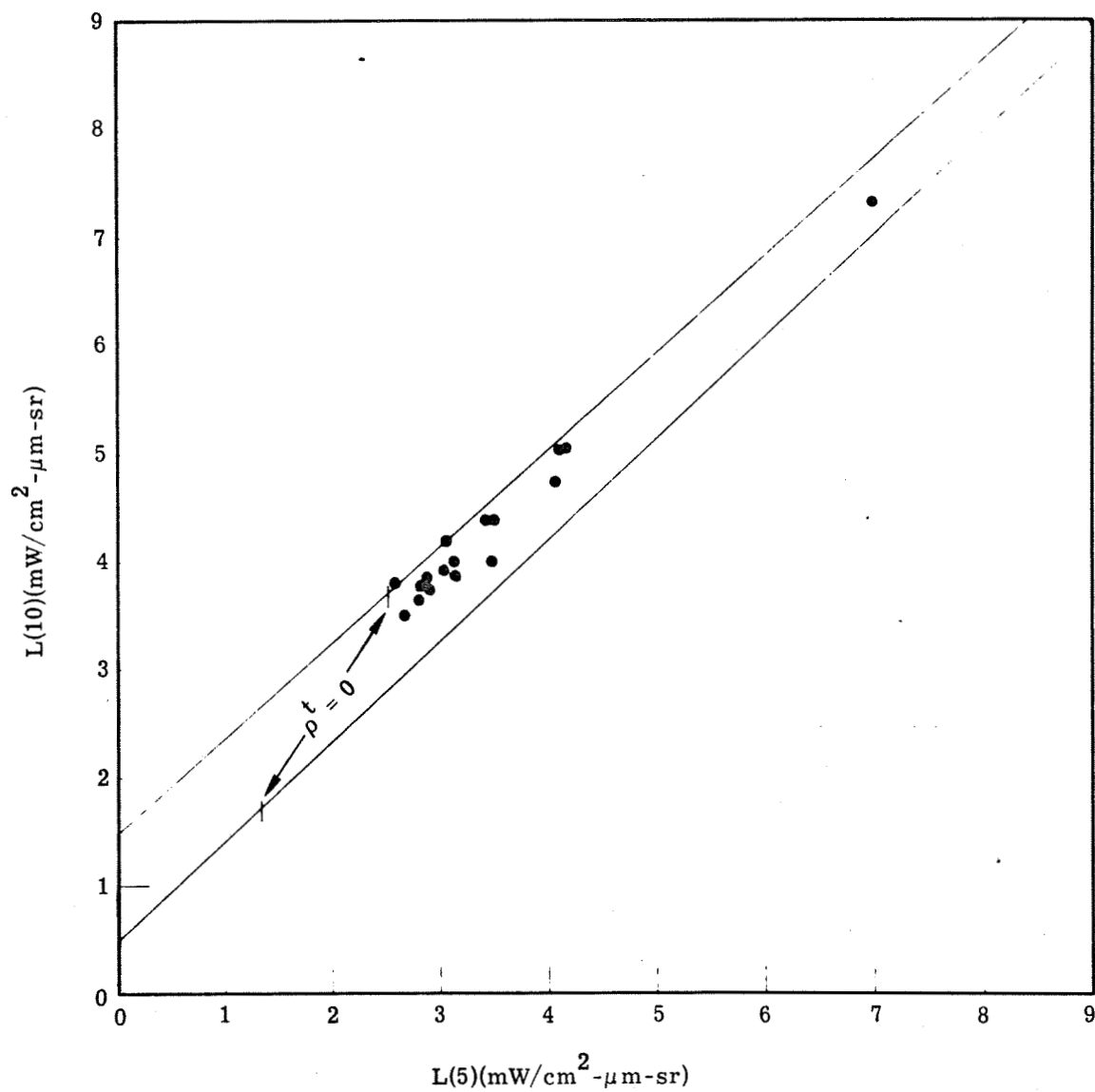


FIGURE 20. SLOPE-INTERCEPT COMPARISON AT $0.457 \mu\text{m}$ (SPECTROMETER CHANNEL 3). Solid lines are model-calculated S-I lines. Dots are measured data from the multispectral scanner.

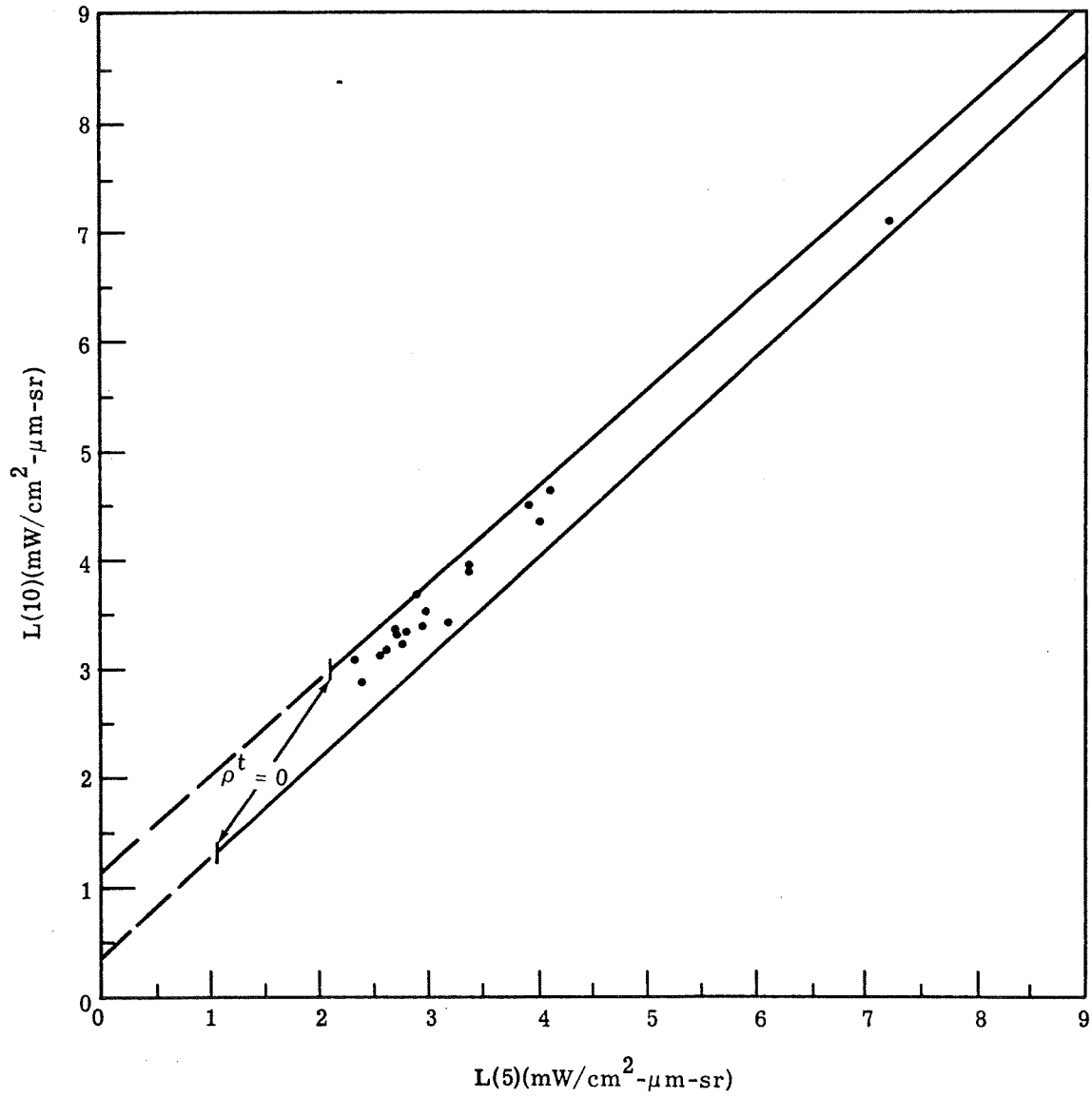


FIGURE 21. SLOPE-INTERCEPT COMPARISON AT $0.491 \mu\text{m}$ (SPECTROMETER CHANNEL 5). Solid lines are model-calculated S-I lines. Dots are measured data from the multispectral scanner.

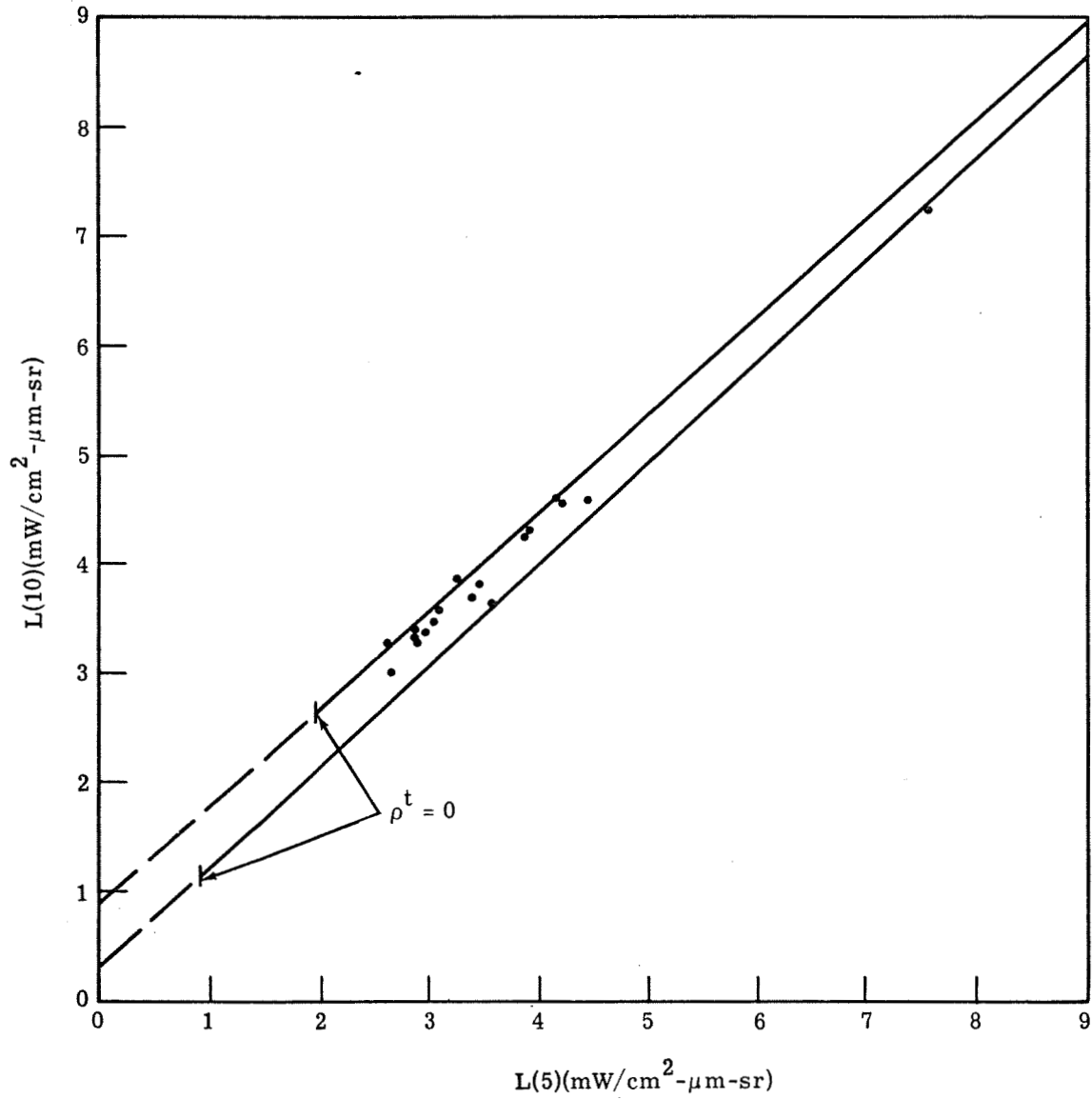


FIGURE 22. SLOPE-INTERCEPT COMPARISON AT $0.511 \mu\text{m}$ (SPECTROMETER CHANNEL 6). Solid lines are model-calculated S-I lines. Dots are measured data from the multispectral scanner.

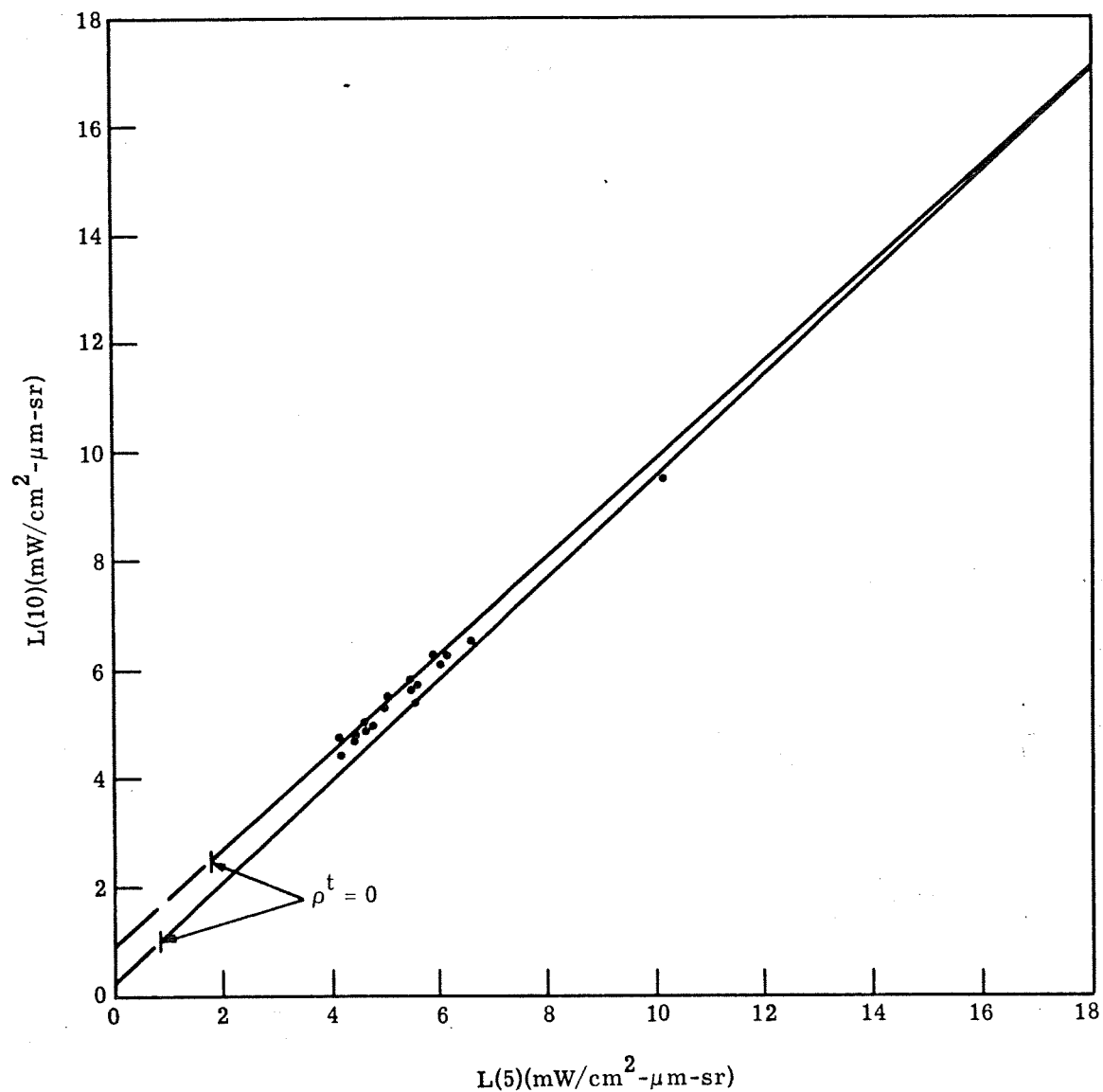


FIGURE 23. SLOPE-INTERCEPT COMPARISON AT $0.533 \mu\text{m}$ (SPECTROMETER CHANNEL 7). Solid lines are model-calculated S-I lines. Dots are measured data from the multispectral scanner.

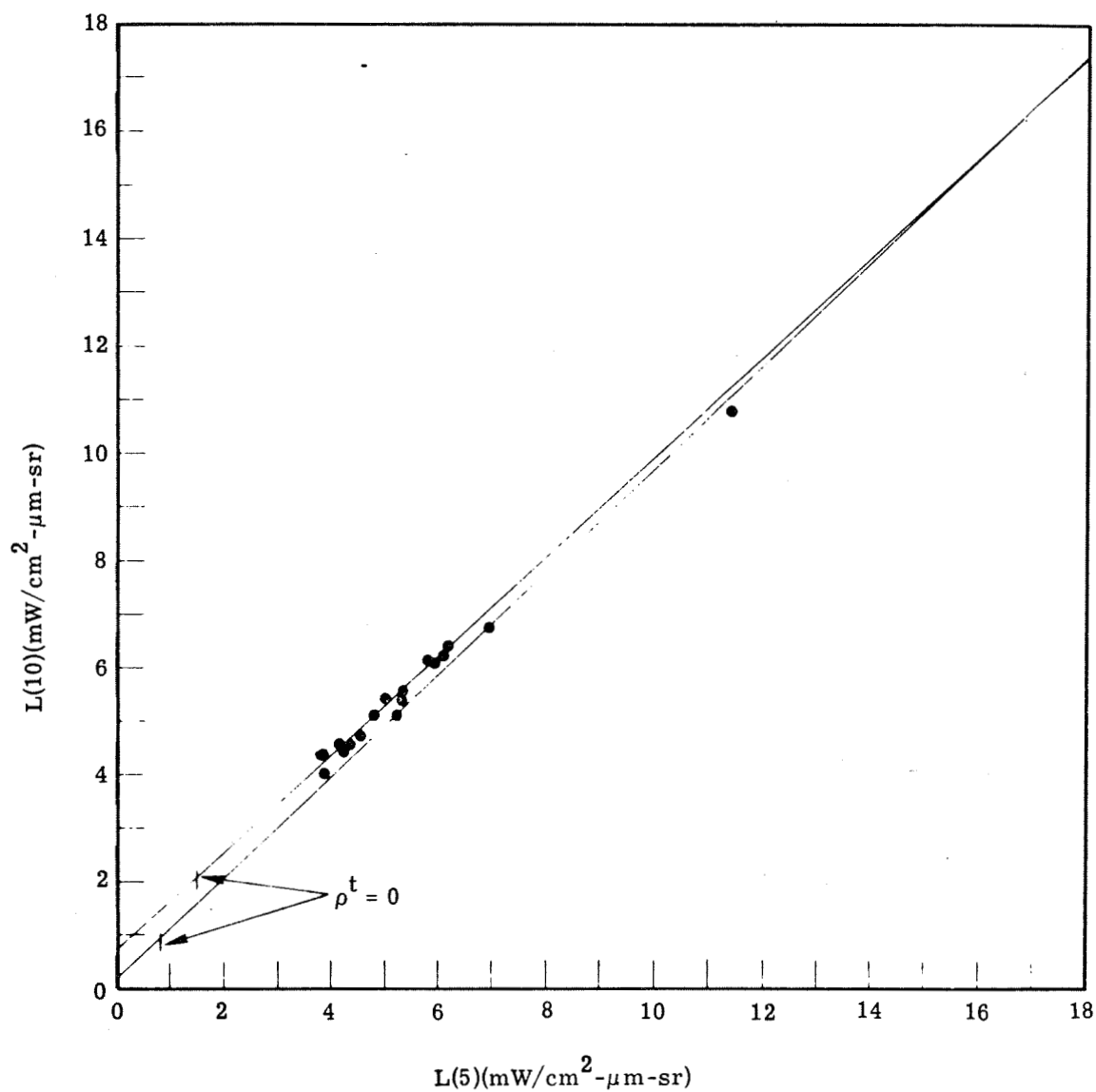


FIGURE 24. SLOPE-INTERCEPT COMPARISON AT $0.563 \mu\text{m}$ (SPECTROMETER CHANNEL 8). Solid lines are model-calculated S-I lines. Dots are measured data from the multispectral scanner.

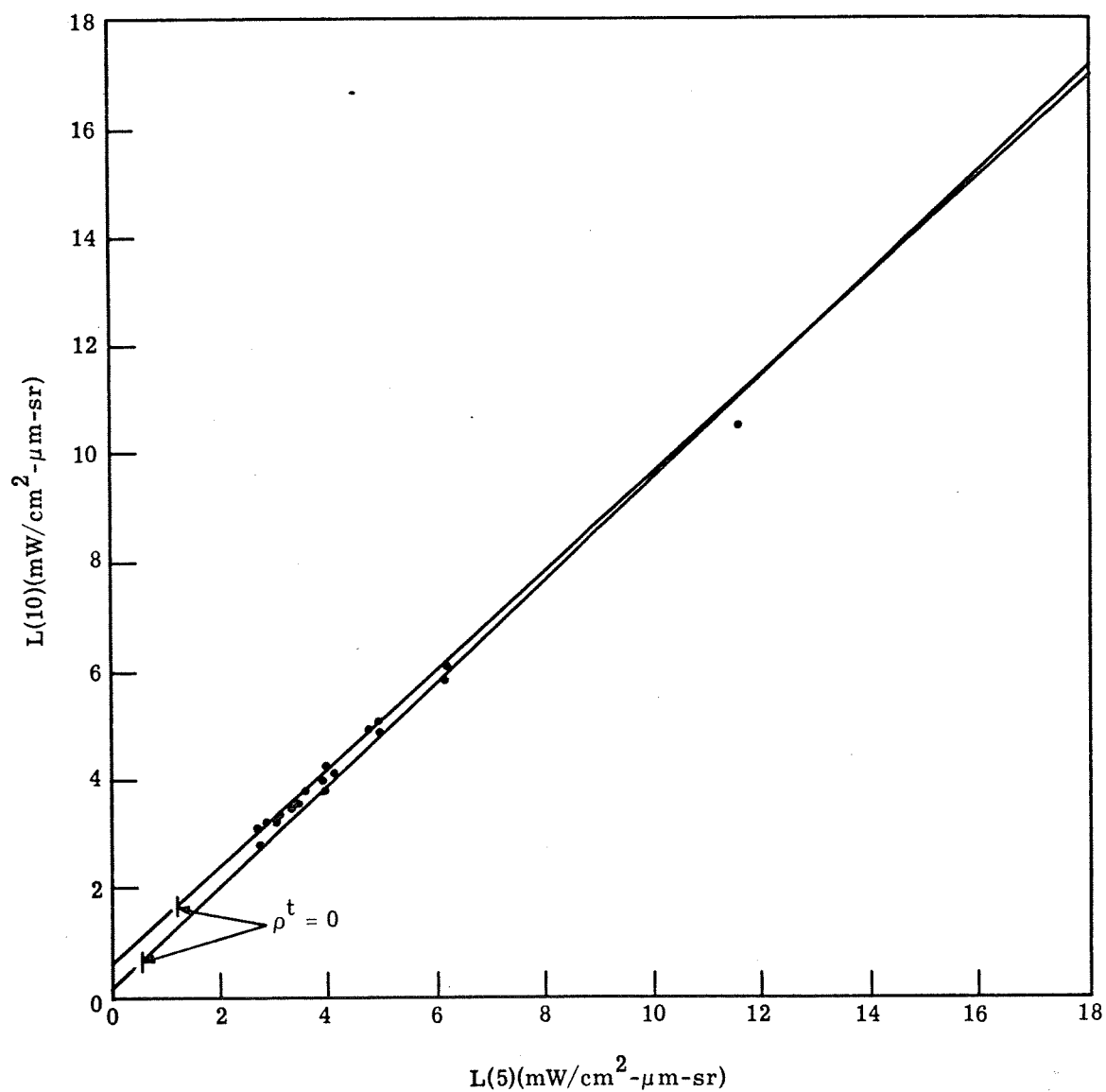


FIGURE 25. SLOPE-INTERCEPT COMPARISON AT $0.602 \mu\text{m}$ (SPECTROMETER CHANNEL 9). Solid lines are model-calculated S-I lines. Dots are measured data from the multispectral scanner.

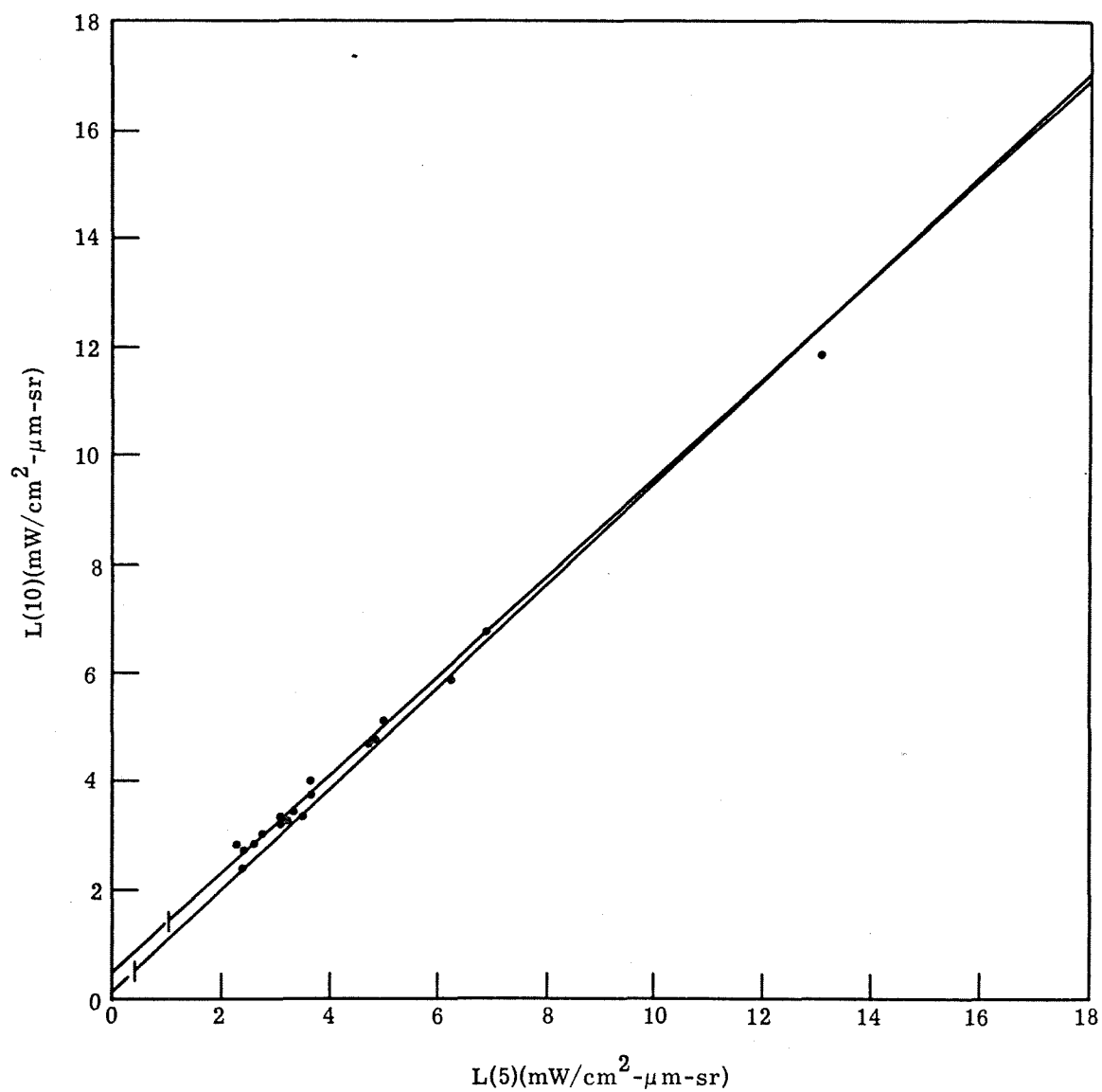


FIGURE 26. SLOPE-INTERCEPT COMPARISON AT $0.646 \mu\text{m}$ (SPECTROMETER CHANNEL 10). Solid lines are model-calculated S-I lines. Dots are measured data from the multispectral scanner.

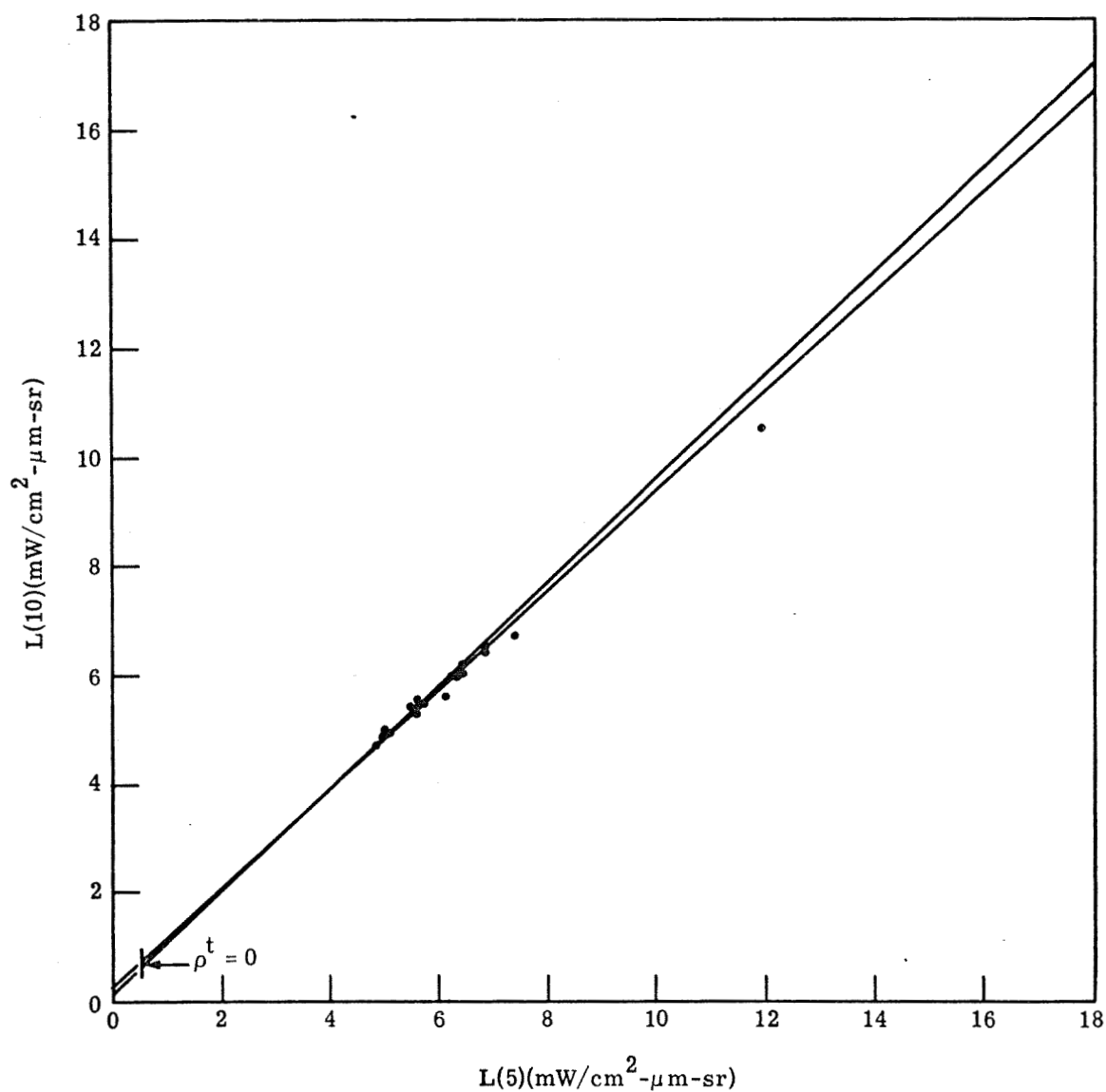


FIGURE 27. SLOPE-INTERCEPT COMPARISON AT 0.708 μm (SPECTROMETER CHANNEL 11). Solid lines are model-calculated S-I lines. Dots are measured data from the multispectral scanner.

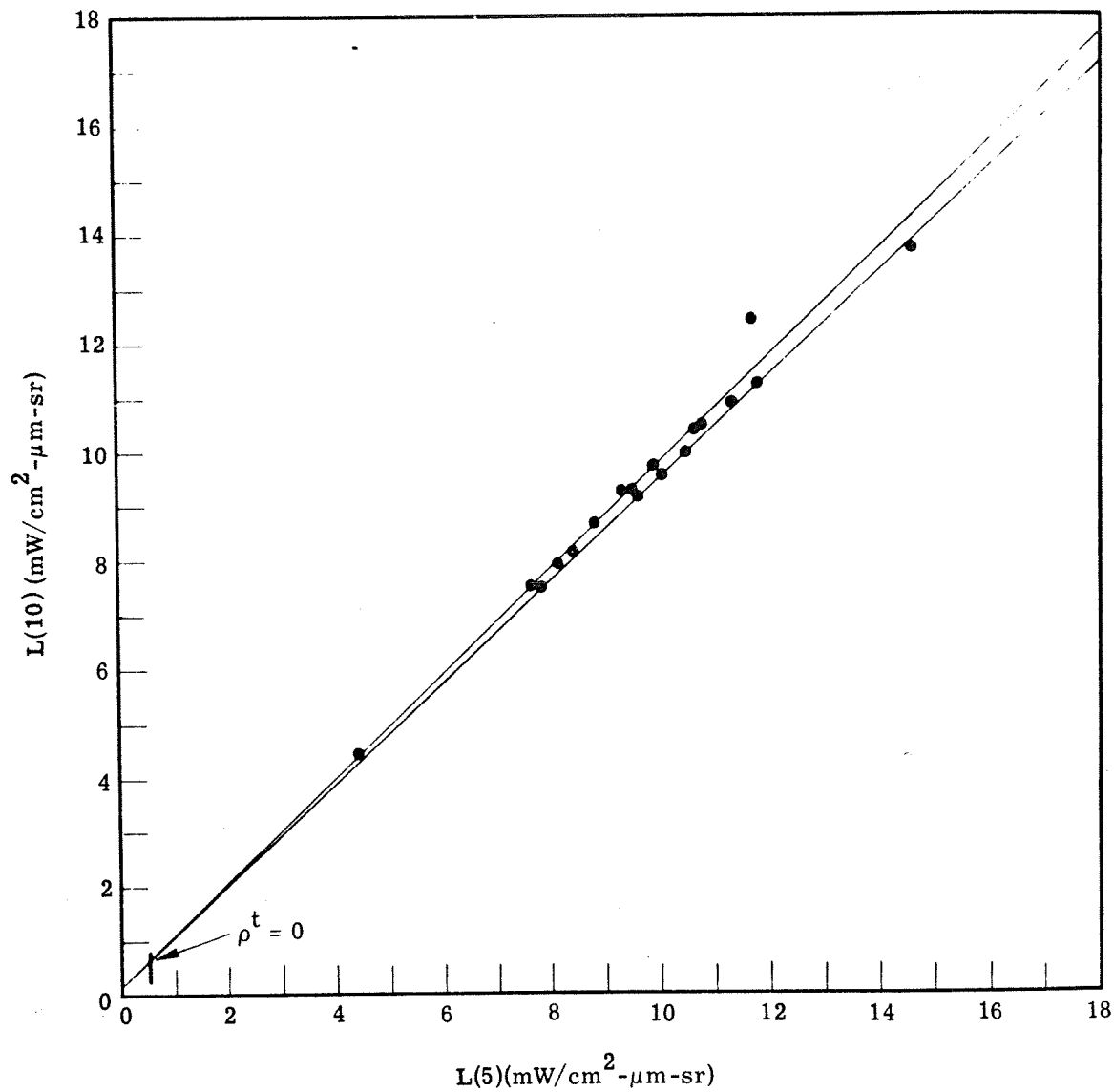


FIGURE 28. SLOPE-INTERCEPT COMPARISON AT 0.800 μm (SPECTROMETER CHANNEL 12). Solid lines are model-calculated S-I lines. Dots are measured data from the multispectral scanner.

independently for each channel, and so need not be systematic spectrally. If the calibration constant for channel 1 were reduced by 25%, the data points would move towards the origin of the graph and fall within the S-I limits indicated by the model, with the least squares line moving downwards but remaining parallel with itself. In retrospect, it is impossible to establish whether such calibration error was present. It is known, however, that successive calibrations of channel 1 have varied by about 20%. This is predominantly due to the fact that the standard lamp for radiance calibration has a precipitously changing spectral radiance output over the spectral bandwidth of channel 1. Thus, it is quite possible that the discrepancy shown in Fig. 19 can be attributed to the scanner calibration. Qualitative substantiation of this possibility is provided by the spectral curves of Figs. 15 and 16, which show unexpectedly high ρ^t values for $0.422 \mu m$ when compared to adjacent wavelengths. Such calibration error would also produce the relatively high $\overline{\Delta\rho}$ value seen for channel 1 in Table 3.

For all wavelengths, the measured data points of Figs. 19 through 28 tend to define empirical S-I lines having slopes which are less than the slopes of either of the S-I lines calculated using the model. Since the slope of any empirical line is not a function of scanner calibration (changing calibration would only translate a given line to another which was parallel), it appears that the model results do in fact exhibit a systematic error in determining at least part of the atmospheric effects upon these data.

The slope of an S-I line is proportional to a ratio of ground irradiances and to a ratio of transmittances (Eq. 5). Because of the short time interval between the aircraft overflights at 10,000 and 5000 ft, the irradiance ratio is nearly equal to one and cannot be significantly in error. Thus, the slope problem must be associated with the calculation of the transmittances. As is implied in the appendixes (I.3.2 and II.4), the transmittance is determined by the optical depth of the atmosphere, $\tau_{0,h}$, existing between the target at ground level and the sensor at altitude h . In turn, this optical depth is the sum of a Rayleigh scattering component and an aerosol scattering component.

The Rayleigh component is well-defined since it depends only upon the relationship between atmospheric pressure and altitude, a relationship which is quite universally applicable, at least near Earth's surface. However, the aerosol scattering component of $\tau_{0,h}$ depends upon the relationship between the aerosol number density and the altitude, a relationship which can be highly variable. The radiative transfer model uses specific number density profiles which represent, for a given surface visual range, empirically-determined mean values for the aerosol altitude distributions (Appendix I). These distributions are correct on the average, but may not hold for a particular time and place. The exact form of the altitude distribution is most important for near-surface calculations such as the present ones, since most of the aerosol particles exist in the first several thousand feet of atmosphere. In particular, since calculation of the transmittance to any particular altitude depends upon the integrated aerosol number density up to that

altitude, any profile errors will have greater effect upon a calculation at the 5000-ft altitude, than at 10,000 ft or higher.

For the calculated S-I lines of Figs. 19-28, a lower slope would result if T(5) were increased while T(10) remained unchanged. This could have been accomplished by assuming that the same number of aerosol particles existed between 0 and 10,000 ft, but that some of those assumed to lie between 0 and 5000 ft should really have been between 5000 ft and 10,000 ft. It is interesting to note that if such modification had been made, the decreased slope would have been accompanied by an increased intercept (see Table 5) so that the S-I lines of Figs. 19-28 would tend to rotate about an axis located somewhere near the middle of the L(5) scale. Thus, the relationship between such resultant calculated S-I lines and the majority of the experimental data points would remain essentially unchanged, while agreement would be improved for experimental points of high radiance (i.e., ρ^t) values.

4.2.3. VALIDATION SUMMARY

The results of the validation analysis presented in the preceding sections indicate that the atmospheric radiative transfer model is a credible tool for calculating the effects of the atmosphere on remote sensor data. The analysis of Section 4.2.1 emphasized the absolute accuracy of the model, and showed that agreement between experiment and theory was good for all wavelengths longer than about 0.45 μm . At shorter wavelengths, the agreement is less precise, but is very probably related to scanner calibration uncertainties rather than to any intrinsic defect in the model itself.

The analysis of Section 4.2.2 showed that uncertainties in the exact values of the environmental parameters used as model inputs can account for systematic errors in the calculations. These results are indicative of the fundamental accuracy limits that nature imposes upon the results of such modeling, without regard to the actual accuracy of the model.

It appears that use of the visual range at the surface as the only measure for the atmospheric aerosol distribution can lead to some calculation error for specific cases, even though it should lead to correct results on the average. Such possible error will probably be greatest for calculations applied to low aircraft altitudes and high target reflectances, and will quite probably be diminished for space altitudes and for average target reflectances. Visual range will remain the only generally available measure until finer measures are made standard and available to all remote sensing investigators.

SO-65 PHOTOGRAPHY CALIBRATION

One of the original goals of this program was to use the SO-65 photographic data from Apollo IX as a means for validating the ability of the radiative transfer model to correctly calculate the atmospheric effects present in space photographic data. A second goal was to then correct the SO-65 data for such atmospheric effects; i.e., determine the relation between the film density and the effective diffuse reflectance of ground targets. Our failure to accomplish the first of these goals is discussed in Section 5.1, while our accomplishment of a portion of the second goal by indirect methods is described in Section 5.2.

5.1. MODEL VALIDATION ATTEMPTS WITH SO-65 DATA

Section 4 of this report described two methods by which near-simultaneous multispectral line scanner data acquired at two flight altitudes could be used to evaluate the accuracy of the atmospheric radiative transfer model. These validation schemes required, as a minimum, three preconditions: (1) that the sensor be radiometrically calibrated to some minimal degree of absolute accuracy, but most important that it be highly repeatable in relative responsivity for the two altitudes; (2) that certain environmental parameters describing the atmospheric state be known (i.e., those required as model inputs); (3) that enough ground truth be available to allow at least a rough determination of the average background terrain albedo.

The relative success of the validation results of Section 4 indicates that all of these preconditions were met to a reasonable tolerance for the line scanner analysis. Thus, for a validation attempt utilizing both the scanner data and SO-65 camera data, at least conditions (2) and (3) above could be achieved since they are not sensor dependent. However, condition (1) above becomes very strict when the data at the two altitudes (i.e. space and 3 km) are provided by different sensors, for then the strong requirement of repeatable responsivity actually forces a requirement for good absolute accuracy from both sensors in order for their outputs to be comparable.

The characteristics of the Hasselblad cameras had been extensively measured and documented, both prior to space flight by the manufacturer, Carl Zeiss, and the Manned Spacecraft Center, and subsequent to the space flight by the Optical Sciences Center of The University of Arizona. Extensive sensitometry had been conducted by the Photographic Technology Laboratory at MSC and by Data Corporation in order to establish flight film process control procedures, to provide calibration film friskets on flight film emulsions, and to provide post-processing evaluations. The presence of this extensive data base provided some hope that an adequate calibration of the SO-65 data could be accomplished, despite the fact that photographic film is not usually considered an appropriate approach to calibrated radiometry. It was felt that some useful model validation results could be obtained if the film density on the reproduced transparencies of SO-65 data provided for this program could be related to a band radiance at the entrance aperture of the cameras with an accuracy of $\pm 30\%$.

An estimate of the accuracy with which the band radiance at the aperture can be determined from a measurement of film density on the original negative for these SO-65 cameras using type 3400 film is shown in Table 7. Only significant error sources (net effect $\geq \pm 1\%$) are included. In some cases even these had to be estimated. A net root-mean-square (rms) error of $\pm 28\%$ results if error independence is assumed. While this probably represents the minimum actual error, it is still a very good result for a photographic sensor. However, one possibly significant error source which could not be evaluated quantitatively is that of latent image failure during the time between exposure and processing. Flight film control friskets on type 3400 film which were exposed on or about 20 February 1969 and then processed with the actual flight film on or about 15 March 1969 exhibited significant changes in effective speed, gamma and maximum density when compared to similar friskets exposed and then processed without delay [6]. While such latent image failure is known to be a function of film environment and time, the exact relationship is not well understood. Thus, it is not known to what degree latent image failure may have affected the actual flight film.

In any event, the data of Table 7 show only the minimum error involved when the film density measurement is made on the original flight film. The actual transparencies available to this program were n-th generation enlarged positives (n is unknown). These would still have been useful if one could relate the film density on these transparencies to that on the original negatives. However, well into the program period it was learned that the transparencies provided had been produced using an uncalibrated enlarger and, even more significantly, had been hand processed without controls [7]. Lack of sufficient time remaining for preparation and analysis precluded the possibility of acquiring controlled transparencies. As a result, it was impossible to assign even a marginally useful calibration to the SO-65 photographic data on hand, and it was also impossible to use these data for even a rough validation of the atmospheric radiative transfer model.

5.2. SO-65 DATA CALIBRATION

One of the major advantages to be gained by having a radiometrically calibrated remote sensing device is that, in conjunction with a quantitative atmospheric model, remotely sensed target radiances may be corrected for atmospheric effects to produce a measure of the effective diffuse target reflectance, and thus a signature more closely representative of the intrinsic attributes of the target. As discussed in Section 5.1, direct calibration of the SO-65 data available to this program could not be accomplished. It was therefore necessary to resort to an indirect calibration method utilizing the Imperial Valley multispectral scanner data acquired nearly simultaneously with SO-65 data set AS9-26-3799. Three major steps were involved in this calibration: (1) extrapolation of the multispectral scanner data in altitude and time using the atmospheric radiative transfer model; (2) simulation of the in-band spectral radiance for each camera and for a range of targets by appropriate weighted summing of the higher spectral resolution scanner data; and (3) comparison of the simulated band radiance of selected targets to the film

TABLE 7. ESTIMATED MINIMUM RMS CALIBRATION ERRORS FOR SO-65 CAMERAS WITH TYPE 3400 FILM

(A) Determination of Absolute Film Exposure from Density Measured on Flight Film

Error Source	Absolute Error	Equivalent Density Error (at $D = 1$)
Data Corporation Sensitometer	± 0.08 log exp. (estimated)	± 0.11 (at $\gamma = 1.4$)
PTL Process Control	± 0.07 density [4]	± 0.07

RMS equivalent density error = ± 0.13 RMS equivalent film exposure error ($\gamma = 1.4$) = ± 0.093 log exp. = $\pm 24\%$ exp

(B) Determination of Absolute Band Radiance at Entrance Aperture from Calculated Film Exposure

Error Source	Absolute Error	Equivalent Exposure Error
Filter Transmission	$\pm 3\%$ absolute [5]	$> \pm 3\%$
Vignetting (off axis only)	$\pm 5\%$ [5]	$\pm 5\%$
Effective f-number	$\pm 5\%$ [6]	$\pm 5\%$
Shutter speed *	$\pm 7\%$ [6]	$\pm 7\%$
Spectral Integration of exposing energy and film spectral response	$\pm 10\%$ (estimated)	$\pm 10\%$

RMS equivalent film exposure error $\geq \pm 14\%$ (average of on- and off-axis)Total Estimated Minimum RMS Calibration Error = $\pm 28\%$

*Based on average difference in shutter speeds between pre-flight and post-flight calibrations.

density of those same targets on the space photography. Sections 5.2.1, 5.2.2 and 5.2.3 respectively described these three operations and the results obtained.

5.2.1. EXTRAPOLATION OF SCANNER DATA

The multispectral scanner data of Imperial Valley acquired on 12 March 1969 were described in Section 4. These data provided a base-line target measure which could be used for calibration of SO-65 data set AS9-26-3799 provided that the quantitative differences in atmospheric effects could be determined. This required an extrapolation not only in altitude (from 10,000 ft to ~ 100 miles) but also in time (from 1010 PST for the scanner to 0828 PST for the space photography).

It was shown in Section 4 that calibrated scanner data together with the atmospheric model could be used to calculate the effective diffuse spectral reflectance, ρ^t , of a target, t, by the relation

$$\rho^t = \frac{\pi [L_T^t - L_p(h)]}{E_g T(h)}$$

L_T^t was the measured target spectral radiance provided by the scanner, $L_p(h)$ and $T(h)$ were the spectral path radiance and transmittance calculated by the model for the appropriate environmental conditions and sensor altitude, and E_g was the total spectral irradiance onto the target calculated by the model for the specific environmental conditions. It follows that if ρ^t for a particular target is the same for the conditions of both the scanner data acquisition and the space photography acquisition, then that target can be used as a transfer standard, and the total spectral radiance for that target presented to the space cameras can be calculated using that ρ^t together with model calculations for L_p , T_v , and the particular E_g , appropriate to the atmospheric conditions.

The effective diffuse spectral reflectance, ρ^t , is a pure target attribute only if the target is in fact a diffuse reflector. If the target is not diffuse (as is usually the case), then ρ^t will in general vary with changes in either viewing geometry or illumination geometry, for it only describes the target reflectance for one particular combination of angles. Thus, in using the calibrated scanner data and atmospheric model to produce a space-extrapolated target radiance spectrum for SO-65 data calibration, only those targets for which the angular geometry of view and illumination were similar for the two sensors can be used.

As seen from the space photography of data set AS9-26-3799, the center point of that portion of the Imperial Valley covered by the scanner data was viewed at a nadir view angle of 10° on a true azimuth of 181° . For the 10,000 ft scanner data itself, the true view azimuth (defined by the ground projection of the scan direction to the south side of nadir) was 177° . Thus, for that scanner data obtained at a nadir view angle of 10° on this 177° true azimuth any structure effects

(row direction, projected leaf area index, etc.) on the effective diffuse spectral reflectance of a particular target should be essentially identical to that applicable to the space photography.

While the viewing geometries relative to the target structure were nearly identical for the scanner (at 10° nadir view angle) and the space photography, the absolute illumination geometries differed. For the space photography acquired at 0828 PST, the solar zenith angle was 58.8° and the true solar azimuth angle was 118.6°. At 1010 PST when the 10,000 ft scanner data was acquired, these angles were 43.5° and 141°, respectively. The relative illumination geometry can be calculated by determining the angle between the vector defining the viewing direction and the vector defining the direction of propagation of the direct solar beam into the target area. Such calculation shows an angle of 63.8° for the space photography and 51.8° for that part of the 10,000 ft scanner data taken with a nadir view angle of 10° on the 177° azimuth. This difference of 12° in the relative illumination geometries for the two data sets could affect the applicable value of the equivalent diffuse spectral reflectance. Reduction of this difference can be accomplished by using scanner data for a larger value of the nadir view angle. For example, the relative illumination angle for the scanner data at a 20° nadir view angle along the 177° azimuth is 60.5°, only 3.3° different from that for the space photography. However, this improvement in matching the illumination geometry decreases the matching of any effects resulting from target structure, as discussed in the previous paragraph. In particular, the effect on ρ^t caused by a changing projected leaf area index could be significant in going from 10° to 20° nadir view angle. For this reason, and for the reason that only a portion of the illumination is contained in the direct solar beam, it was decided that a 12° disparity in relative illumination angle could be accepted. Thus, those targets seen by the scanner at a 10° nadir view angle along the 177° azimuth were chosen to provide the transfer standards for space simulation.

The atmospheric model was used to determine the spectral path radiance, transmittance and irradiance on the ground for the conditions of the 10,000-ft scanner data acquisition (described in Section 4). The path radiance and transmittance necessary were only those calculated for the previously described viewing geometry to be used in the space photography calibration. These calculated values were used to transform the ten digitized spectral channels of scanner data so that the voltages now represented equivalent diffuse spectral reflectance, rather than spectral radiance. Since the transformation was accomplished as if all the scanner data had been acquired at the particular nadir view angle of interest, residual angle effects caused by improper atmospheric correction existed for the other angles in the data. At the same time, angular effects resulting from actual angular variations in ρ^t for a given target class also existed.

The residual angular effects were corrected empirically by means of the extensive ground truth data. The residual angular variation in ρ^t for specific target classes was determined from the data by locating as many fields of a given target class as possible and then plotting, for each spectral channel, the ρ^t value as a function of the particular view angle. Care was taken to ex-

clude portions of fields where the imagery or the ground truth indicated some peculiar condition existed (e.g., weed infestation or incomplete ground cover). From these angular variation curves for each spectral channel, a single angular correction function was determined which would flatten out the angular variations for all of the target classes so that, independent of angle, the ρ^t value for any field of a particular class would be the same as if it had originally been at the reference 10° view angle. These angular correction functions were then applied to the scanner data. Such correction was not necessary for the SO-65 calibration, since only the data at the reference 10° view angle would be used. However, such correction was advantageous to the ERTS and SKYLAB sensor simulation and analysis as will be described in Section 6.

Once the scanner data had been transformed to equivalent diffuse reflectance, the atmospheric model was again used to calculate the spectral path radiance, transmittance and ground irradiance applicable to the conditions under which the SO-65 data AS9-26-3799 were taken. These parameters were then used to transform and extrapolate the digitized scanner data into space. The result was a quantitative multispectral data set, calibrated in radiance, representing what the multispectral scanner would have produced had it been mounted in Apollo IX and had it looked at the same portion of Imperial Valley with the same ground resolution as that at the 10,000-ft altitude from which the data were acquired.

5.2.2. SIMULATION OF SO-65 PHOTOGRAPHIC DATA

Extrapolation of the multispectral scanner data to space provided the data base necessary to produce simulations of the SO-65 camera data. It was then necessary to determine how to add together weighted combinations of the ten available spectral channels in order to optimally simulate the actual spectral response of the three monochrome SO-65 cameras.

Figure 29 shows the relative spectral sensitivity of the monochrome SO-65 cameras [7] and of the ten available scanner channels. It can be seen that the relative narrowness and position of the scanner spectral channels can allow some latitude in matching the spectral sensitivity of the SO-65 bands, except for that of camera CC where only channel 12 of the scanner appears useful.

Several methods were available by which to select the weighting factors used to simulate the SO-65 spectral responses. The most straightforward approach would have been to select those scanner channels which fell within the spectral range of the response to the simulated, and then do a trial and error relative weighting in order to approximate the required spectral shape. After such fitting, the resulting simulation could be scaled so that the integrated spectral response (i.e., area under the curve) would equal that of the band to be simulated. Such a technique assures only that the absolute response will be correct for any spectrally flat radiance distribution. Another technique is to adjust the weightings in order to produce the best least-squares fit to the required spectral response shape. This requires an iterative process to minimize an implicit equation which may have more than one local minimum. In any case, such a technique

only insures that, if the probability of occurrence of any arbitrary spectral radiance distribution is as likely as that of any other, then the mean of the responses to all such distributions will be the same for the simulation as for the actual spectral shape (i.e., the simulation will make positive errors with the same facility that it makes negative errors).

The above techniques for simulation do not appear desirable since, for real scenes, target radiance distributions generally are not spectrally flat and do not represent a random selection of all hypothetically possible distributions. It was therefore decided to utilize a technique for determining simulation weights which forced the resultant simulation to perform exactly like the sensor being simulated for certain specific target spectral radiance distributions.

Consider a relative spectral response, $r_0(\lambda)$, for which a simulation is desired. A number n of narrow spectral bands of relative response $r_i(\lambda)$ ($i = 1, n$) are available for producing such a simulation, for which n weights w_i must be determined. A particular target has a spectral radiance, $L(\lambda)$. This produces a band radiance, L^B , (i.e., a response) in the actual system of

$$L^B = \int_0^{\infty} r_0(\lambda) L(\lambda) d\lambda \quad (15a)$$

To produce a correct simulation, the weights for the n simulating channels must be such as to result in the same L^B , vis:

$$\int_0^{\infty} r_0(\lambda) L(\lambda) d\lambda = \sum_{i=1}^n w_i \int_0^{\infty} r_i(\lambda) L(\lambda) d\lambda \quad (15b)$$

This is one linear equation in n unknowns, w_i . Obviously, by choosing n different target radiance distributions, $L_j(\lambda)$ ($j = 1, n$), n simultaneous linear equations in the n unknowns w_i result. These may be uniquely solved for the w_i so long as none of the $L(\lambda)$ are linear combinations of any subset of the others, i.e., so long as the resultant equations are independent. Thus, if four spectral bands $r_i(\lambda)$ are to be used in simulating $r_0(\lambda)$, this simulation can be made perfect for four particular target spectral radiance distributions and for any linear combination of those distributions. Judicious choice of the $L_j(\lambda)$ can make the simulation even more generally applicable.

The simulation of the SO-65 cameras was conducted in order to calibrate the SO-65 data. Therefore, the particular $L_j(\lambda)$ used to determine scanner channel simulation weights were derived directly from the selected targets present in the space-extrapolated scanner data which would provide the calibration. Fourteen target areas present in the scanner data were selected and their space-extrapolated spectral radiance distributions determined from the ten available spectral channels. Target selection was based upon four criteria: (1) the target was located within $\pm 3^\circ$ of that position in the scanner data for which the space extrapolation was considered

WILLOW RUN LABORATORIES

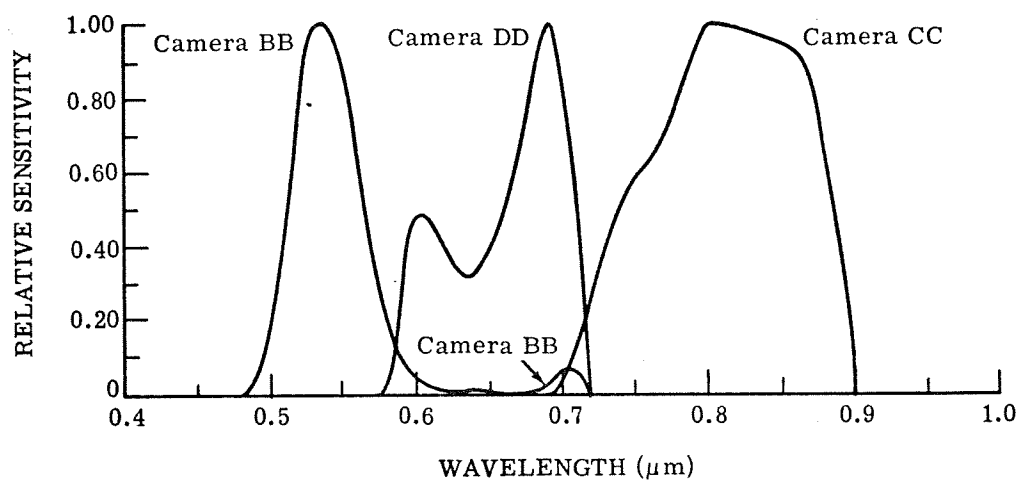
most accurate (see Section 5.2.1); (2) the target was uniform in appearance in the scanner imagery and described as homogeneous in content in the ground truth observations; (3) the target was large enough (at least 500-ft square) to be easily located and defined in the space photography; and (4) the total set of such targets adequately represented all the major target classes present in the data, and adequately represented the spectral variability and dynamic range of the scene.

Each of the SO-65 camera responses of Fig. 29 was simulated by means of a subset of the available scanner channels and target radiance distributions. The particular subset of targets chosen for each determination of simulation weights corresponded to those exhibiting the most dissimilar spectral characteristics within the spectral range of the particular SO-65 band being simulated. Table 8 defines the particular scanner bands used for each simulation. Also shown is an independent measure of the overall accuracy of each simulation in terms of how well the simulated SO-65 band matches the actual SO-65 band in terms of its response to those targets not used in producing the simulation weights. The simulation errors for Camera BB are quite small. This is due to the large number of scanner channels which could be used, and as a result, the variety of target spectra for which the simulation could be made exact. The simulation errors for Camera CC are probably representative of the best that can be expected when only one scanner channel is available for simulation. The very low mean error in relation to the RMS error results from the fact that the simulation overestimates the response to healthy vegetation by 1 to 2% and underestimates the response to soil and dead vegetation by an equal amount. The simulation errors for camera DD are worse than those for camera CC, despite the use of three scanner channels for the former. This results from the odd shape of Camera DD's spectral response (see Fig. 29). One problem is that this spectral shape is highly correlated with that of vegetation. This results from the pronounced local minimum at about 0.64 μm . In addition, the fact that the peak response for Camera DD occurs near 0.69 μm requires that scanner channel 11 be used in the simulation, even though use of this channel leads to undesirable response in the 0.71- to 0.79- μm range where vegetation spectra are significantly increasing. These factors result in a 1 to 4% over-estimation of response to some healthy vegetation and a 1 to 2% under-estimate of response to some soils.

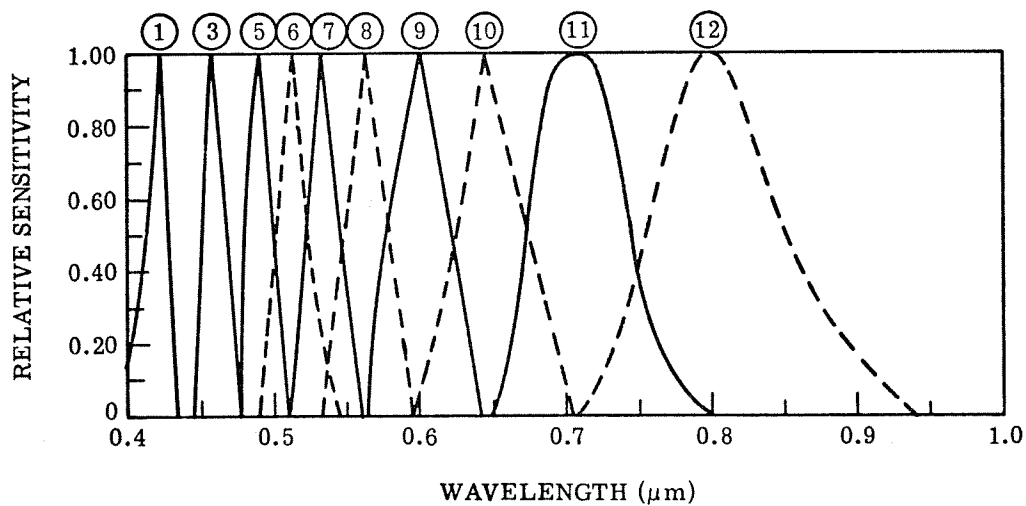
TABLE 8. SIMULATION ACCURACY FOR SO-65 CAMERAS

SO-65 Camera	n	Scanner Channels	Simulation Errors for 14-n Targets		
			rms (%)	Mean (%)	Largest (%)
BB	5	5, 6, 7, 8, 11	0.125	-0.094	-0.233
DD	3	9, 10, 11	1.725	0.525	3.750
CC	1	12	1.405	0.095	2.100

While certain deficiencies in the selected technique for simulation have been pointed out, the overall result appears quite acceptable. Simulation errors on the order of 2 or 3% for those targets to be used in calibrating the SO-65 photographic data certainly cannot be considered



(a) SO-65 Monochrome Cameras [7]



(b) Multispectral Scanner (10 bands only)

FIGURE 29. RELATIVE SPECTRAL SENSITIVITY

significant in comparison to other possible error sources involved. In any case, the selected technique would seem to be the optimum deterministic method for accomplishing such simulations.

5.2.3. SO-65 CALIBRATION

The space-extrapolated simulations of the three SO-65 monochrome bands discussed in previous sections provided the means for calibrating the space photography of data set AS9-26-3799. Such calibration required the further step of comparing the film density of selected targets on the transparencies to the band radiance for those same targets on the simulations.

Positive transparencies of SO-65 data sets AS9-26-3799 (Imperial Valley), AS9-26-3698 (Imperial Valley), AS9-26-3727 (Houston-Galveston) and AS9-26-3741 (Mississippi River) were digitized by Optronics International, Inc. The digitization was accomplished on a rotating drum scanner by means of a 50- μ m square aperture and a 50- μ m raster advance per scanline. Because of size limitations on the drum, only a 7- by 5-in. area on the enlarged ($\approx 4X$) transparencies could be digitized. Specular optical density was measured with 8 bit (256 level) resolution over the range 0 to 3D ($\Delta D \approx 0.0117$). These data were recorded on-line by Optronics in 9-track NRZI 800 bpi format. Willow Run Laboratories' IBM 360-67 computer was used to reformat the data into 7 track 200-bpi packed mode which was identical to the format of the digitized multispectral scanner data. Thus, all software processing routines developed for the multispectral scanner data could be used on the digitized SO-65 photographic data.

The 50- μ m sampling aperture for digitization corresponds to 10 line pairs per mm sampling resolution on the enlarged transparency, which in turn is equivalent to about 40 line pairs per mm on the original 70-mm format for the SO-65 data. Thus, considering reproduction degradation, the sampling resolution was probably equal to or better than the actual resolution available in the data [7]. In any case, the sampling resolution was equal to a spot size of about 110 ft on the ground.

Density contour maps (gray maps) of the digitized space photography for Imperial Valley data set AS9-26-3799 were prepared and compared to similar maps made from the multispectral scanner data. The fourteen previously selected target areas (Section 5.2.1 and 5.2.2) were located on the space data and the data points falling within the boundaries of those target areas defined as accurately as possible. Finally, the mean recorded film density for each of these targets on the digitized space photography was calculated as was the mean for the band radiance of the scanner simulations. Since the film density resulting from the photographic process is proportional to the logarithm of the exposure (and thus the logarithm of the band radiance) the mean band radiance, \bar{L}^B , for each target in the simulated data was determined logarithmically

$$\bar{L}^B = \log^{-1} \left[\frac{1}{N} \sum_{i=1}^N \log L_i^B \right]$$

where N is the number of data points within the target area. Actually, however, the criterion of uniformity in the fourteen selected target areas was met so well that the variance in the simulated data was very small and the resultant \bar{L}^B was not significantly different from that derived by an arithmetic mean calculation.

Figures 30, 31, and 32 show plots of specular optical density versus mean band radiance for the photography of data set AS9-26-3799. These graphs constitute the calibration curves for the particular transparencies provided to this program. The upper scale in these figures shows the diffuse reflectance which would produce a particular band radiance for the atmospheric conditions and geometry applicable to this data set.

A solid line representing a least squares fit to the data is shown in each of Figs. 30, 31, and 32. The film gamma calculated for these lines is also shown in the figures. The rather significant difference in gamma for the three transparencies is probably indicative of the uncontrolled reproduction processing, since the original flight film control process was designed to achieve a common gamma (≈ 1.4) for all monochrome bands [29]. Whether these calibration lines should really be straight after several generations of reproduction is of course open to question. Such an assumption seems well founded for the Camera DD transparency (Fig. 32), while for the Camera CC transparency (Fig. 31) a curved calibration such as shown by the dashed line could be justified as easily as the straight line. It is interesting, although not necessarily significant, to note that this curved line would blend nicely into the data of Fig. 30 with a minor shift in the band radiance scale.

Regardless of the kind of calibration line derived from the data of Figs. 30, 31, and 32, it is impossible to estimate the absolute accuracy of the result. Error sources include:

- (1) the SO-65 spectral responses, which were not measured but calculated using the film manufacturer's standard response data [7]
- (2) the absolute calibration of the multispectral scanner
- (3) the accuracy of the radiative transfer model calculations including both intrinsic errors and those resulting from errors in the input parameters
- (4) the simulation technique
- (5) possible errors in determining the exact location in the digitized space photography corresponding to the fourteen target areas used from the space-extrapolated scanner simulation.

Thus, it would seem reasonable to accept the premise that the straight lines in Figs. 30, 31, and 32 represent as good an approximation to the true calibration as is justified for this data set.

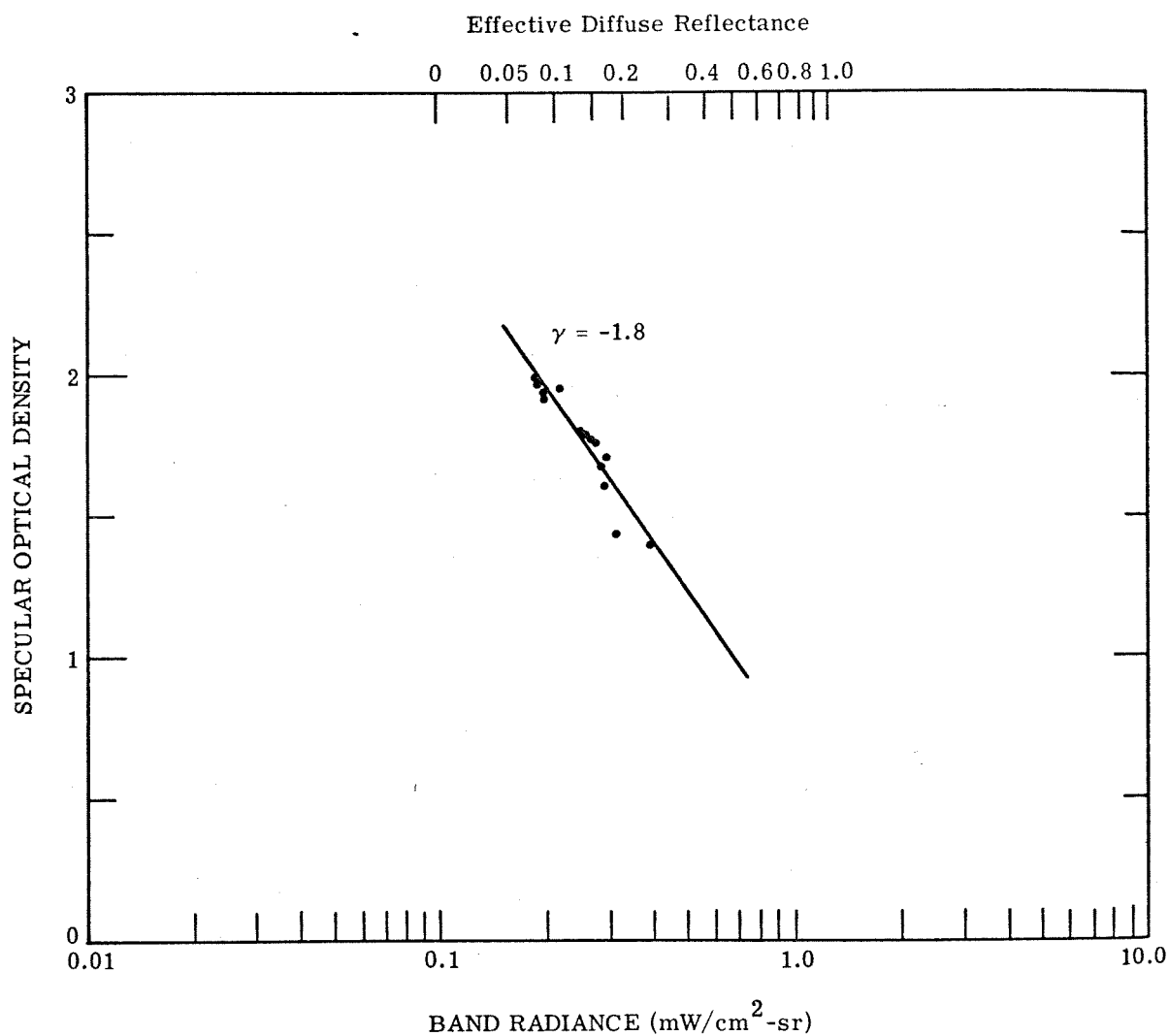


FIGURE 30. CALIBRATION CURVE FOR AS9-26-3799B: SO-65 CAMERA BB POSITIVE TRANSPARENCY. Calibration applies only to the particular transparency used.

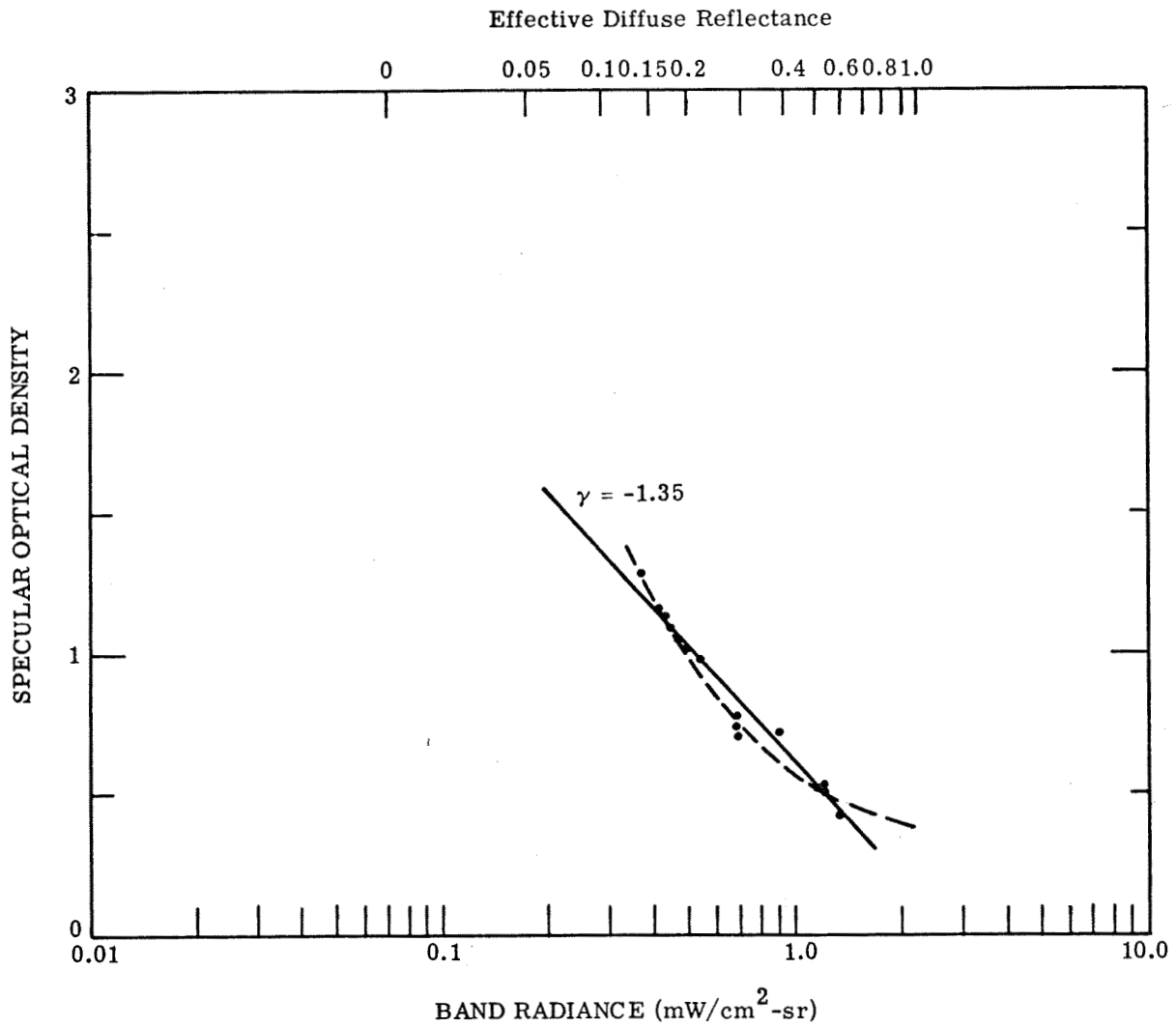


FIGURE 31. CALIBRATION CURVE FOR AS9-26-3799C: SO-65 CAMERA CC POSITIVE TRANSPARENCY. Calibration applies only to the particular transparency used.

WILLOW RUN LABORATORIES

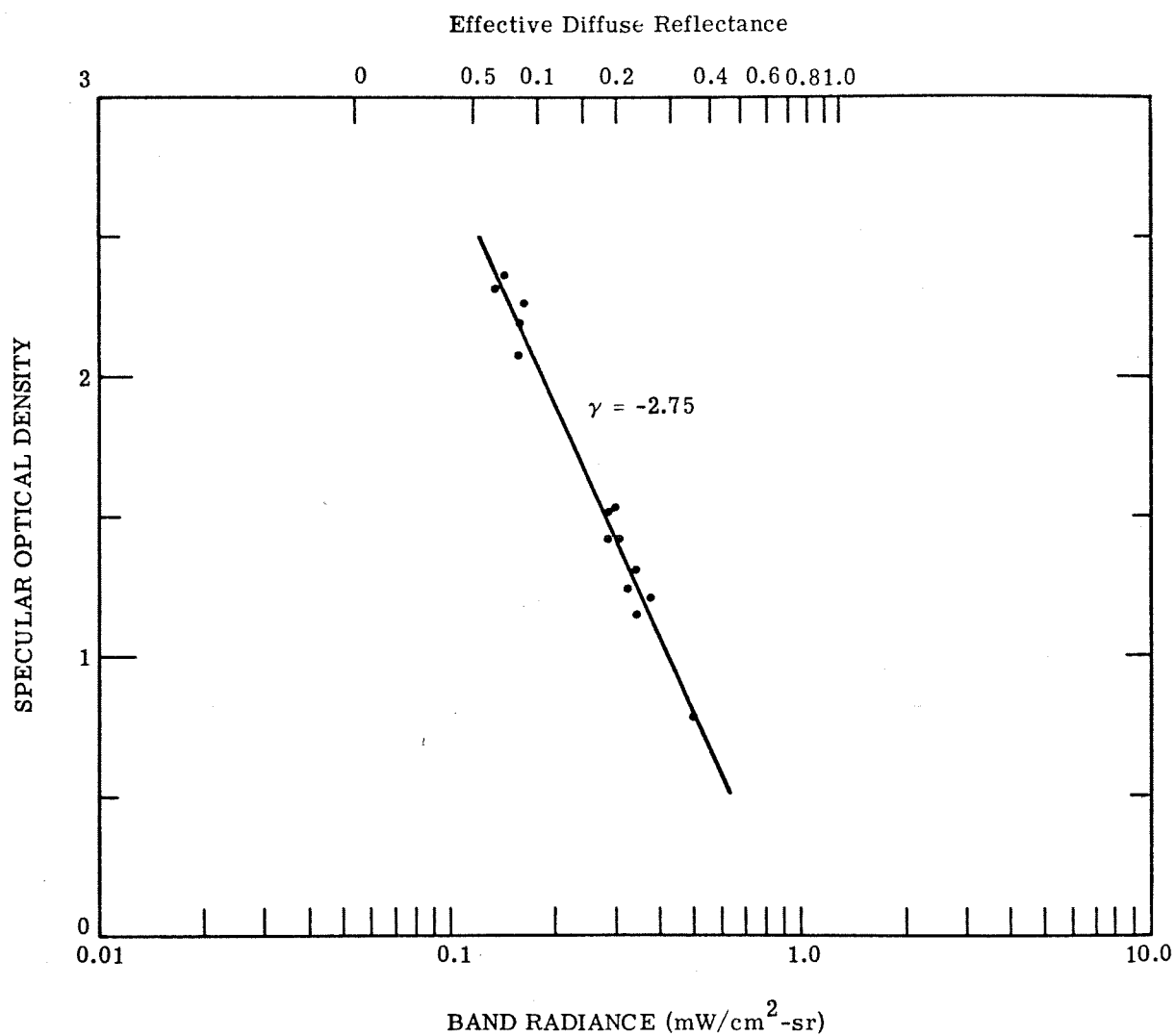
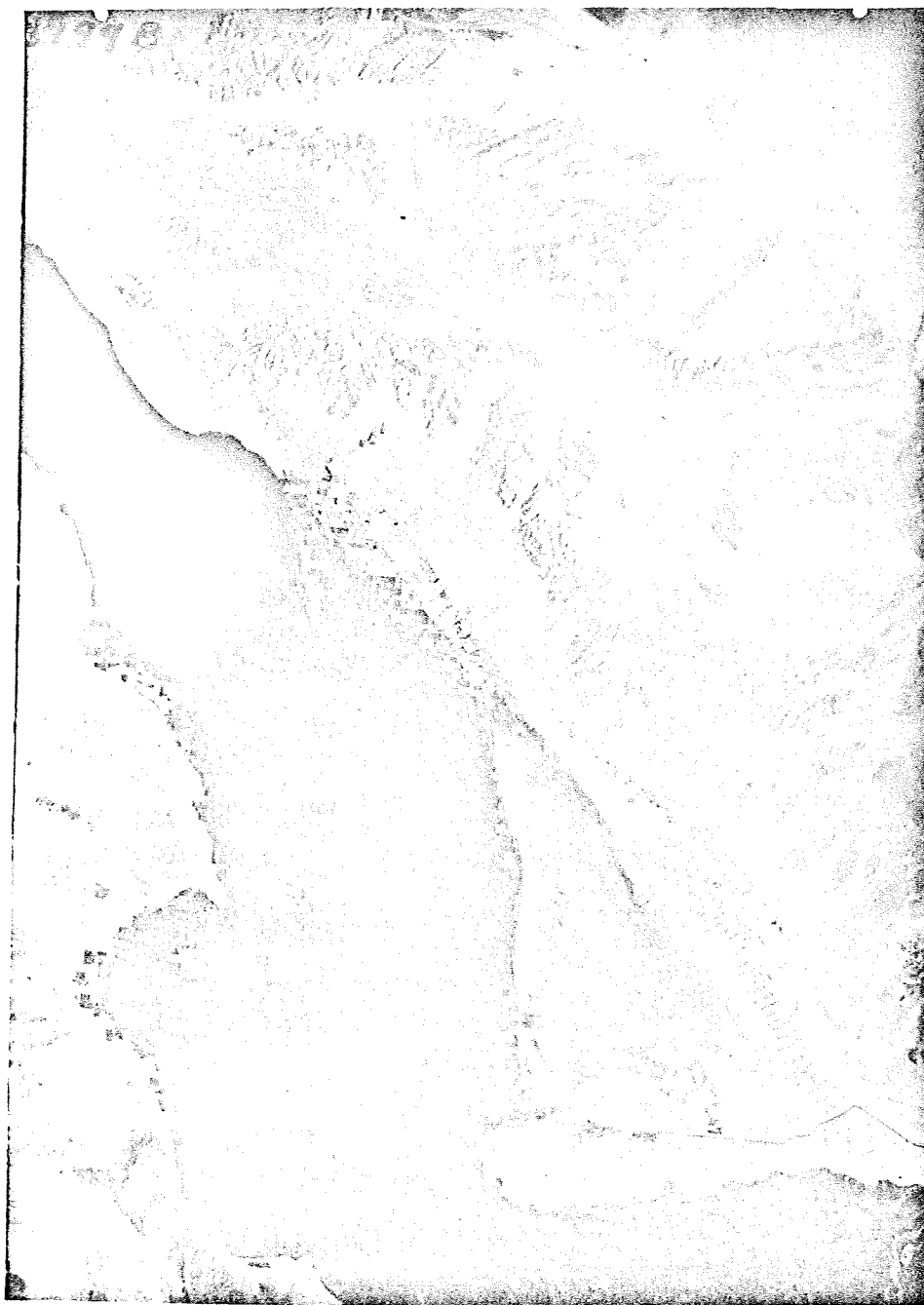


FIGURE 32. CALIBRATION CURVE FOR AS9-26-3799D: SO-65 CAMERA DD POSITIVE TRANSPARENCY. Calibration applies only to the particular transparency used.

WILLOW RUN LABORATORIES

Figures 33, 34, and 35 are calibrated reproductions of the monochrome bands of SO-65 data set AS9-26-3799. The density of each numbered step in the gray scale represents a particular effective diffuse reflectance determined using the least-squares fitted straight lines of Figs. 30, 31, and 32. Because of the uncalibrated processing applied to the transparencies provided to this program, the calibration applies only to that indicated portion of the frame where the scanner data were available. Positive transparencies of Figs. 33, 34, and 35 may be found in the jacket attached inside the back cover of this report.

Calibration of SO-65 data sets AS9-26-3698 (Imperial Valley), AS9-26-3727 (Houston-Galveston) and AS9-36-3741 (Mississippi River) was not attempted. The lack of controlled photographic reproduction made it impossible to transfer the partial calibration achieved for data set AS9-26-3799. At the same time, the absence of either simultaneous underflights with a radiometrically calibrated scanner, or any quantitative inscene reference precluded the possibility of independent calibration.



Effective
Diffuse
Reflectance

	—
	—
	—
	1.30
	0.95
	0.72
7	0.55
8	0.41
9	0.28
10	0.20
11	0.12
12	0.07
13	0.04
14	0.00
15	—
16	—

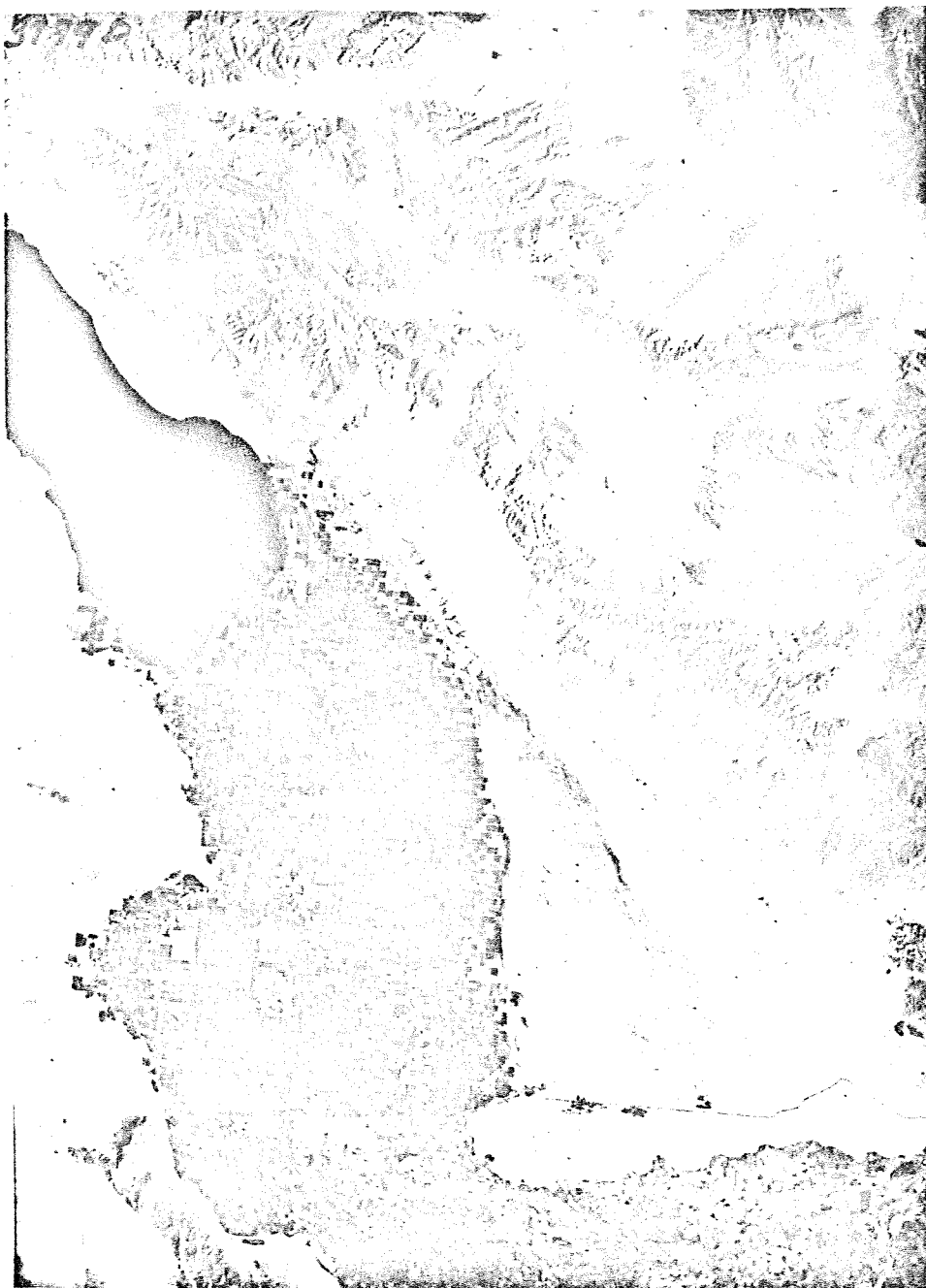
FIGURE 33. CALIBRATED REPRODUCTION OF SO-65 FRAME AS9-26-3799B. Calibration applies only in the lower quarter of the right half of the cultivated mitten-shaped area.



Effective
Diffuse
Reflectance

	1.08
	0.90
	0.78
	0.61
	0.49
	0.34
	0.23
	0.16
	0.10
	0.06
	0.03
	0.01
	-
	-
	-
	-

FIGURE 34. CALIBRATED REPRODUCTION OF SO-65 FRAME AS9-26-3799C. Calibration applies only in the lower quarter of the right half of the cultivated mitten-shaped area.



Effective
Diffuse
Reflectance

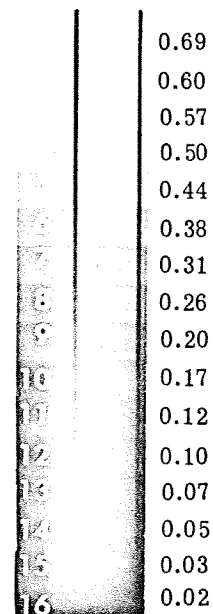


FIGURE 35. CALIBRATED REPRODUCTION OF SO-65 FRAME AS9-26-3799D. Calibration applies only in the lower quarter of the right half of the cultivated mitten-shaped area.

ANALYSIS OF SIMULATED ERTS AND SKYLAB DATA

The atmospheric radiative transfer model, together with the simulation technique developed during the program, provided means by which simulations of the multispectral data to be acquired by ERTS and SKYLAB-EREP sensors could be accomplished. Such simulations were generated from the multispectral scanner data of Imperial Valley for the Return Beam Vidicon (RBV) and Multispectral Scanner (MSS) sensors of the ERTS-A spacecraft, and for the first seven channels of the S-192 scanner in the Earth Resource Experiment Package (EREP) of SKYLAB. These simulations were then analyzed in order to assess their relative multispectral recognition capabilities, and also to evaluate the utility of a new approach to multispectral recognition especially designed to minimize recognition problems resulting from the coarse spatial resolution inherent in space-acquired remote sensor data. Simulated imagery of the S-192 multispectral scanner was produced and is presented in Appendix III.

6.1. SIMULATION

In order to accomplish calibration of the monochrome bands of the SO-65 photography, the multispectral scanner data acquired over the Imperial Valley were extrapolated to space using calculations produced by the radiative transfer model. This operation, as described in Section 5.2.1, provided a multispectral data set, calibrated in radiance, representing what the multispectral scanner would have produced had it been mounted in Apollo IX and had it looked at the same portion of Imperial Valley with the same ground resolution as that at the altitude of 10,000 ft from which the data were acquired. These data thus provided a means for simulating what the RBV, MSS and S-192 sensors would have produced had they been mounted in Apollo IX.

With the use of the available data for the spectral responses of the three RBV and the four MSS channels [10], and the first seven channels of S-192 Unit 2 [11, 12], the technique described in Section 5.2.2 for determining appropriate channel weightings for the space-extrapolated scanner data was applied. The same 14 target radiance distributions used for the SO-65 simulations were used here, with the choice of particular targets for weighting calculation again made using the criterion of choosing those with the most dissimilar spectral characteristics within the spectral band being simulated. Table 9 describes the particular M-5 scanner channels (see Fig. 29) used in the simulations.

As was done for the SO-65 simulations, a check of the simulation accuracy was accomplished using those targets not involved in determining simulation weights. These results are also shown in Table 9. The simulation errors shown in Table 9 are very small for those simulations for which more than one M-5 scanner channel could be used. Conversely, as expected the errors are generally much larger where only one M-5 channel was used; S-192 channel 7 is an exception, apparently because M-5 channel 12 is a very good spectral match to it. The simulation errors for S-192 channel 6 are quite large, even though M-5 channel 11 used to simulate it does have a

TABLE 9. SIMULATION ACCURACY FOR ERTS AND SKYLAB SENSORS

Sensor	Channel	n	M-5 Channels Used	Simulation Errors for 14-n Targets		
				rms (%)	Mean (%)	Largest (%)
RBV	1	5	3, 5, 6, 7, 8	0.056	0.019	-0.083
	2	2	9, 10	0.029	-0.001	0.056
	3	1	11	5.478	-1.570	-9.790
MSS	1	4	6, 7, 8, 9	0.181	-0.131	-0.348
	2	2	10, 11	0.451	-0.372	1.030
	3	2	11, 12	0.423	-0.335	-0.821
	4	1	12	6.102	0.079	-8.460
S-192	1	1	3	2.815	-1.569	-4.750
	2	3	3, 5, 6	1.001	-0.768	-1.830
	3	3	6, 7, 8	0.074	-0.043	-0.128
	4	3	7, 8, 9	0.044	-0.032	-0.081
	5	2	9, 10	0.544	-0.075	1.230
	6	1	11	5.662	-1.632	10.100
	7	1	12	0.251	-0.018	-0.382

nearly identical spectral response. Apparently, a difference of only $0.01 \mu\text{m}$ in the wavelength of peak response ($0.71 \mu\text{m}$ versus $0.72 \mu\text{m}$) is enough to cause significant errors due to the very rapidly changing spectral radiance of vegetation targets in this spectral region.

After the spectral simulation of the RBV, MSS and S-192 sensors had been completed, the spatial resolution of the data had to be degraded. The spatial resolution of the multispectral scanner data taken from 10,000-ft altitude was, after digitization, approximately $50 \text{ ft} \times 50 \text{ ft}$ (Section 4.1). This resolution remained after the spectral simulations. Subsequently, the simulation data were smoothed by averaging over blocks five resolution elements square (25 elements per block), to produce one new spatially degraded resolution element. The resultant digital resolution of 250-ft square approximates that expected of the actual sensors. One difference, however, is that each resolution element so created is not significantly contaminated by information from adjacent elements. In real data, such contamination will be present because of limitations in electronic bandwidth, detector time constant, and other factors. Imagery examples of simulated S-192 data are presented in Appendix III.

Perhaps the most significant deficiency in the resultant simulations is that no attempt was made to simulate the actual noise which will appear in the real data. In fact, much of the noise present in the original multispectral scanner data was eliminated as a result of the spectral and spatial averaging accomplished in the simulations. In addition, the path radiance added into the data in performing the extrapolation to space altitudes was accomplished by adding a noise-free signal, thus failing to simulate the increased photon noise produced by the path radiance for a real space sensor. Therefore, the analyses of multispectral recognition capabilities to be discussed in the following sections of this report cannot be interpreted as indications of the absolute capabilities of the various sensors. Rather, they must only be considered indicative of the relative capabilities to be expected.

Another possible deficiency in the simulation involves the statistics of the targets. The simulation technique forced the mean target radiance values to be correctly simulated in each resultant spectral channel. This probably also forced the variances in each channel to be reasonably well simulated, at least for large targets. However, the channel-to-channel spectral covariance, which is determined resolution element by resolution element, may not have survived the simulation without alteration, even though the spectral simulation was done element by element prior to degrading the resolution.

6.2. STANDARD MULTISPECTRAL RECOGNITION EVALUATION

The simulated space data were analyzed by means of a standard likelihood ratio technique which utilizes mean value, variance and spectral covariance derived from training areas in the data known to contain a desired class of target [13]. This technique compares, in an n-dimensional spectral space, each resolution element to be classified against each training distribution in order to determine from which available class the resolution element most likely came. After this decision is reached, the position of the resolution element within the statistical distribution of the most likely class is examined to determine whether the probability is high enough to say that the resolution element really does belong to that class. If not, the resolution element is rejected as not belonging to any of the desired classes. The classification decisions are made independently for each resolution element without any a priori specification as to the probability of occurrence of a given class. The classification decision is also made assuming that no more than one of the desired target classes is actually present in any given resolution element.

Spectral signatures (mean, variance and covariance) were extracted from the original scanner data and from each of the spectrally simulated data sets prior to spatial resolution degradation. This was done in order to preclude problems in defining pure training sets for each target class in the spatially degraded data, and in order to allow the use of the smaller field areas as well as the very large ones. Global signatures were produced by analyzing, for each desired target class, every field which was known to belong to that class, thus accounting for field-to-field variations as well as in-field variations. Only pure fields belonging to a given class were chosen, however (e.g., for barley, only those fields of barley with > 90% ground cover and no significant weed or disease problems). The use of global signatures also assured that problems as a result of row direction or any residual target bidirectional effects not eliminated previously (Section 5.2.1) would be reduced.

The spectral signatures themselves were analyzed prior to multispectral recognition. The results are shown in Tables 10 through 13 for the multispectral scanner, S-192, MSS and RBV signatures, respectively. Shown in these tables is the average pair-wise probability that a member of one target class will be incorrectly classified as belonging to a second. These probabilities are indicative of the statistical independence of pairs of signature distributions. As can be seen,

the statistical independence decreases as the number of sensor spectral channels decreases (from 10 channels for the original scanner data of Table 10 to 3 channels for the RBV data of Table 13). This result is, of course, expected since the degrees of freedom are being reduced. The most significant problems on a pair-wise basis occur when either alfalfa or cut alfalfa (or both) are one of the members of the pairs, with false alarm probabilities for such pairs being at the 0.005% level for the 10 channel scanner data, at the 0.01% level for the S-192, at the 0.02% level for the MSS and at the 0.05% and higher level for the RBV. The only other significantly high probability of false alarm occurs between lettuce and fallow soil for the RBV signatures. Overall, if one takes the average of all values in these tables for each sensor, the resultant average probability is 0.0008 for the multispectral scanner, 0.0016 for the S-192, 0.0026 for the MSS, and 0.0200 for the RBV. Thus, of the space-simulated data, it appears from the signature analysis that the reduction from seven S-192 channels to four MSS channels is not nearly as significant as the reduction from four MSS channels to three RBV channels.

The signatures for the target classes shown in Tables 10 through 13 were used for standard multispectral recognition processing on the three spatially-degraded space simulations and on the non-degraded multispectral scanner data. It was felt that the signatures obtained prior to spatial degradation were valid for recognition after spatial degradation since field-to-field variance within a given class would still be of approximately equal magnitude, while in-field effects on signature variance had been minimized in the first place through selection of pure and uniform field areas for establishing global signatures. A comparison of the total results obtained for the entire flight line of data is shown in Fig. 36. For each of the seven target classes used, the acreage recognized as being of that class by each sensor is shown. Also shown is the acreage rejected as not belonging to any of the seven classes. The test for rejection used a chi-squared criterion designed to reject no more than 0.1% of those data points which actually belonged to the distribution against which they were tested. The criterion accounted for the number of spectral channels in each sensor, and assumed the alternative hypothesis that all data points did not necessarily belong to one of the seven defined classes.

Assuming that the solid bars representing the original scanner data in Fig. 36 are the ground truth (or as near to ground truth as is statistically important to the simulations derived from it), then the results shown are not overwhelmingly conclusive in their relative praise for any particular simulated space sensor. Depending upon the particular target, one or another simulated sensor appears to most closely reproduce the multispectral scanner results. The most significant proportional error occurs for lettuce recognition, particularly by the RBV. Gray maps of the recognition results showed that the RBV tended to classify as lettuce those degraded resolution elements containing a healthy green crop (e.g., barley) together with bare soil (e.g., adjacent bare fields and especially dirt roads). This result is in agreement with the signature analysis of Table 13, which showed some potential problem between lettuce and fallow soil even without

WILLOW RUN LABORATORIES

TABLE 10. AVERAGE PAIR-WISE PROBABILITY OF FALSE ALARM FOR ORIGINAL (10 CHANNEL) SCANNER DATA. (The number is the average of the probabilities that a row target will be incorrectly classified as a column target and vice-versa.)

	<u>Barley</u>	<u>Cut Alfalfa</u>	<u>Alfalfa</u>	<u>Lettuce</u>	<u>Weeds</u>	<u>Bedded and Disced Soil</u>
Cut Alfalfa	0.0014	--	--	--	--	--
Alfalfa	0.0068	0.0053	--	--	--	--
Lettuce	0.0000	0.0000	0.0000	--	--	--
Weeds	0.0000	0.0000	0.0000	0.0000	--	--
Bedded and Disced Soil	0.0000	0.0008	0.0000	0.0000	0.0000	--
Fallow Soil	0.0000	0.0000	0.0000	0.0000	0.0000	0.0020

TABLE 11. AVERAGE PAIR-WISE PROBABILITY OF FALSE ALARM FOR S-192 (7 CHANNELS ONLY) DATA. (The number is the average of the probabilities that a row target will be incorrectly classified as a column target and vice-versa.)

	<u>Barley</u>	<u>Cut Alfalfa</u>	<u>Alfalfa</u>	<u>Lettuce</u>	<u>Weeds</u>	<u>Bedded and Disced Soil</u>
Cut Alfalfa	0.0023	--	--	--	--	--
Alfalfa	0.0128	0.0123	--	--	--	--
Lettuce	0.0000	0.0000	0.0000	--	--	--
Weeds	0.0000	0.0000	0.0000	0.0000	--	--
Bedded and Disced Soil	0.0000	0.0017	0.0000	0.0000	0.0000	--
Fallow Soil	0.0000	0.0001	0.0000	0.0000	0.0000	0.0046

TABLE 12. AVERAGE PAIR-WISE PROBABILITY OF FALSE ALARM FOR MSS (4 CHANNEL) DATA. (The number is the average of the probabilities that a row target will be incorrectly classified as a column target and vice-versa.)

	<u>Barley</u>	<u>Cut Alfalfa</u>	<u>Alfalfa</u>	<u>Lettuce</u>	<u>Weeds</u>	<u>Bedded and Disced Soil</u>
Cut Alfalfa	0.0032	--	--	--	--	--
Alfalfa	0.0209	0.0167	--	--	--	--
Lettuce	0.0000	0.0041	0.0000	--	--	--
Weeds	0.0000	0.0001	0.0002	0.0000	--	--
Bedded and Disced Soil	0.0000	0.0024	0.0000	0.0000	0.0000	--
Fallow Soil	0.0000	0.0003	0.0000	0.0000	0.0000	0.0070

TABLE 13. AVERAGE PAIR-WISE PROBABILITY OF FALSE ALARM FOR RBV (3 CHANNEL) DATA. (The number is the average of the probabilities that a row target will be incorrectly classified as a column target and vice-versa.)

	<u>Barley</u>	<u>Cut Alfalfa</u>	<u>Alfalfa</u>	<u>Lettuce</u>	<u>Weeds</u>	<u>Bedded and Disced Soil</u>
Cut Alfalfa	0.0059	--	--	--	--	--
Alfalfa	0.0522	0.0499	--	--	--	--
Lettuce	0.0000	0.0365	0.0001	--	--	--
Weeds	0.0000	0.0045	0.0017	0.0002	--	--
Bedded and Disced Soil	0.0000	0.0219	0.0003	0.0057	0.0005	--
Fallow Soil	0.0000	0.1832	0.0014	0.0424	0.0030	0.0115

WILLOW RUN LABORATORIES

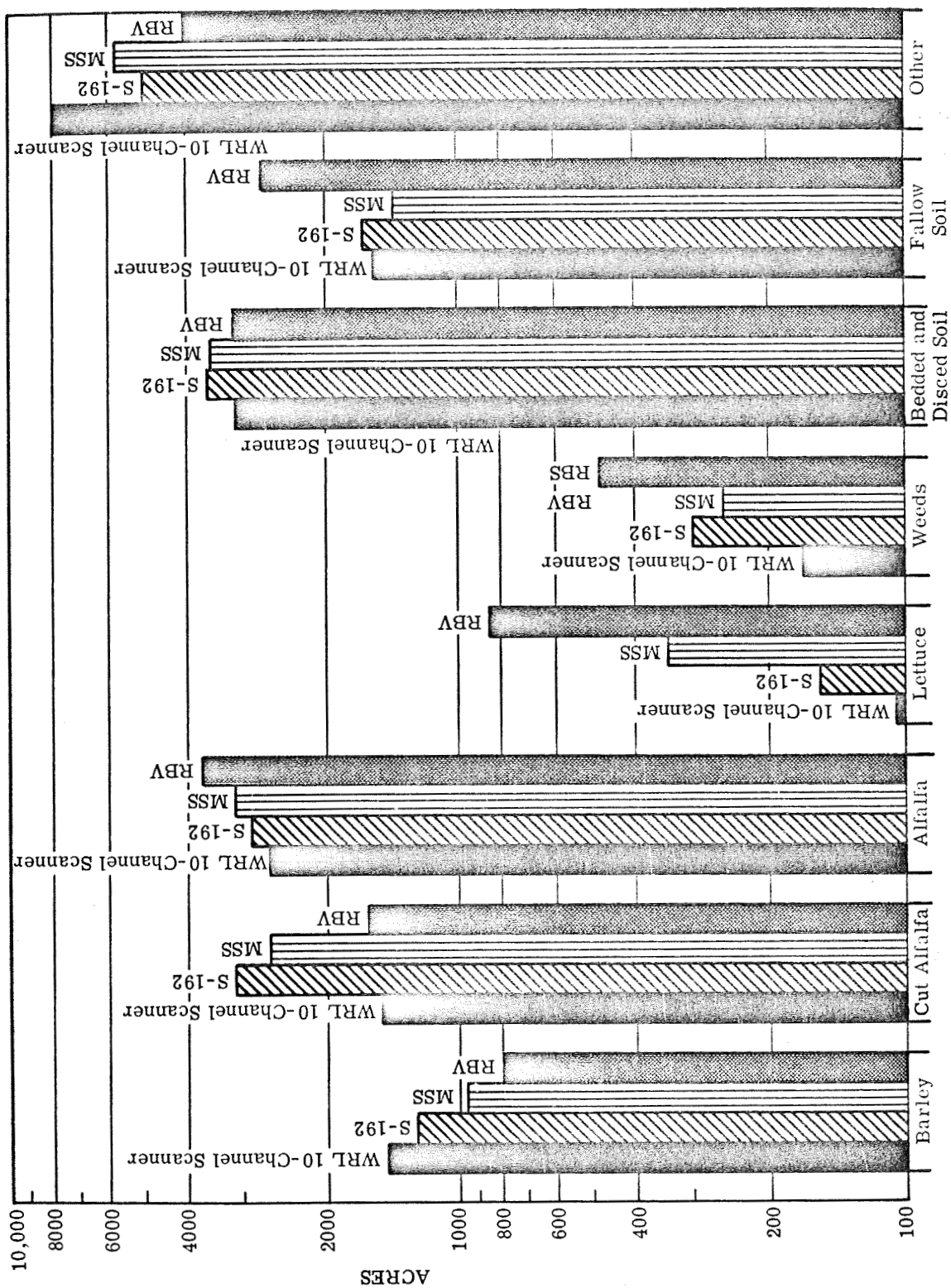


FIGURE 36. STANDARD RECOGNITION RESULTS FOR THE SPACE-SIMULATED SENSOR DATA AND FOR THE ORIGINAL 10-CHANNEL SCANNER DATA. 18,600 acre total.

any vegetation mixed into the soil. On the other hand, the RBV did not produce any significantly unreasonable acreage estimate for cut alfalfa, despite the potential indicated in Table 13.

While the acreage estimates shown in Fig. 36 do not indicate dramatic and consistent trends for any one sensor simulation, a point by point statistical comparison of the recognition results does. The general trend seems to indicate that with a fewer number of spectral bands available more missed detections for a given class occurred. That is a logical result of reducing degrees of freedom. On the other hand, these comparisons also seemed to indicate that the fewer number of spectral bands available, the more false alarms for a given class occurred, and in proportion to the amount of that class present in the scene (and not just in proportion to the amount of the classes from which the false alarms were derived). This result is not logical since a priori expectations were not used in the decisions. The net effect of these two processes was to offset missed detections with false alarms and so maintain approximately similar total acreage estimates for all sensors.

A complete analysis to determine the real significance and source of these results could not be completed in the time available. One possible explanation is that a circuitous logic exists in simulating one data set from another, and then comparing recognition results for the two, even though, on the face of it, one might assume that a degraded simulation should produce poorer recognition results by all measures when compared to the original data. Certainly, the potential for uniformly poorer results was indicated in Tables 10, 11, 12, and 13.

6.3. ANALYSIS OF MIXTURES WITHIN A RESOLUTION ELEMENT

All conventional multispectral recognition approaches are based upon the criterion of classifying a given resolution element as either belonging entirely to one class of a given set, or as belonging to none of the given classes. Such a criterion has the obvious advantage of requiring only a small number of possible choices and tests as to the identity of a resolution element. The number of choices is equal to the number of classes defined plus a rejected class composed of everything else. However, with the advent of remote sensing from space and the associated problem, for many users, of degraded ground resolution, it has become obvious that many resolution elements seen from space will be composed of mixtures of desired target classes. This problem increases as the spatial scale of the targets to be detected decreases.

Recent work at the Willow Run Laboratories has involved itself with the solution of this problem.* The specific approach, often called convex mixtures, assumes that, if several target classes i are present within a resolution element, each in proportion p_i , then the signature mean of the mixture is equal to the weighted sum of the individual signature means, each weighting factor being just equal to p_i . Additionally, the covariance matrix of the mixture is assumed to be resultant from a similar weighting of the individual covariance matrices of the components.

*Contract NAS 9-9784, NASA Manned Spacecraft Center.

Obviously, any small number of component signatures can be so combined as to produce an infinite number of resultant mixture signatures, depending on the particular p_i values chosen. Specific details of the theory of the mixtures analysis and the possible methods for implementation of the mathematics have recently been reported [14]. We shall only indicate that the implementation presently operating and used herein is limited to analyzing for a mixture of no more than $n + 1$ target classes, where n is the number of spectral channels available, and assumes equal covariance for all target classes present. In addition, an alien object criterion is utilized which rejects the entire resolution element if it appears to contain any significant quantity of alien material (i.e., if it appears to contain anything other than the designated target classes). This rejection criterion is analogous in effect, but not equivalent to, the rejection criterion utilized in standard recognition approaches.

It was originally intended that the convex mixtures recognition program be applied to the simulated space data for S-192, MSS and RBV sensors. However, the problems discussed (but not resolved) in the previous section indicated that the results obtained when the simulated data are used would be of questionable validity. Therefore, in order to evaluate the recognition algorithm itself without contaminating the evaluation with any simulation problems, analysis was restricted to the 10-channel multispectral scanner data.

The space-extrapolated 10-channel scanner data were spatially degraded to the same 250-ft square resolution previously described for the simulations. The convex mixtures recognition processing was then accomplished using the spectral signatures extracted from the non-spatially degraded data (previously discussed in Section 6.2). The summary results of the proportion determinations are shown in Table 1 along with the comparable results obtained using the standard multispectral recognition technique (Section 6.2). Since the absolute accuracy of the estimate is in question here, and not just the relative accuracy, Table 1 also contains the actual ground truth results derived from ground observations and field-size measurements on the scanner data (see Section 4.1).

The results shown in Table 1 provide a persuasive argument for the convex mixtures approach. For the classes cut alfalfa plus alfalfa, lettuce, and weeds plus others, the agreement between the mixtures proportions and the ground truth is excellent. For barley, the mixtures proportion is less than the ground truth estimate, but indicative of the fact that the ground truth defines a barley field as being entirely barley, while the mixtures recognition should recognize only that proportion constituting full leaf area coverage by crop, and classify elsewhere any patches of soil showing. Thus, the mixtures recognition indicates an average barley crop cover of 75% of the field. This is not much different from a mean value (based upon field count and not area count) of 80 to 85% estimated on the ground [5]. For the bare soil areas, the convex mixtures recognition produces a higher estimated proportion than indicated by the ground truth. The above argument for barley, in reverse, can account for at least some of this difference. In

WILLOW RUN LABORATORIES

addition, dirt roads and other such non-productive bare soil areas would have been recognized as soil by the mixtures recognition, but classed as other by the ground truth.

The agreement obtained for the convex mixtures recognition is not achieved in the standard recognition results. For the vegetative targets, the estimated proportions seem much too low to be accounted for by the previous leaf-area argument. In addition, the proportion of other (not classified) is significantly greater than indicated by the ground truth. Only the soil proportion can be justified by reasonable arguments other than that the standard recognition approach was not adequate for the job required.

In summary, it would appear that, at least for this data set, the problem of target mixtures within large resolution elements can be very nicely handled by the convex mixtures approach. The results produced are in very good agreement with ground observations, and appear much superior to those produced by the standard recognition technique.

Page intentionally left blank

Appendix I EARTH'S ATMOSPHERE

In the analysis of Earth's surface features from space data, it is often necessary that one consider the perturbing effects of the atmosphere. In this section we shall summarize briefly those atmospheric properties and phenomena which affect electromagnetic radiation in the visible and near-infrared regions of the spectrum.

I.1. SOLAR RADIATION

Almost all of the electromagnetic radiation which arrives at Earth's surface originated from the sun. The spectral characteristic of the radiant energy emitted by the sun approximates that of a 6000°K blackbody with about 99% of the radiation being contained within the spectral band 0.2 to 4.0 μm . Recent high-altitude measurements of the solar radiation by Thekaekara [15] and Arvesen et al. [16] are considered to be among the most reliable estimates of the spectral solar radiation in the visible and near-infrared region. Temporal variations in the solar output can be attributed to geometric and intrinsic changes. There is a 6% total annual variation caused by the varying Earth-sun distance. Intrinsic changes, either from the sun itself or from disturbances in the interplanetary medium are not well known but are generally believed to be small.

I.2. ATMOSPHERIC ATTENUATION

In passing through the atmosphere, electromagnetic radiation is scattered and absorbed by gases and particulates. Besides the major atmospheric gaseous components of molecular nitrogen and oxygen, the gases carbon dioxide, water vapor, ozone, atomic oxygen, atomic nitrogen, carbon monoxide, methane, hydrogen, helium, and nitrogen compounds play an important role in transfer of radiation. The strongest absorption occurs in the ultraviolet (UV) as a result of electronic transitions of molecular and atomic oxygen and nitrogen, and ozone. Another strong region of absorption is the infrared in which there are many bands of absorption due primarily to the vibration and rotation of H_2O , CO_2 , and O_3 molecules. In the visible region from 0.40 to 0.70 μm there is very little absorption by gases. It is in this region however, where multiple scattering takes place and a spatial redistribution of the energy occurs. Since a typical gas scattering center is of the size $\sim 10^{-3}$ μm , whereas the wavelength of visible radiation is ~ 0.5 μm , dipole radiation results and has an intensity which is proportional to the inverse fourth power of the wavelength, i.e.:

$$I_{\text{Rayleigh}} \propto \lambda^{-4} (1 + \cos^2 \theta) \quad (7)$$

where θ is the angle between the initial and final directions of the photon. This type of process is usually referred to as Rayleigh scattering.

Besides the gaseous component, radiation is also affected by the presence of particulates. If the particles have a residence time which is long compared to the period of time required for a measurement, then we can refer to this semipermanent suspension of liquid and solid particles as an aerosol. Aerosols may be categorized as hazes, clouds, mists, fogs, smokes, smogs, and dusts. Their composition can vary, but most continental aerosols are composed of chemical compounds such as NH_4^- , Na^+ , Mg^{++} , SO_4^{--} , NO_3^- , NO_3^- and NO_2^- . Volcanic eruptions, winds, and man-produced aerosols can contain carbon compounds. Much work has been done over the years on aerosols and their size distributions [17]. Generally speaking, one can divide the particles into three size divisions as listed in Table 14. Deirmendjian has classified distributions according to continental and coastal or maritime types [18]. He uses a modified gamma distribution of the form

$$n(r) = ar^\xi \exp(-br^\gamma) \quad (8)$$

where $0 \leq r < \infty$. The parameters a , b , ξ , and γ are not all independent of each other but are related to the mode radius of the particles and their number density. Deirmendjian has developed a variety of models of clouds and hazes by using Eq. (8).

TABLE 14. SIZE DISTRIBUTION OF
AEROSOL PARTICLES

<u>Range</u>	<u>Particle Radius $r(\mu\text{m})$</u>
Aitken Nuclei	0.001 to 0.1
Large Particles	0.1 to 1.0
Giant Particles	≥ 1.0

Based upon this discussion of gases and aerosols, we shall now describe the scattering and absorption properties of Earth's atmosphere. If a beam of radiation propagates through a uniform medium a distance x and undergoes scattering and/or absorption out of that beam, the intensity at distance x from the source is

$$I(x) = I_0 \exp(-\kappa x) \quad (9)$$

In Eq. (9) κ is referred to as the volume extinction coefficient and has the dimensions of reciprocal length. In general, for Earth's atmosphere, κ is not constant with altitude but varies according to the number density of the scattering and absorbing centers. Since the scattering and absorbing processes are independent events we can write

$$\kappa = \alpha + \beta$$

where α is the volume absorption coefficient and β is the volume scattering coefficient. Also, since Rayleigh and aerosol attenuation processes are independent we can write

$$\alpha = \alpha_R + \alpha_A$$

$$\beta = \beta_R + \beta_A$$

$$\kappa = \kappa_R + \kappa_A$$

If we neglect the rather complex relationship of absorption by gases and consider only scattering, the volume extinction coefficient for Rayleigh scattering is given by

$$\kappa_R = N(h)\sigma_s(\text{Rayleigh}) \quad (10)$$

where

$$\sigma_s(\text{Rayleigh}) = \left[\frac{8\pi^3(m^2 - 1)^2}{3\lambda^4 N_s^2} \right] \times \left(\frac{6 + 3\Delta}{6 - 7\Delta} \right)$$

is the Rayleigh scattering cross section for a gas with an index of refraction m , depolarization anisotropy factor Δ , and sea level number density N_s for a standard atmosphere. In Eq. (10) $N(h)$ is the number density as a function of altitude h .

When the wavelength of the radiation is approximately the same as the sizes of the scattering centers, then the instantaneous distribution of charge over the scattering center is a complicated multipole of high order and the consequent scattering is referred to as Mie scattering [19, 20, 21]. Most of the particles composing a haze are typically 0.1 to 1 μm in size and hence for visible and near-infrared radiation the above criterion is fulfilled. Thus, a hazy atmosphere is characterized by considerable scattering. It turns out, however, that the spectral variation for a haze is not a λ^{-4} type as in Rayleigh scattering but a $\lambda^{-1.3}$ type. Therefore, a hazy atmosphere will not possess the deep blue color of a clear sky. A comparison of Rayleigh and aerosol scattering is shown in Fig. 37.

In the case of particulates, a formula for the extinction coefficient similar to Eq. (10) will no longer apply since there is a distribution of particle sizes. Thus, for aerosols we must integrate over the particle sizes, i.e.:

$$\alpha_A = \int_0^\infty \sigma_a(r)N(r)dr \quad \beta_A = \int_0^\infty \sigma_s(r)N(r)dr \quad \kappa_A = \int_0^\infty \sigma_t(r)N(r)dr \quad (11)$$

where $\sigma_a(r)$, $\sigma_s(r)$, and $\sigma_t(r)$ are the absorption, scattering, and total cross sections respectively and $N(r)$ is the particle number density. For comparison, Fig. 37 illustrates the attenuation coefficients for aerosol and Rayleigh scattering.

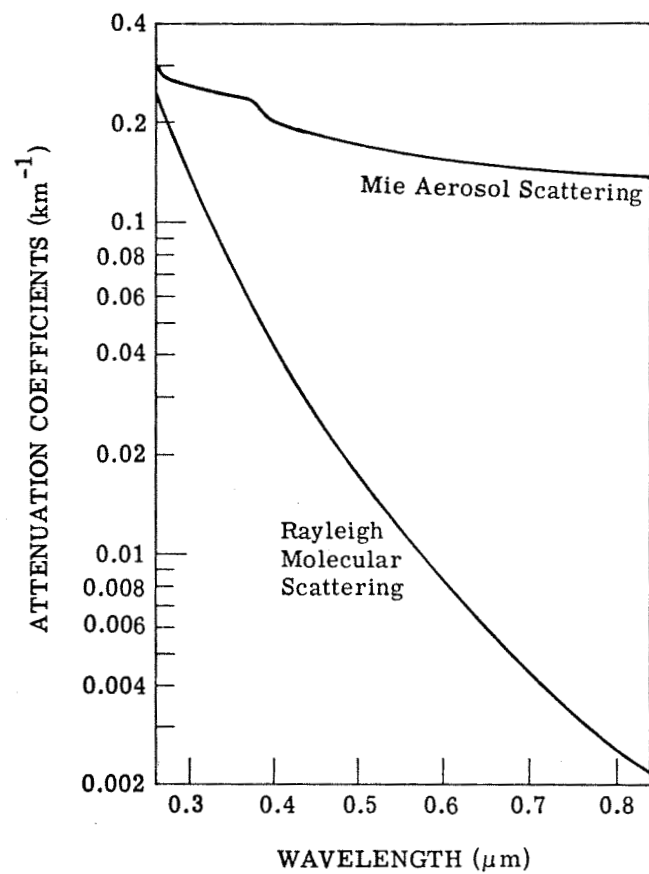


FIGURE 37. WAVELENGTH DEPENDENCE OF THE ATTENUATION COEFFICIENT FOR RAYLEIGH MOLECULAR SCATTERING AND MIE AEROSOL SCATTERING IN THE EARTH'S ATMOSPHERE

Throughout the visible region the major amount of absorption the result of ozone in the so-called Chappuis bands. The peak of absorption occurs near $0.60 \mu\text{m}$ and the total amount of absorption over the visible region is about 2-3%. Compared to other atmospheric absorbers, ozone is not uniformly distributed but lies primarily at an altitude of 23 km and acts essentially as an absorbing layer rather than a homogeneous type of absorption as for other gases. For this reason one can treat this absorption as separable from the scattering phenomenon.

I.3. METEOROLOGY

I.3.1. OPTICAL DEPTH

The optical depth of an atmosphere is a useful quantity which expresses the amount of scattering or absorption which occurs. It can be thought of as the distance which a photon travels measured in units of mean free paths. Thus, it is defined as

$$\tau(h) = \int_h^{\infty} \kappa(z) dz \quad (12)$$

where h is some altitude above sea level and $\kappa(z)$ is the volume extinction coefficient.* The total optical depth of the atmosphere relative to sea level is then

$$\tau_0 = \int_0^{\infty} \kappa(z) dz \quad (13)$$

It is possible to separate the optical depth into two components, that of Rayleigh scattering and that which results from Mie scattering. Let us first consider the Rayleigh optical depth, τ_R . If the terrain altitude is not at sea level, Eq. (13) must be modified as follows:

$$\tau_R(h_0) = \int_{h_0}^{\infty} \kappa_R(z) dz \quad (14)$$

where h_0 is the station altitude and $\kappa_R(z)$ is the Rayleigh volume extinction coefficient. Now, the gaseous component of the atmosphere manifests itself through a static pressure which is found from the hydrostatic balance equation, i.e.

$$P(h_0) = \int_{h_0}^{\infty} \rho(z)g(z) dz \quad (15)$$

*From this point on all quantities are assumed to be spectral values unless otherwise stated. Spectral dependence will not be shown explicitly.

where $\rho(z)$ is the density of the atmosphere at altitude z and $g(z)$ is the acceleration due to gravity. Since $g(z) \approx g_0$, the value at sea level, Eq. (15) becomes

$$P(h_0) \approx g_0 \int_{h_0}^{\infty} \rho(z) dz \quad (16)$$

Now Eq. (14) can be written as

$$\tau_R(h_0) = \int_{h_0}^{\infty} N(z) \sigma(z) dz \quad (17)$$

The number density $N(z)$ is

$$N(z) = \frac{A_0 \rho(z)}{M(z)}$$

where A_0 is Avogadro's number, and $M(z)$ is the mean molecular mass of the atmosphere. Since $M(z) \approx M_0$ and $\sigma(z) \approx \sigma_0$, their corresponding sea level values, then Eq. (13) becomes

$$\tau_R(h_0) = \frac{A_0 \sigma_0}{M_0} \int_{h_0}^{\infty} P(z) dz \quad (18)$$

Therefore, we see that Eqs. (12) and (14) together give

$$\frac{\tau_R(h_0)}{P(h_0)} = \frac{A_0 \sigma_0}{M_0 g_0} \quad (19)$$

Since the right hand side of Eq. (15) is independent of h_0 , the relationship holds for any base altitude, thus

$$\frac{\tau_R(h_0)}{P(h_0)} = \frac{\tau_R(0)}{P(0)}$$

and

$$\tau_R(h_0) = \tau_R(0) \frac{P(h_0)}{P(0)} \quad (20)$$

where $h_0 = 0$ is interpreted as sea level altitude. It should be noted that Eq. (16) also holds if there is a basic or intrinsic change in atmospheric pressure beyond that which results from an

altitude change. Hence, Eq. (16) can be used to find the Rayleigh optical depth corresponding to a given station pressure $P(h_0)$. We shall let $P(0)$ be 1013.250 mbar as a reference. The resulting $\tau_R(0) = \tau_{R0}$ is shown in Fig. 6 for 15°C. Correction for temperature is not usually significant, but, if needed Penndorf's [22] formulas can be used.

I.3.2. TURBIDITY

The turbidity T_u of the atmosphere is a measure of its deviation from a pure Rayleigh atmosphere. There are various definitions of turbidity but the one which we shall use is the Linke [23] turbidity factor, given by

$$\tau_R T_u = \tau_R + \tau_A \quad (21)$$

or

$$T_u = 1 + \frac{\tau_A}{\tau_R} \quad (22)$$

where τ_R is the Rayleigh optical depth and τ_A is the aerosol optical depth.* Thus, if there is no aerosol present in the atmosphere the turbidity has its minimum value of one. Values of turbidity have been determined for the atmosphere over Europe [24] and the United States [25]. It is found that T_u varies from a low value of 1.7 at high altitudes in winter months to a high value of 3.9 at low altitudes in the summertime. As can be seen if one has available the turbidity of the atmosphere, then the aerosol optical depth is determined and the total spectral transmittance of the atmosphere is known. As will be seen in a later section this is an important factor in removing atmospheric effects from space data.

If a measurement of the particle size is made in a given region, and the number density is known, then the aerosol optical depth can be determined using

$$\tau_A(h) = \int_h^\infty \int_0^\infty \sigma_t(r, z) N_p(r, z) dr dz \quad (23)$$

Let us assume that the particulate cross section does not vary with altitude z , and that the number density is given by

$$N_p(r, z) = n_p(z)\psi(r) \quad (24)$$

i.e., the particle size distribution is independent of altitude, an approximation which is usually valid. Hence, the optical depth can be written as

*We are neglecting absorption by water vapor since we consider only the visible and infrared transmission bands.

$$\tau_A(h) = \bar{\sigma}_t \int_h^{\infty} n_p(z) dz \quad (25)$$

where

$$\bar{\sigma}_t = \int_0^{\infty} \sigma_t(r) \psi(r) dr \quad (26)$$

Since aerosol particles have a negligible influence on pressure there exists no pressure correction for the aerosol optical depth as there was for the Rayleigh optical depth. There does seem to be a positive correlation of scattering coefficient with relative humidity [26] but no unique relation or formulation exists. As can be expected, the relationship connecting aerosol optical depth and terrain altitude is not a simple one. If the lateral extent of the terrain is large enough to affect the local weather, then we shall assume that the total aerosol optical depth is independent of terrain altitude.

I.3.3. VISIBILITY

For most practical purposes a measurement of the visibility or visual range defines the basic optical state of the atmosphere. We shall not go into the details of visibility studies but rather we shall simply use Koschmieder's [13] definition for horizontal visual range, i.e.,

$$V(h) = \frac{3.912}{\kappa(h)} \quad (27)$$

where the visual range at altitude h is usually measured in kilometers and the volume extinction coefficient $\kappa(h)$ is given in reciprocal kilometers, and both V and κ are defined at a wavelength of $0.55 \mu m$. The dependence of visual range on extinction coefficient is illustrated in Fig. 38. As a result of thorough analysis of experimental data on atmospheric aerosols, Elterman [28] was able to show that the volume extinction coefficient can be written as

$$\kappa(z) = \kappa_0 e^{-z/H_p} \quad (28)$$

where H_p is a scale height for an aerosol distribution and is a function of visual range. As a result of Eqs. (27) and (28) and the definition of optical depth, the following relation exists:

$$\frac{\tau_A(h)}{\tau_A(0)} = \frac{V(0)}{V(h)} \quad (29)$$

where $\tau_A(0)$ is the optical depth at sea level terrain altitude and $V(0)$ is the corresponding visual range. The dependence of aerosol optical depth on wavelength and visual range is shown in Fig. 7.

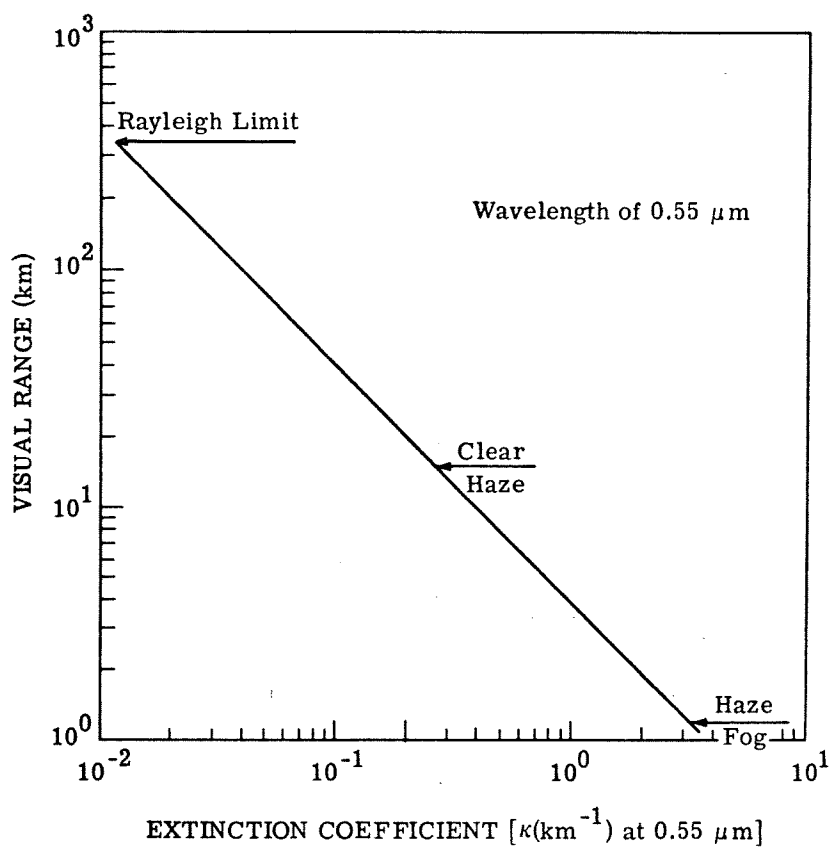


FIGURE 38. VARIATION OF VISUAL RANGE WITH EXTINCTION COEFFICIENT

WILLOW RUN LABORATORIES

Appendix II THE RADIATIVE TRANSFER MODEL

Having defined the optical properties of realistic atmospheres, we must now make use of the theory of radiative transfer to describe the spectral, angular, and geometric distribution of electromagnetic radiation.

II.1. GENERAL DEFINITIONS

Knowledge of the amount of energy flowing per unit area per unit solid angle per unit time per unit wavelength interval for a given polarization state at each point within an atmosphere in terms of the relevant optical parameters constitutes a complete description of the radiation field within that atmosphere. This radiometric quantity is called spectral radiance for a certain state of polarization. We shall average over all polarization states for our work and define spectral radiance without regard to polarization.

The radiation falling upon some flat surface averaged over a hemisphere is called spectral irradiance. It is the amount of energy flowing across a surface per unit area per unit time per unit wavelength interval.

Finally, the spectral transmittance is a dimensionless parameter which indicates the amount of attenuation which a beam of radiation undergoes in passing through a medium.

Let us consider the problem of an atmosphere of infinite lateral extent bounded below by a flat surface and above by a vacuum. Also, allow solar radiation to enter the atmosphere at an angle θ_0 with respect to the outward normal. The total spectral radiance at any point in the atmosphere can then be written as

$$L_T(h, V, \theta_v, \theta_0, \phi) = L_I(V, \theta_v, \theta_0, \phi)T(h, V, \theta_v) + L_P(h, V, \theta_v, \theta_0, \phi) \quad (30)$$

where $L_I(V, \theta_v, \theta_0, \phi)$ is the intrinsic surface radiance, $L_P(h, V, \theta_v, \theta_0, \phi)$ is the path radiance which results from multiple scattering and emission, and $T(h, V, \theta_v)$ is the transmittance. The quantities $h, V, \theta_v, \theta_0, \phi$ are respectively the altitude, visual range, view angle, solar zenith angle, and relative azimuth angle between the solar plane and the view plane.

II.2. RADIATIVE TRANSFER THEORY

The details of radiative transfer theory which have been developed over the past 70 years with all its mathematical intricacies are much too involved to be presented here. However, the basic general ideas can be outlined. There exist three general techniques for determining spectral radiance in a medium: (1) a continuous formulation in which differential or integral equations are solved for the radiation field, (2) a discrete space approach which consists of dividing space into cells and solving difference equations, and (3) a statistical sampling or Monte Carlo solution which depends on the generation of random numbers. Some details of radiative trans-

fer theory and its application to remote sensing problems have previously been described by Turner [29], Malila et al. [30], and Turner et al. [31].

Usually, the major difficulties of solving the equation of radiative transfer involves essentially two functions, the single-scattering albedo and the single-scattering phase function. The former quantity is defined as

$$\omega_0(\tau) = \frac{\beta(\tau)}{\kappa(\tau)} \quad (31)$$

and simply indicates the amount of scattering that takes place. If $\omega_0(\tau) = 0$ there is no scattering and the problem is greatly simplified; if $\omega_0(\tau) = 1$ there is pure scattering, i.e. no absorption, and great mathematical difficulties can occur. The single-scattering phase function, denoted by $p(\nu, \hat{\Omega} \cdot \hat{\Omega}')$ is the fraction of radiation which is scattered from direction $\hat{\Omega}'$ into direction $\hat{\Omega}$. For Rayleigh scattering the phase function is a simple dipole-like distribution but for scattering by aerosol particles the energy is usually distributed heavily in the forward direction, i.e., it is highly anisotropic. For low degrees of anisotropy the solution of the radiative transfer equation is not too difficult. For realistic aerosols which occur in Earth's atmosphere, however, the phase function is extremely anisotropic and certain approximations must be made to solve the equation.

II.3. THE DOUBLE-DELTA FUNCTION APPROXIMATION

The earliest attempts to solve the radiative transfer equation (32, 33) involved breaking the radiation field up into two parts, an upward and downward flux. We consider that we have a modified version of the Schuster-Schwarzschild approximation, called the double delta-function approximation. It has the advantage that it can be applied to hazy atmospheres and produce more realistic results.

We shall consider a homogeneous, isotropic, plane-parallel atmosphere illuminated by direct solar radiation at an angle θ_0 with respect to the outward normal. By homogeneous it is meant that the qualitative scattering and absorption properties are independent of optical depths (i.e. altitude).

$$\omega_0(\tau) = \omega_0, \text{ a constant} \quad (32)$$

and

$$p(\tau, \hat{\Omega} \cdot \hat{\Omega}') = p(\hat{\Omega} \cdot \hat{\Omega}') \quad (33)$$

By isotropic it is meant that the scattering and absorption properties are independent of the initial direction of the photon at an interaction center. The details of solving the integro-differential equation of radiative transfer is beyond the scope of this report. Only the results of the mathematical analysis will be presented here.

The assumptions of the model are the following: (1) there is no diffuse radiation entering Earth's atmosphere from above; (2) the surface background terrain albedo is Lambertian, i.e. perfectly diffuse; (3) there is no absorption within the region where scattering occurs; (4) haze is characterized by visual range or transmittance; (5) no clouds are present; and, (6) the single-scattering phase function can be written as

$$p(\mu, \phi, \mu', \phi') = 4\pi\eta\delta(\mu - \mu')\delta(\mu - \mu') + 4\pi(1 - \eta)\delta(\mu + \mu')\delta(\pi + \phi - \phi') \quad (34)$$

where $\mu = \cos \theta$, $\mu' = \cos \theta'$. The primed quantities refer to the initial set of angles and the unprimed quantities to the final set of angles. The parameter η is the fraction of energy which is scattered into the forward hemisphere and is designated by the approximate relation

$$n = \frac{0.5\tau_R + 0.95\tau_A}{\tau_R + \tau_A} \quad (35)$$

where τ_R is the total Rayleigh optical depth and τ_A is the total aerosol optical depth. Equation (35) indicates that for most aerosol atmospheres with heavy haze where $\tau_A \gg \tau_R$, then $\eta \approx 0.95$ i.e. 95% of the radiation is scattered into the forward direction. If there is very little haze present, $\tau_A \ll \tau_R$ and $\eta \approx 0.5$, i.e. 50% of the radiation is scattered into the forward direction, a result which is exact for pure Rayleigh scattering. Thus, Eq. (35) should hold for all realistic atmospheres from the clearest to those with a heavy haze.

II.4. SIMPLIFIED RESULT FOR SPACE APPLICATIONS

Introducing relation (34) into the radiative transfer equation allows one to solve for the irradiances within the atmosphere [34]. For our purposes, since we are concerned with space data, the total (diffuse plus solar) downward irradiance at the bottom of the atmosphere, E_g is given by

$$E_g(\tau_0) = \frac{\mu_0^2 E_0}{\mu_0 + (1 - \eta)\tau_0} \left[1 + \frac{2\bar{\rho}(1 - \eta)\tau_0}{1 + 2(1 - \eta)(1 - \bar{\rho})\tau_0} \right] \quad (36)$$

where $\bar{\rho}$ is the mean surface (Lambertian) reflectance and E_0 is the extraterrestrial solar irradiance. We can rewrite Eq. (36) as

$$\frac{E_g(\tau_0)}{E_0} = I(\mu_0, \tau_0) \left[1 + J(\tau_0)H(\bar{\rho}, \tau_0) \right] \quad (37)$$

where the functions $I(\mu_0, \tau_0)$, $J(\tau_0)$, and $H(\bar{\rho}, \tau_0)$ are defined as

$$I(\mu_0, \tau_0) = \frac{\mu_0^2}{\mu_0 + (1 - \eta)\tau_0} \quad (38)$$

$$J(\tau_0) = 2(1 - \eta)\tau_0 \quad (39)$$

$$H(\bar{\rho}, \tau_0) = \frac{\bar{\rho}}{1 + 2(1 - \eta)(1 - \bar{\rho})\tau_0} \quad (40)$$

and are all functions of the wavelength, λ . Note

$$\frac{E_g(\tau_0)}{E_0} = \begin{cases} I(\mu_0, \tau_0), \bar{\rho} = 0 \\ I(\mu_0, \tau_0) [1 + J(\tau_0)], \bar{\rho} = 1 \end{cases} \quad (41)$$

The general equation for total spectral radiance of a target t as seen from the top of the atmosphere ($\tau = 0$) is given by

$$L(0, \mu, \phi) = \frac{\rho^t}{\pi} E_g(\tau_0) T_v(0, \mu_v) + L_p(0, \mu_v, \phi) \quad (42)$$

where ρ^t is the effective diffuse reflectance of the target. The total transmittance of the atmosphere is given by

$$T(0, \mu_v) = e^{-\tau_0/\mu_v} \quad (43)$$

and the spectral path radiance is

$$L_p(0, \mu_v, \phi) = E_0 \left[\frac{L_p(0, \mu_v, \phi)}{E_0} \right] \quad (44)$$

where the bracketed function is expressed as

$$\frac{L_p(0, \mu_v, \phi)}{E_0} = F(\mu_v, \phi_v, \mu_0, \phi_0, \tau_0) + G(\mu_v, \phi_v, \mu_0, \phi_0, \tau_0) H(\tau_0, \bar{\rho}) \quad (45)$$

and

$$\begin{aligned} F(\mu_v, \phi_v, \mu_0, \phi_0, \tau_0) = & \frac{1}{4\pi[\mu_0 + (1 - \eta)\tau_0]} \left\{ (1 - \eta)(\tau_0 - \mu_v)[p(\mu_v, \phi_v, \mu_0, \pi + \phi_0) \right. \\ & + p(\mu_v, \phi_v, -\mu_0, \phi_0)] + \mu_0 p(\mu_v, \phi_v, -\mu_0, \phi_0) + (1 - \eta)\mu_v [p(\mu_v, \phi_v, \mu_0, \pi + \phi_0) \\ & + p(\mu_v, \phi_v, -\mu_0, \phi_0)] e^{-\tau_0/\mu_v} - \mu_0 p(\mu_v, \phi_v, -\mu_0, \phi_0) e^{-\tau_0/\mu_v} \left. \right\} \end{aligned} \quad (46)$$

$$G(\mu_v, \phi_v, \mu_0, \phi_0, \tau_0) = \frac{\mu_0^2}{2\pi[\mu_0 + (1 - \eta)\tau_0]} \left\{ 1 + 4\mu_v(1 - \eta) - [1 + 4(1 - \eta)(\tau_0 + \mu_v)] e^{-\tau_0/\mu_v} \right\} \quad (47)$$

The single-scattering phase functions are given by

$$p(\mu_v, \phi_v, \mu_0, \pi + \phi_0) = p \left[\mu_v \mu_0 - \sqrt{(1 - \mu_v^2)(1 - \mu_0^2)} \cos(\phi_v - \phi_0) \right] \quad (48)$$

$$p(\mu_v, \phi_v, \mu_0, \phi_0) = p \left[-\mu_v \mu_0 + \sqrt{(1 - \mu_v^2)(1 - \mu_0^2)} \cos(\phi_v - \phi_0) \right] \quad (49)$$

The values used for the phase functions are those for Deirmendjian's [18] polydisperse continental aerosol distribution and the Rayleigh phase function. A specialized computer program adapted from the radiative transfer model was written to allow the direct determination of the functions I, J, H, T, F, and G in terms of wavelength, view angle, solar zenith angle, relative azimuthal angle, and total spectral transmittance.

The radiative transfer model in its most general form has been used for direct comparison with experimental values of sky radiance and exact sky radiance calculations using Chandrasekhar's [35] theory. Except for very large solar zenith angles ($\theta_0 \gtrsim 86^\circ$) the agreement is excellent [31, 34]. Section 4 describes model validation for the downward looking case.

A simplified technique for graphical computation of the atmospheric parameters discussed above has been formulated. Section 3 describes the procedure and presents the graphs. Also described is a correction for ozone absorption based upon the assumption that most of the significant ozone absorption effects occur above the altitude where scattering becomes of negligible significance.

Appendix III
SIMULATED S-192 MULTISPECTRAL SCANNER IMAGERY

Section 6.1 described the methodology by which multispectral digital data were simulated for various space sensors by use of the M-5 multispectral scanner data of Imperial Valley. These simulations included the first seven spectral channels of the S-192 sensor.

Hardcopy imagery of the S-192 sensor simulations were prepared from the digital tapes by the Earth Observation Divisions' Data Analysis Stations at NASA/Manned Spacecraft Center. This imagery is presented as Fig. 39. As discussed in Section 6.1, these simulations are quite good in terms of reproducing, for each spectral channel, the appropriate average band radiance level for the various targets evaluated. In addition, the simulated resolution of 250 ft square approximates quite closely the nominal resolution capability of the S-192 sensor.

Certain limitations or deficiencies in the simulations were also discussed in Section 6. For the simulated imagery of Fig. 39, the important deficiencies concern resolution and noise. Because the simulated 250 ft square resolution element was built up from much smaller (50 ft square) elements, the Modulation Transfer Function (MTF) for this simulated element is quite high, probably about 0.9. Conversely, the actual S-192 sensor (unit 2) exhibits an MTF between 0.26 and 0.41 for such a resolution element [12].

System detector or photon noise sources are significantly suppressed in the simulated S-192 imagery. This results partly from the spectral and spatial averaging involved in producing the simulation. Additionally, however, the atmospheric path radiance added to the data to simulate space-acquired data was a pure noise-free level. In any real sensor, a higher path radiance input leads to higher photon noise, while the associated decrease in path transmittance leads to attenuated signal differences between targets, the net result being a reduced signal to noise ratio for discriminating between targets. This deficiency in simulating the noise consequences of the total atmosphere on the data is greatest for the shortest wavelength channels.

Figure 40 is a ground truth map of the Imperial Valley area for which the S-192 simulations were made. Tables 15 and 16 identify the nature and state of the numbered fields at the time the data were acquired. Figure 40 and the tables were extracted from reference [5].

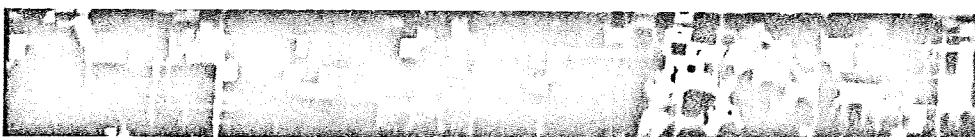
WILLOW RUN LABORATORIES

Data Not Available

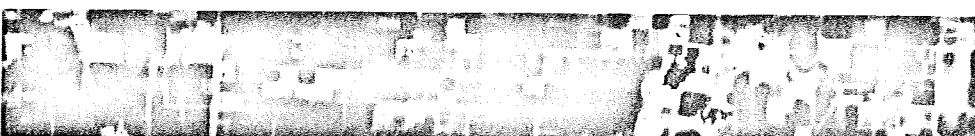
(a) Channel 1



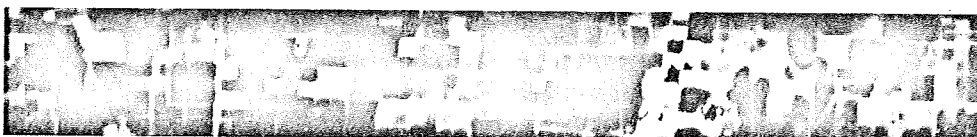
(b) Channel 2



(c) Channel 3



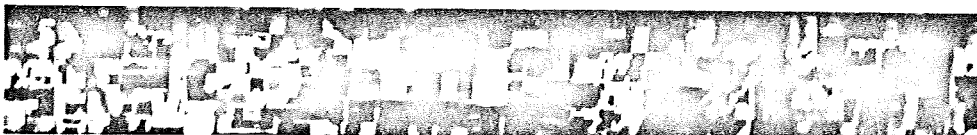
(d) Channel 4



(e) Channel 5

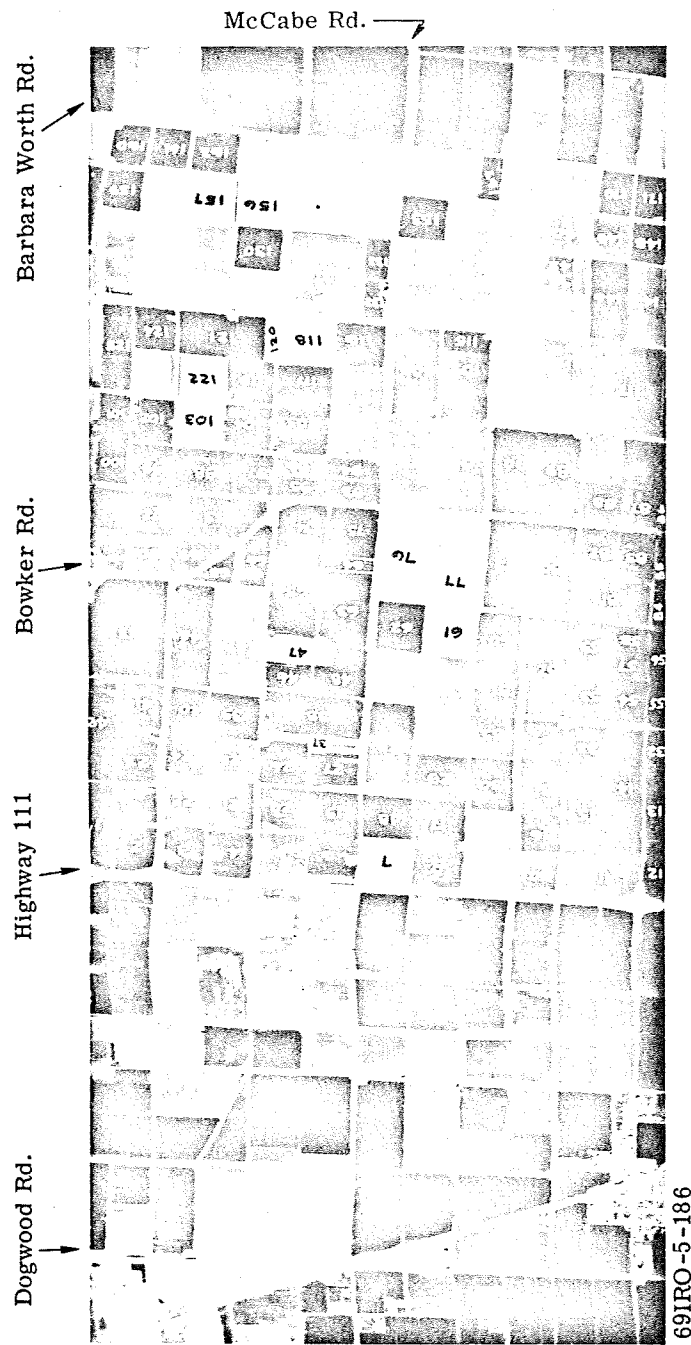


(f) Channel 6



(g) Channel 7

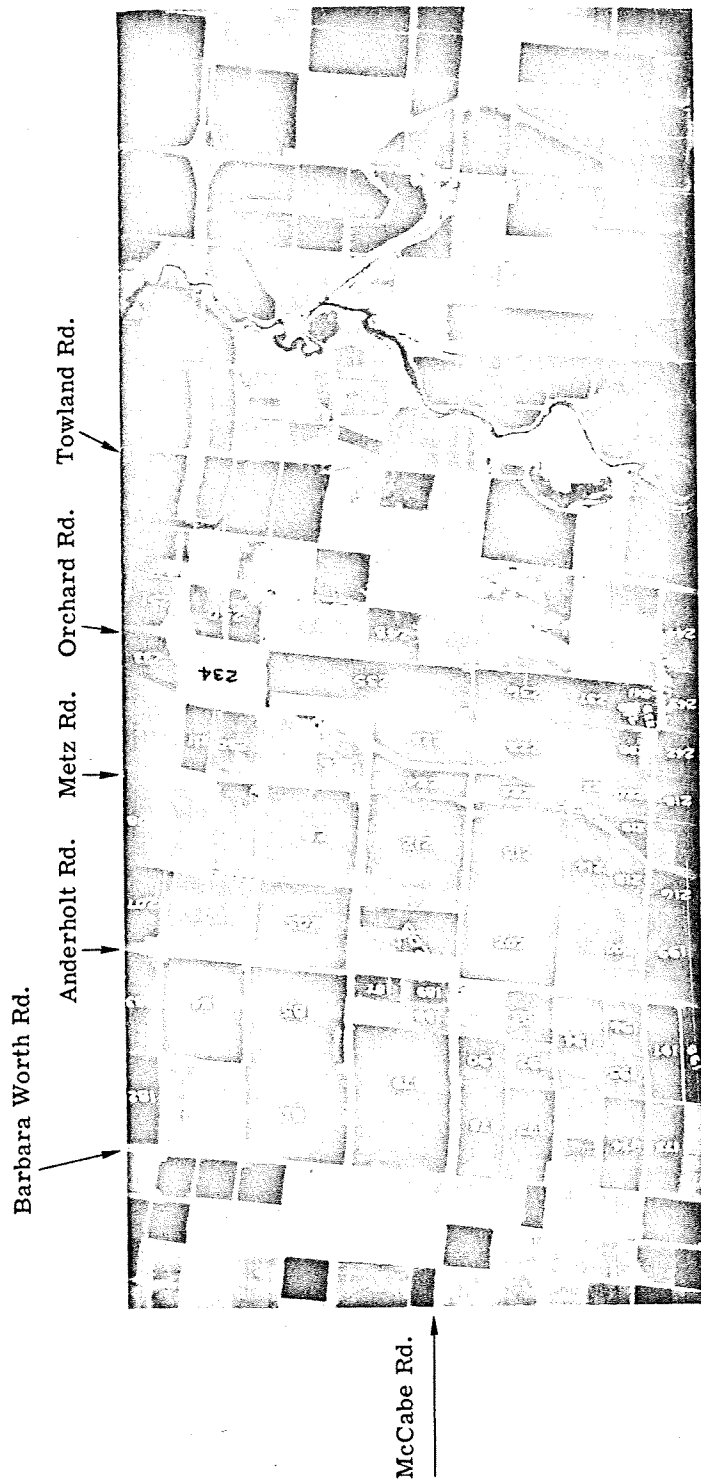
FIGURE 39. SIMULATED S-192 MULTISPECTRAL SCANNER IMAGERY. Spectral and spatial simulation accomplished by means of M-5 multispectral scanner data acquired over Imperial Valley on 12 March 1969. Each image represents an area approximately 2 mi wide and 14 mi long.



(a) Western Section

Scanner Imagery Line No. 15D, McCabe Road
 Simulated Type 3400 Film with 25A Filter
 Altitude 10,000, Ground Track Heading 90°
 Date 12 Mar 69, Time 1006

FIGURE 40. IMPERIAL VALLEY TEST AREA



69IRO-5-187

(b) Eastern Section

Scanner Imagery Line No. 15D, McCabe Road
 Simulated Type 3400 Film with 25A Filter
 Altitude 10,000, Ground Track Heading 90°
 Date 12 Mar 69, Time 1006

FIGURE 40. IMPERIAL VALLEY TEST AREA (Continued)

WILLOW RUN LABORATORIES

TABLE 15a. IMPERIAL VALLEY GROUND TRUTH
Line 15D (McCabe Rd); Fields 1-50

Field No.	Field Code	Row Dir.	Est. Ave. Crop Height (in.)	Est. Ave. Ground Cover (%)	Field Treatments Prior to and During Flights, and Other Ground Observations
1	A&R	NS	3-4	90	Recently cut
2	B	NS	30-36	60	Large patches of bare soil in E portion of field
3	R	NS	3-8	70	
4	R	NS	3-8	80	
5	A&B	EW	4-6	70	
6	A	NS	6-12	60	30% weed cover
7	A&B	EW	6-8	90	Recently pastured
8	A&B	NS	10-34	80	Pastured
9	A&B	NS	2-6	90	Pastured
10	A	NS	2-4	100	Recently cut
11	CB	NS	6-12	60	10% weed cover; field partially cut
12	A	NS	8-10	90	
13	L	NS	4-6	80	
14	A	NS	2-6	90	
15	B	NS	24-30	90	
16	B	NS	2-6	90	Recently cut
17	A	NS	12-16	100	
18	B	NS	20-30	100	Heading stage
19	B	NS	12-20	80	20% weed cover; pastured; large portions of bare soil in S portion of field
20	R	NS	10-16	80	
21	R	NS	2-6	90	
22	R	EW	2-4	90	Pastured; patches of bare soil with white salt deposits
23	R	NS	4-8	80	Scattered areas of salt deposits and weeds at E end
24	A	NS	2-8	70	10% weed cover; pastured
25	R	NS	2-6	80	
26	B	EW	20-28	90	
27	B	NS	20-24	60	Large patches of bare soil in E portion of field
28	A	EW	8-16	90	Irregular cover
29	A	EW	15-22	90	
30	A	NS	3-12	90	Pastured
31	B	NS	2-6	90	Recently cut
32	B	NS	2-4	100	Recently cut; yellowish-green stubble
33	A	NS	4-10	90	
34	B	EW	18-24	90	
35	A	NS	16-18	90	Pastured
36	A	EW	2-4	80	Recently cut; yellowish-green stubble
37	SFT				
38	B	NS	18-24	85	Large patches of bare soil in N portion of field
39	SB	EW	20-24	90	10% weeds
40	SB	NS	18-24	80	20% weed cover
41	R	EW	4-10	70	
42	R	NS	4-6	80	
43	SB		18-24	90	
44	PS		10-16	90	15% alfalfa and 75% weeds
45	BS				Bedded for cotton
46	B	NS	18-24	90	
47	SFT		20-60		Weeds
48	B	NS	18-24	90	
49	L	NS	6-8	60	Yellow mottling
50	L	NS	6-8	40	40% weed cover

WILLOW RUN LABORATORIES

TABLE 15b. IMPERIAL VALLEY GROUND TRUTH
Line 15D (McCabe Rd); Fields 53-103

Field No.	Field Code	Row Dir.	Est. Ave. Crop Height (in.)	Est. Ave. Ground Cover (%)	Field Treatments Prior to and During Flights, and Other Ground Observations
51	A	NS	18-24	90	
52	B	EW	24-30	100	
53	B	NS	10-16	90	
54	B	NS	18-24	90	
55	SB		10-12	100	Yellow mottling
56	SB	NS	12-18	100	Yellow mottling
57	B		12-14	100	
58	B	NS	8-10	70	
59	B	NS	8-10	70	
60	B	NS	24-36	100	
61	SB				
62	B	NS	20-24	90	
63	SB	NS	15-18	90	
64	B		12-18	80	
65	A	NS	3-6	70	Recently cut
66	SB	EW	18-24	100	
67	ON	EW	20-30	60	
68	CR	EW	10-12	80	
69	R	EW	2-4	70	
70	A	EW	4-8	60	20% weed cover
71	A	NS	4-12	80	
72	A	EW	3-8	90	30% weed cover
73	A	EW	4-6	80	
74	SB	NS	14-18	90	
75	B	NS	18-24	95	
76	BS				
77	BS				
78	BS	NS			Bedded for cotton
79	B	NS	24-30	100	
80	B	NS	24-30	100	
81	B	NS	6-10	70	
82	B	EW	2-8	80	
83	B	NS	12-14	90	
84	SB	NS	10-12	100	
85	R	EW			Pastured
86	SB		12-14	90	
87	B		24-36	70	
88	A&B	NS	3-10	80	E portion of field is barley; pastured
89	B	EW	24-30	100	
90	B	EW	24-30	90	
91	R	NS	3-6	90	
92	R	NS	4-6	80	
93	I				80% weed cover
94	I				80% weed cover
95	I				80% weed cover
96	I				80% weed cover
97	SF		24-36	70	
98	A&R	NS		60	Large patches of bare soil in SE portion of field
99	A	EW	10-12	100	
100	B	NS	24-30	100	
101	B	NS	24-30	100	
102	A	NS	3-4	80	Recently cut
103	BS	NS			Bedded for cotton

WILLOW RUN LABORATORIES

TABLE 15c. IMPERIAL VALLEY GROUND TRUTH
Line 15D (McCabe Rd); Fields 104-155

Field No.	Field Code	Row Dir.	Est. Ave. Crop Height (in.)	Est. Ave. Ground Cover (%)	Field Treatments Prior to and During Flights, and Other Ground Observations
104	A	NS	10-12	80	
105	A	NS	10-12	70	
106	SF	NS	24-30	100	
107	SF	NS	24-30	100	
108	R	NS	3-6	80	
109	R	NS	3-5	80	Pastured
110	L	NS			Recently disked
111	L				Recently disked
112	BS	NS			Worked and borders up
113	L				Recently disked
114	BS	EW			Bedded for cotton
115	B	NS	6-10	90	
116	B	EW	18-24	80	
117	A	EW	10-12	80	
118	BS	EW			Bedded
119	A	NS	10-12	90	
120	BS	EW			Bedded
121	B	EW	24-36	100	
122	BS	EW			Bedded for cotton
123	BS				Recently plowed
124	A	EW		100	Recently cut
125	A&B	NS	3-5	70	
126	ON	NS	12-18	70	
127	BS	EW			Bedded for melons
128	BS	EW			Bedded for melons
129	L	NS	4-6	30	
130	B	NS	24-30	100	
131	A	NS	3-4	60	Recently cut
132	A	EW	6-8	80	
133	A	EW	6-8	80	
134	A	NS	3-6	70	
135	BS				Bedded for cotton
136	A	NS	3-6	70	
137	BS	NS			Bedded for cotton
138	BS	EW			Bedded for melons
139	BS				
140	BS				
141	BS				
142	BS				
143	BS				
144	BS				
145	BS				
146	SB	NS	18-24	80	40% weed cover
147	CB	NS			
148	A		10-36	90	Weeds; pastured
149	A	NS	3-18	90	Weedy
150	A				Weedy
151	BS	NS			Bedded for cotton
152	L	NS	5-10	60	50% weed cover
153	SB	NS	15-18	100	
154	L	NS	4-6	50	
155	L	NS	4-6	70	

WILLOW RUN LABORATORIES

TABLE 15d. IMPERIAL VALLEY GROUND TRUTH
Line 15D (McCabe Rd); Fields 156-207

Field No.	Field Code	Row Dir.	Est. Ave. Crop Height (in.)	Est. Ave. Ground Cover (%)	Field Treatments Prior to and During Flights, and Other Ground Observations
156	BS	EW			Bedded for melons
157	BS	EW			Bedded for melons
158	BS	NS			Recently plowed
159	A	NS	8-16	95	
160	A	NS	8-16	90	
161	A	NS	10-12	100	
162	A	NS	10-12	100	
163	BS	EW			Bedded for melons
164	BS				Recently plowed
165	ON	NS	3-5	30	
166	BS	EW			Bedded for melons
167	?				
168	BS	NS			Bedded for cotton
169	BS	EW			Bedded for cotton
170	SB	EW	15-18	80	30% weed cover
171	A	NS	10-12	100	
172	L	NS			Recently disked
173	L	NS			Recently disked
174	B	NS	24-30	100	
175	ON	NS	12-18	60	
176	BS	EW			Bedded for cotton
177	A	NS		100	
178	SB	EW	15-20	90	
179	SB	NS	12-20	90	Yellow mottling
180	A	NS	6-8	80	
181	BS	EW			Bedded for melons
182	R	NS	3-6	80	
183	L	NS	4-6	70	
184	A	NS	12-24	100	
185	A	EW	10-14	90	
186	BS	NS			Bedded
187	B	NS		60	
188	A&B	EW	2-4	60	Pastured; weedy
189	A&B	EW	2-4	60	Pastured; weedy
190	SB	EW	15-25	100	
191	L	NS	6-8	70	
192	A	NS	2-4	70	Recently cut
193	OR				Orchard
194	A	NS		80	Cut and baled
195	A	NS	2-4	70	
196	A	NS	2-4	80	
197	B	NS	24-30	100	
198	B	NS	30-36	100	
199	A	NS		100	Recently cut
200	A	EW	2-4	60	W 1/2 of field recently plowed
201	BS	NS			Bedded for cotton
202	B	NS	24-30	100	
203	PS				Sheep pasture
204	BS	NS			Bedded for cotton
205	A	NS	2-4	70	Recently cut
206	BS	EW			Recently plowed
207	B	EW	20-28	100	

WILLOW RUN LABORATORIES

TABLE 15e. IMPERIAL VALLEY GROUND TRUTH
Line 15D (McCabe Rd); Fields 208-251

Field No.	Field Code	Row Dir.	Est. Ave. Crop Height (in.)	Est. Ave. Ground Cover (%)	Field Treatments Prior to and During Flights, and Other Ground Observations
208	BS	NS			Bedded
209	BS				Recently plowed
210	A	EW		60	Recently cut
211	ON	NE&NS	14-18	60	E portion of field in NE-SW rows
212	A	EW	6-8	70	
213	B	NS	24-28	90	
214	SB	EW	15-18	70	Yellow mottling
215	BS	EW			Bedded for cotton
216	A	EW	8-10	100	
217	BS				Borders worked up
218	B	EW	12-14	100	
219	?				
220	?				
221	SB	EW	18-26	90	
222	SB	NS	15-18	90	
223	A	EW	6-10	90	
224	SB	NS	15-18	90	Yellow mottling
225	A	EW	10-12	100	
226	ON	SE	12-18	60	
227	BS	NS			Bedded for cotton
228	L	NE	6-8	60	Weedy
229	BS				
230	A	EW	3-5	70	Pastured
231	A	EW	12-18	100	30% weed cover
232	BS	EW			Bedded for melons
233	L	NS	8-10	100	Harvesting 3/12
234	BS	EW			Bedded for melons
235	B	EW	30-36	90	
236	A	NS	12-24	100	
237	B	EW	24-36	100	Yellow mottling
238	?				
239	OR				Orchard
240	?				
241	?				
242	?				
243	A	EW	12-14	90	
244	?				
245	BS				Boarders worked up
246	CR	NS	4-6	50	
247	BS	EW			Bedded and irrigated
248	?				
249	BS	EW			Bedded for melons
250	CR	NS	4-6	60	
251	CR	NS	4-6	60	

TABLE 16. FIELD KEY

<u>Field Code</u>		<u>Field Type</u>
A	=	Alfalfa
B	=	Barley
A & B	=	Alfalfa and barley
A & O	=	Alfalfa and oats
A & R	=	Alfalfa and rye
BS	=	Bare soil
CB	=	Cabbage
CR	=	Carrots
FL	=	Feed lot
FS	=	Farmstead
G	=	Cotton gin
GS	=	Grain stubble
I	=	Idle
L	=	Lettuce
ON	=	Onions
OR	=	Orchard
P	=	Pond
PS	=	Pasture
R	=	Rye
R & B	=	Rye and barley
SB	=	Sugar beets
SF	=	Safflower
SFT	=	Salt flat
FX	=	Flax

WILLOW RUN LABORATORIES

REFERENCES

1. R. N. Colwell et al., Monitoring Earth Resources from Aircraft and Spacecraft, Report No. SP-275, Scientific and Technical Information Office, NASA, Washington, D.C., 1971.
2. P. D. Lowman, Jr., Apollo 9 Multispectral Photography: Geologic Analysis, Report No. X-644-69-423, Goddard Space Flight Center, NASA, Greenbelt, 1969.
3. V. Leeman et al., The NASA Earth Resources Spectral Information Systems: A Data Compilation, Report No. 31650-24-T, Willow Run Laboratories of the Institute of Science and Technology, The University of Michigan, Ann Arbor, May 1971.
4. P. G. Hasell and L. M. Larsen, Calibration of an Airborne Multispectral Optical Sensor, Report No. 6400-137-T, Willow Run Laboratories of the Institute of Science and Technology, The University of Michigan, Ann Arbor, October 1968.
5. N. Spansail, Imperial Valley Ground Truth for Apollo 9 Overflight of March 1969, Report No. 2264-7-X, Willow Run Laboratories of the Institute of Science and Technology, The University of Michigan, Ann Arbor, May 1969.
6. T. D. Glaze et al., Flight Film Control Friskets—Apollo 9, Technical Note DTN-69-4, Data Corporation, Dayton, July 1969.
7. P. B. Keenan et al., Interim Post-Flight Calibration Report on Apollo 9 Multiband Photography Experiment SO-65, Technical Memorandum 2, Optical Sciences Center, University of Arizona, Tucson, 15 June 1970.
8. P. B. Keenan and P. N. Slater, Preliminary Post-Flight Calibration Report on Apollo 9 Multiband Photography Experiment SO-65, Technical Memorandum 1, Optical Sciences Center, University of Arizona, Tucson, September 1969.
9. N. T. Lamar, Photographic Technology Laboratory, Manned Spacecraft Center, NASA, Houston, Personal Communication to R. Horvath, Willow Run Laboratories of the Institute of Science and Technology, The University of Michigan, Ann Arbor, 28 April 1972.
10. N. M. Short and N. H. MacLeod, Analysis of Multispectral Images Simulating ERTS Observations, Report No. X-430-72-118, Goddard Space Flight Center, Greenbelt, April 1972.
11. Acceptance Data Package for S192 Multispectral Scanner NAS 9-11196, Unit I, Volume IA, Honeywell Radiation Center, Lexington, 1971.
12. Summary Data Test Procedures—S192 Multispectral Scanner No. 2, Honeywell Radiation Center, Lexington, 19 May 1972.
13. R. F. Nalepka, Investigation of Multispectral Discrimination Techniques, Report No. 2764-12-F, Willow Run Laboratories of the Institute of Science and Technology, The University of Michigan, Ann Arbor, January 1970.
14. R. F. Nalepka et al., Stimating Proportions of Objects from Multispectral Data, Report No. 31650-73-T, Willow Run Laboratories of the Institute of Science and Technology, The University of Michigan, Ann Arbor, March 1972.
15. M. P. Thekaekara, "Evaluating the Light from the Sun," Optical Spectra, March 1972.
16. J. C. Arvesen, R. N. Griffin, Jr., and B. D. Person, Jr., "Determination of Extraterrestrial Solar Spectral Irradiance from a Research Aircraft," Appl. Opt., Vol. 8, No. 11, November 1969.

17. C. E. Junge, Air Chemistry and Radioactivity, Academic Press, New York, 1963.
18. D. Deirmendjian, Electromagnetic Scattering on Spherical Polydispersions, American Elsevier Publishing Company, New York, 1969.
19. M. Kerker, The Scattering of Light and Other Electromagnetic Radiation, Academic Press, New York, 1969.
20. H. C. van de Hulst, Light Scattering by Small Particles, Wiley Publishing Company, New York, 1957.
21. R. O. Gumprecht and C. M. Sliepcevich, Light-Scattering Functions for Spherical Particles, Engineering Research Institute, The University of Michigan, Ann Arbor, 1951.
22. R. Penndorf, "Tables of the Refraction Index for Standard Air and the Rayleigh Scattering Coefficient for the Spectral Region Between 0.2 and 20.0 μm and Their Applications to Atmospheric Optics," J. Opt. Soc. Am., Vol. 47, No. 2, 1957.
23. P. N. Tverskoi, Physics of the Atmosphere, Trans. by A. Sen and R. N. Sen, Ed. by E. S. Selezneva, Israel Program for Scientific Translations, Jerusalem, 1965, NASA TT F-288, TT 65-50114, Washington, 1965.
24. N. Robinson, Solar Radiation, Elsevier Publishing Company, New York, 1966.
25. F. E. Volz, "Some Results of Turbidity Networks," Tellus, XXI, No. 5, 1969.
26. G. V. Rozenberg, "Optical Investigations of Atmospheric Aerosols," Soviet Uspekhi, Vol. 11, No. 3, 1968.
27. W. E. K. Middleton, Vision Through the Atmosphere, University of Toronto Press, Toronto, 1952.
28. L. Elterman, Vertical Attenuation Model with Eight Surface Meteorological Ranges, 2 to 13 Kilometers, Report No. AFCRL-70-0200, Air Force Cambridge Research Laboratories, Cambridge, March 1970.
29. R. E. Turner, Atmospheric Models (Scattering), Willow Run Laboratories of the Institute of Science and Technology, The University of Michigan, Engineering Summer Conference Notes, Advance Infrared Technology, July 1972.
30. W. A. Malila, R. B. Crane, C. A. Omarzu and R. E. Turner, Studies of Spectral Discrimination, Report No. 31650-22-T, Willow Run Laboratories of the Institute of Science and Technology, The University of Michigan, Ann Arbor, 1971.
31. R. E. Turner, W. A. Malila and R. F. Nalepka, Importance of Atmospheric Scattering in Remote Sensing, Proceedings of the Seventh International Symposium on Remote Sensing of the Environment, Report No. 10259-1-X, Willow Run Laboratories of the Institute of Science and Technology, The University of Michigan, Ann Arbor, 1971.
32. A. Schuster, Radiation Through a Foggy Atmosphere, Astrophys. J., Vol. 21, No. 1, 1905.
33. K. Schwarzschild, Gottinger Nachrichten, Vol. 41, 1906.
34. W. A. Malila, R. B. Crane and R. E. Turner, Information Extraction Techniques for Multispectral Scanner Data, Report No. 31650-74-T, Willow Run Laboratories of the Institute of Science and Technology, The University of Michigan, Ann Arbor, 1972.
35. S. Chandrasekhar, Radiative Transfer, Dover Publications, New York, 1960.

WILLOW RUN LABORATORIES

DISTRIBUTION LIST

<p>NASA/Manned Spacecraft Center Earth Observations Division Houston, Texas 77058</p> <p>ATTN: Mr. Larry B. York/TF (4) ATTN: Mr. Robert MacDonald (1) ATTN: Mr. John D. Overton/TF4 (1) ATTN: Mr. Dallas E. Evans/TF (1) ATTN: Dr. A. Potter/TF3 (1) ATTN: Mr. Brian Erb/TF2 (1) ATTN: Mr. Edward O. Zeitler/TF53 (12) Chief Earth Resources Research Data Facility ATTN: Mr. A. H. Watkins/TF (1)</p> <p>NASA/Manned Spacecraft Center Space Sciences Procurement Division Houston, Texas 77058</p> <p>ATTN: Mr. R. F. LaMere BB321 (S55) (1)</p> <p>NASA/Manned Spacecraft Center Computation and Flight Support Houston, Texas 77058</p> <p>ATTN: Mr. John Frere/FA12 (1) ATTN: Mr. Eugene Davis/FA (1)</p> <p>Chief, Earth Resources Survey Program NASA Headquarters Washington, D. C. 20242</p> <p>ATTN: Dr. A. Park (1)</p> <p>U. S. Department of Agriculture Agricultural Research Service Washington, D. C. 20242</p> <p>ATTN: Dr. Robert Miller (1)</p> <p>U. S. Department of Agriculture Soil and Water Conservation Research Division P. O. Box 267 Weslaco, Texas 78596</p> <p>ATTN: Dr. Craig Wiegand (1)</p> <p>U. S. Department of Interior Geological Survey Washington, D. C. 20242</p> <p>ATTN: Dr. Arch C. Gerlach (1)</p> <p>U. S. Department of Interior Geological Survey 801 19th Street, N. W., Room 1032 Washington, D. C. 20242</p> <p>ATTN: Dr. Raymond W. Fary (1)</p> <p>U. S. Department of Interior, Geological Survey 801 19th Street, N. W. Washington, D. C. 20242</p> <p>ATTN: Mr. Charles Withington (1)</p> <p>U. S. Department of Interior Geological Survey 801 19th Street, N. W. Washington, D. C. 20242</p> <p>ATTN: Mr. M. Deutsch (1)</p> <p>U. S. Department of Interior Geological Survey 801 19th Street, N. W., Room 1030 Washington, D. C. 20242</p> <p>ATTN: Dr. Jules D. Friedman (1)</p> <p>U. S. Department of Interior Geological Survey, Federal Center Denver, Colorado 80225</p> <p>ATTN: Dr. A. Campbell/Dr. Harry W. Smedes (1)</p> <p>U. S. Department of Interior Geological Survey, Water Resources Division Room 730, 51 S. W. First Avenue Miami, Florida 33130</p> <p>ATTN: Mr. Aaron L. Higer/Mr. Milton Kolipinski (1)</p> <p>University of California School of Forestry Berkeley, California 94720</p> <p>ATTN: Dr. Robert Colwell (1)</p>	<p>Oregon State University School of Agriculture Range Management Corvallis, Oregon 97331</p> <p>ATTN: Dr. Charles E. Poulton (1)</p> <p>U. S. Geological Survey Branch of Theoretical Geophysics 2221 Jefferson Davis Highway Arlington, Virginia 22202</p> <p>ATTN: Dr. William Hemphill (1)</p> <p>U. S. Geological Survey Water Resources Division, Code 4032 0001 Washington, D. C. 20242</p> <p>ATTN: Mr. C. J. Robinove (1)</p> <p>Chief of Technical Support Environmental Protection Agency Western Environmental Research Laboratories P. O. Box 15027 Las Vegas, Nevada 89114</p> <p>ATTN: Mr. Leslie Dunn (1)</p> <p>NASA/Langley Research Mail Stop 470 Hampton, Virginia 23365</p> <p>ATTN: Mr. William Howle (1)</p> <p>U. S. Geological Survey Branch of Regional Geophysics Denver Federal Center, Building 25 Denver, Colorado 80225</p> <p>ATTN: Mr. Kenneth Watson (1)</p> <p>NAVOCEANO, Code 7001 Naval Research Laboratory Washington, D. C. 20390</p> <p>ATTN: Mr. J. W. Sherman, III (1)</p> <p>Agricultural Stabilization and Conservation Service Department of Agriculture Washington, D. C. 20242</p> <p>ATTN: Mr. J. Clifton (1)</p> <p>Pacific Southwest Forest and Range Experiment Station U. S. Forest Service P. O. Box 245 Berkeley, California 94701</p> <p>ATTN: Mr. R. C. Heller/Dr. P. Weber (1)</p> <p>Director, Remote Sensing Institute South Dakota State University Agriculture Engineering Building Brooks, South Dakota 57006</p> <p>ATTN: Mr. Victor I. Myers (1)</p> <p>U. S. Department of Interior Fish and Wildlife Service Bureau of Sport Fisheries and Wildlife Northern Prairie Wildlife Research Center Jamestown, North Dakota 58401</p> <p>ATTN: Mr. Harvey K. Nelson (1)</p> <p>U. S. Department of Agriculture Forest Service 240 W. Prospect Street Fort Collins, Colorado 80521</p> <p>ATTN: Dr. Richard Driscoll (1)</p> <p>U. S. Department of Interior Geological Survey, Water Resources Division 500 Zack Street Tampa, Florida 33602</p> <p>ATTN: Mr. A. E. Coker (1)</p> <p>OSSA, SR, NASA Earth Observations Programs Washington, D. C. 20546</p> <p>ATTN: Mr. J. M. DeNoyer, Director (1)</p>
---	--

WILLOW RUN LABORATORIES

Earth Resources Laboratory, GS
Mississippi Test Facility
Bay St. Louis, Mississippi 39520
ATTN: Mr. R. O. Piland, Director

(1)

U. S. Department of Interior
Geological Survey
GSA Building, Room 5213
Washington, D. C. 20242
ATTN: Mr. W. A. Fischer

(1)

Texas Tech University
Department of Mathematics
P.O. Box 4319
Lubbock, Texas 79409
ATTN: Dr. Patrick L. Odell

(1)

NASA Wallops
Wallops Station, Virginia 23337
ATTN: Mr. James Bettie

(1)

Purdue University
Purdue Industrial Research Park
1200 Potter
West Lafayette, Indiana 47906
ATTN: Mr. David Landgrebe

(1)

University of Houston
Mathematics Department
Houston, Texas 77004
ATTN: Dr. Henry Decell

(1)

Rice University
Institute for Computer Services and Applications
Houston, Texas 77001
ATTN: Dr. M. Stuart Lynn

(1)